PHASE TRANSITIONS IN BINARY AND TERNARY VANADIUM OXIDES:

IMPLICATIONS FOR THERMOCHROMIC AND INTERCALATION BATTERIES

A Dissertation

by

GREGORY ALAN HORROCKS

Submitted to the Office of Graduate and Professional Studies of
Texas A&M University
in partial fulfillment of the requirements for the degree of

DOCTOR OF PHILOSOPHY

Chair of Committee,	Sarbajit Banerjee
Committee Members,	Timothy Hughbanks
	James Batteas
	Jodie Lutkenhaus
Head of Department,	Simon North

August 2017

Major Subject: Chemistry

ABSTRACT

The implications of climate change and resource scarcity stand to impose great strain on society, and require the development of novel ways to conserve and store energy. Due to the large portion of energy use accounted for the heating and cooling of buildings worldwide, thermochromic coatings offer promise for reducing energy footprints. Vanadium dioxide has long been a material of interest because of the intrinsitc metal-insulator transition wherein the material switches between a low-temperature, insulating, monoclinic phase (E_B = 0.6 eV, infrared transparent) and a high temperature, metallic, tetragonal phase (infrared reflective). In this work we present the development of a scalable synthesis of extremely high quality vanadium dioxide nanoparticles, exhibiting superior a superior metal-insulator transition comparable to the highest quality films produced via molecular beam epitaxy.

In the field of energy storage, high energy and power density batteries are imperative to help drive the electrification of the transportation industry as well as for grid-level storage. However, there are many issues with current state-of-the-art Li-ion battery technologies including high cost, poor high rate performance, and safety concerns that hinder large scale adoption. However, the mechanisms governing cation transport and phase formation in battery host materials are not well understood. The study of these mechanisms is further complicated by their non-equilibrium nature, requiring multiple modes of characterization that combine theoretical calculations with geometric and electronic structure determination across multiple length scales. In this work, we have used

chemical lithiation as a Li-ion insertion tool to study the mechanism of lithium insertion and diffusion through substrate free nanowires and nanoplatelets of vanadium pentoxide. Specifically, we have examined the dependence of these properties on particle size. Systematic studies utilizing X-ray diffraction, Raman spectroscopy, X-ray absorption spectroscopy, and scanning transmission X-ray microscopy have allowed us to identify the formation of two-phase mixtures upon Li-ion insertion. Combining these measurements with first principles calculations has allowed us to determine the mechanistic origins of this phase separation, and suggest that the barrier to diffusion of Li-ions through layered vanadium pentoxide arises from the formation of a small polaron upon Li-ion insertion. Understanding the mechanisms by which lithium mobility through the layered vanadium pentoxide structure is impeded has allowed us to develop a novel polymorph of vanadium pentoxide that minimizes the strength of the polaronic confinement. By replacing the layered framework with one-dimensional tunnels that provide a more rigid framework and spread the localized electron, we have achieved facile, fast, single-phase lithium insertion and removal.

DEDICATION

This thesis is dedicated to my wife Amanda and daughter Felicity, who have been critical to my success through their love, inspiration, and support. To my dog, Preston, for always lending an ear, and my parents, Liz and Steve, for supporting me in all my endeavors. Finally, to all other friends and family; thank you.

ACKNOWLEDGEMENTS

First and foremost, I must thank Prof. Sarbajit Banerjee. His guidance and mentorship has molded me to become the scientist that I am today, and been a constant source of inspiration and motivation over my graduate career. The personal stake that he invests in his students is the foundation of our group's success, and has opened the door for experiences and opportunities that I would never have expected.

I would also like to thank my committee members, Prof. Timothy Hughbanks, Prof. James Batteas, and Prof. Jodie Lutkenhaus, for their support and guidance in undertaking this work.

Thank you to my friends and the faculty and staff in the Chemistry Department at the University at Buffalo for their support of the beginning of my graduate career.

Thanks to all of the current and past members of the Banerjee group for their support, and friendship. I couldn't have asked to work with a better group of scientists. Your comradery and insight helped bring me through the most difficult periods of this journey.

Finally, I need to thank Prof. Marvin Illingsworth at the Rochester Institute of Technology. You inspired my interest in inorganic chemistry, and laid the foundation of academics and research that my success has been built upon. I am beyond thankful for the time that I got to spend with you. The world is certainly worse off without you.

CONTRIBUTORS AND FUNDING SOURCES

Contributors

This work was supervised by a dissertation committee consisting of Professor Sarbajit Banerjee [advisor], Professor Timothy Hughbanks and Professor James Batteas of the Department of Chemistry and Professor Jodie Lutkenhaus of the Department of Chemical Engineering.

Some of the data analyzed for Chapter 2 was provided by Professor Sambandamurthy Ganapathy, and Dr. Sujay Singh of the University at Buffalo. The computational results depicted in Chapter 4 were conducted by Dr. Yufeng Liang, and Dr. David Prendergast of Lawrence Berkeley National Lab. Chapter 5 includes contributions from Dr. David Prendergast of Lawrence Berkeley National Lab, and Dr. Louis F. J. Piper of the University of Binghamton.

All other work conducted for the dissertation was completed by the student independently.

Funding Sources

Graduate study was supported by a fellowship from Texas A&M University and a dissertation research fellowship from the Texas A&M Energy Institute through the MP2 Energy Fellowship.

This work was made possible in part by the National Science Foundation under Grant Number DMR 1504702. Its contents are solely the responsibility of the authors and do not necessarily represent the official views of the National Science Foundation.

TABLE OF CONTENTS

Page

LIST OF FIGURES

Page

Page

LIST OF TABLES

Page

CHAPTER I

INTRODUCTION*

Vanadium oxides are materials of particular interest in solid state chemistry due to their large range of accessible oxidation states and structural motifs.[1–3] These variations in geometric and electronic structure give rise to many interesting properties ranging from abrupt modulations of electronic and optical properties to reversible insertion and removal of guest cation species.[4–6] The structural variations of this family arise due to the accessibility of valences ranging from +2 to +5, several stable vanadium coordination symmetries (octahedral, distorted octahedral, square pyramidal, tetrahedral), and the accommodation of defects through crystallographic shear and charge localization/delocalization.[3,7,8] One of the fundamental pursuits of solid state chemistry is the correlation of structure and function. However, there are few systems in which the geometric and electronic structures can be tuned independently. The binary and ternary vanadium oxides offer a sandbox wherein structure and composition can be systematically and

---

*Portions of this chapter have been adapted with permission from "Transformers: The Changing Phases of Low-Dimensional Vanadium Oxide Bronzes" by P. M. Marley, G. A. Horrocks, K. E. Pelcher and S. Banerjee, *Chem. Commun.*, 2015, **51**, 5181–5198. Reproduced by permission of the Royal Society of Chemistry.

*Portions of this chapter have been adapted from "X-ray Spectroscopy and Imaging as Multiscale Probes of Intercalation Phenomena in Cathode Materials" Horrocks. G. A.; De Jesus, L. R.; Andrews, J. L.; Banerjee, S. *JOM, Accepted.*

*A Portion of this chapter has been adapted from "Mapping Polaronic States and Lithiation Gradients in a Individual V_2O_5 Nanowires" De Jesus, L. R.; Horrocks. G. A.; Liang, Y.; Parija, A.; Jaye, C.; Wangoh, L.; Wang, J.; Fischer, D. A.; Piper, L. F. J.; Banerjee, S. *Nat. Commun.* 2016, **7**, 12202.

independently varied through manipulation of physical environment (temperature, pressure)[4,9] or various chemical transformations (Figure I.1),[1,2] allowing for the study of properties ranging from the fundamentals of electron correlations to the mechanisms of cation insertion and diffusion through host structures. Understanding the mechanistic underpinnings of these structure-function relationships opens the promise of being able to develop rules by which novel materials can be rationally designed to optimize desired properties. This work will focus on the study of phase transitions in binary and ternary vanadium oxides, specifically VO_2 and $Li_xV_2O_5$. The understanding of the mechanisms of these transitions has allowed for the development of novel synthetic routes to minimize defects in VO_2, and the identification of diffusion barriers in V_2O_5, and the design of a novel cathode material.

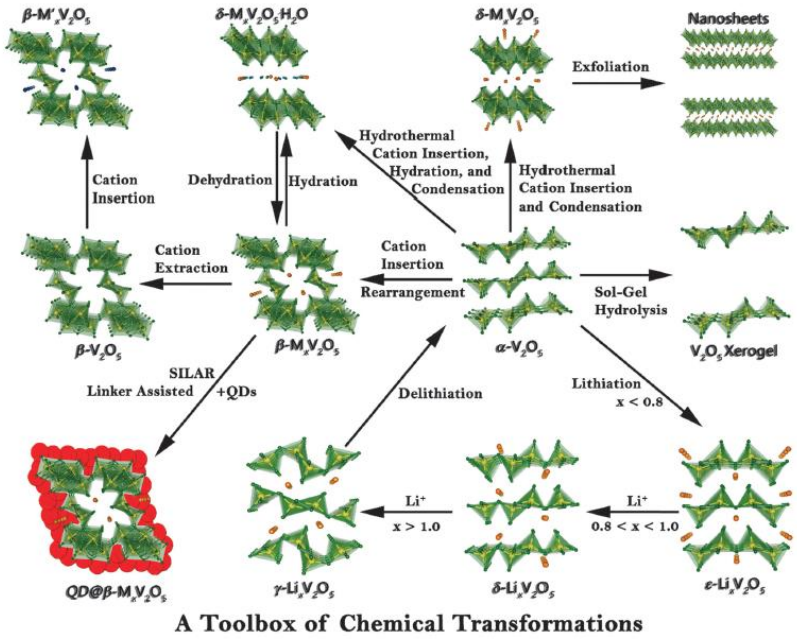

Figure I. 1: Intercalation induced phase transitions, structural rearrangements, and modifcations of ternary vanadium oxide bronzes. Reprinted from 5.

Vanadium dioxide, VO_2, is often considered the canonical example of a metal-insulator transition (MIT) material due to the sharp modulation of electronic and optical properties, and the relative proximity of the transition to room temperature (67°C).[4] The strong electron-electron correlations in VO_2 result in coupling of electronic and lattice instabilities, producing a discontinuous change in the material's resistivity that can span five orders of magnitude and a sharp reduction of the infrared tansmissivity (ca. 50%), but the mechanism of which has been the subject of intense debate since it's discovery by Morin in 1959.[10] This uncertainty surrounding the roles of electron-phonon, and electron-electron correlations in VO_2 make it a good model system for the study of these phenomena.[11–16] Additionally,

the readily accessible transition temperature, the 0.6 eV bandgap of the low-temperature phase making the material transparent to infrared radiation, and the ability to tune the transition temperature via particle size, doping, and strain have made VO_2 a fantastic candidate for thermochromic applications, such as "smart-windows."[4,17] The metal-insulator transition in VO_2 occurs between the high-temperature, metallic, tetragonal phase (rutile-like (R), $P4_2/mnm$) and the low temperature, insulating, monoclinic phase (M_1, $P2_1/c$). Understanding the nature of the change in properties across the transition necessitates an understanding of the differences between these two structures. The high-temperature phase is characterized by chains of VO_6 octahedra linked in along the crystallographic *c*-axis via edge sharing wherein neighboring vanadium centers are separated by ca. 2.85 Å. In the *a* and *b* directions, the VO_6 chains are linked to one another via corner sharing.[18] Upon cooling past the transition temperature, the M_1-phase is formed as the structure distorts *via* a tilting of the VO_6 octahedra, yielding a doubling of the unit cell and a dimerization of V-V distances yielding a "short" distance of 2.65 Å, and a "long" distance of 3.12 Å along the R-phase *c*-direction (Figure I.2a). [18] From a bonding perspective, in the tetragonal phase, the octahedral coordination of the vanadium centers splits the V d-orbitals into the t_{2g} and e_g sets. Wherein the e_g set (d_{z2}, d_{x2-y2}) coordinate with the oxygen ligands through a strong σ-bonding interaction. The t_{2g} orbitals, which are further split due to a tetrahedral Jahn-Teller distortion of the VO_6 octahedra separating the d_{xz} and d_{yz} orbitals from the d_{xy} orbital. The d_{xz} and d_{yz} orbitals then coordinate *via* π-interactions with the oxygen,

while the d_{xy} orbital is projected at the neighboring V-atoms in the *c*-direction. Though this orbital is non-bonding, it is occupied by the single d electron from each V^{+4} center. This occupied state straddles the fermi level, and renders the material metallic, and thus reflective to infrared radiation (Figure I.2b). Upon transitioning to the monoclinic phase, the octahedral tile leads to an increase in the strength of the π-interactions of the d_{xz} and d_{yz} orbitals with the oxygen ligands. Meanwhile the dimerization of the V-centers allows for strong overlap of the d_{xy} between the dimerized V-atoms, splitting the previously non-bonding orbital in the tetragonal phase into a bonding and antibonding set in the monoclinic phase.[18] This split opens a gap (ca. 0.6 eV) between the d_{xy} and the unoccupied states it previously overlapped, effectively localizing the d^1 electron within the dimer pairs (Figure I.2b), and rendering the material infrared transparent (Figure I.2b).[18]

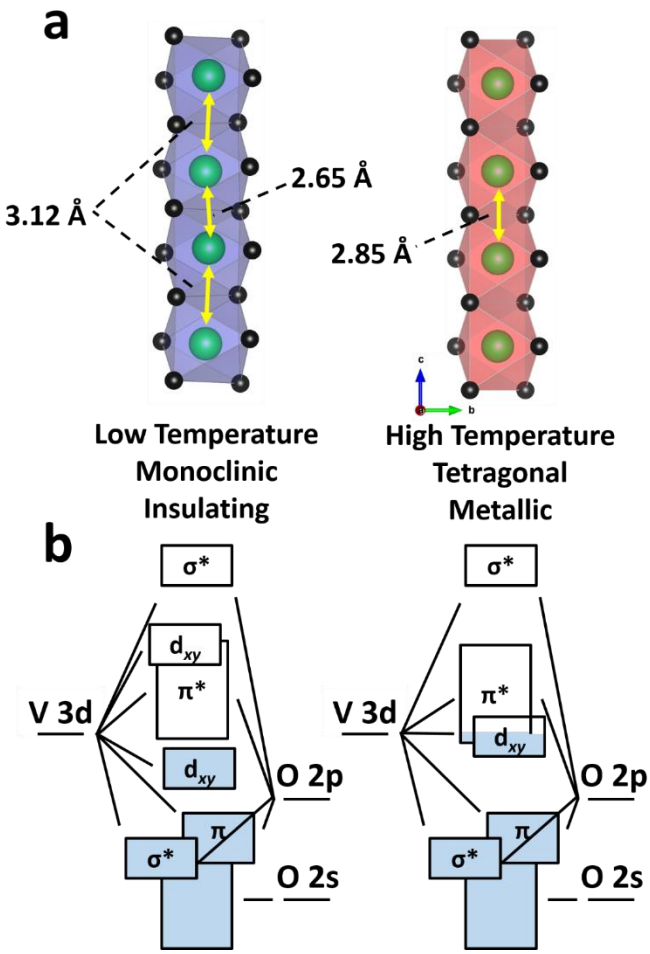

Figure I. 2: (a) crystal structures of the monoclinic (left) and tetragonal (right) phases of VO_2, with V-V distances along the VO_6 chains indicated. (b) molecular orbital diagram illustrating the different electronic structures of the two phases.

Despite almost 60 years passing since the identification of the MIT in VO_2, and significant research interest in suppressing the transition temperature and deployment into films, there is currently no widely available commercial glass utilizing this technology. This is due to several factors. First, the native transition temperature is too high to be useful in real-world environments, although there is significant literature of doping VO_2 wherein this problem has largely been solved,

though doping brings about other issues such as a broadening of the transition, increased hysteresis, and a decrease of transition magnitude.[4,19–25] A second obstacle to development of commercial films is related to the volume change that accompanies the MIT. Due to the ca. 1% anisotropic volume change between the low- and high-temperature phases bulk particles, thin films, and single crystals quickly pulverize and degrade upon cycling. While single crystals of VO_2 have exhibited MIT magnitudes approaching 5 orders of magnitude, and epitaxially grown thin films routinely surpass 4 orders of magnitude, these materials are not robust enough to withstand repeated cycling. Nanostructuring of VO_2 allows for extended cycling due to the increased ability of nanostructures to accommodate strain. Such nanostructures have reported the ability to cycle thousands of times without significant particle degradation. Additionally, the synthesis of large amounts of free standing nanoparticles offers the ability to deploy the thermochromic film in a variety of ways, such as spray coating, *via* a paint, or in a laminate film. Thus far, there have been two primary approaches to the synthesis of VO_2 nanostructures: vapor deposition techniques,[13,26–28] and hydrothermal synthesis.[20,29–31] Though each synthetic route has its advantages, they both suffer from significant drawbacks. Vapor phase synthesis has shown the ability to produce extremely high quality VO_2, exhibiting transition magintudes comparable to the best molecular beam epitaxy (MBE) grown films the product volumes are on the order of micrograms, and often substrate bound. Hydrothermal synthesis has shown the ability synthesize larger volumes of free standing VO_2 nanoparticles of various

morphologies, but these materials typically exhibit reduced MIT magnitude, large hysteresis, and slower transitions.[29,31–33] In this dissertation we seek to address the lack of a method of producing large volumes of extremely high quality VO_2 nanostructures. The problem that invariably arises during solution phase production of these materials is the difficulty in precisely controlling the stoichiometry of the formed VO_2, as VO_2 inhabits a relatively narrow silver of the vanadium-oxygen phase diagram, and even slight stoichiometric deviations rapidly degrade the phase transition properties.[34–37] While calculations have indicated that up to a 50% reduction of infrared transmissivity is possible across the MIT,[38] because the optical property modulation is due to the change in the dielectric constant of the material, a reduction in the magnitude of the electrical properties will be linked to a smaller modulation of the optical transmission. Chapter II presents the development of a novel stepwise hydrothermal synthesis of undoped VO_2, wherein the careful control of stoichiometry is possible, yielding free standing nanowires with outstanding MIT properties.

The main portion of this dissertation is concerned with the study of Li-ion insertion into V_2O_5. The investigation of the mechanisms governing Li-ion insertion and diffusion within single-layered V_2O_5 are discussed, and the applications of this insight in the rational design of a novel cathode material. Since their first commercial adoption in the early 1990s, Li-ion batteries have rapidly eclipsed competing alternatives for electrochemical energy storage and emerged as the principal source of portable power owing to their currently unrivaled combination

of high energy and power densities.[39] However, despite their ubiquity in powering small personal electronics, the deployment of these technologies in the large-area formats required for electric vehicles and grid-scale storage has been hampered by issues associated with cost, safety, cycle life, and high-rate performance. Elucidation of the fundamental mechanisms underpinning the roots of capacity fade, energy dissipation, and poor cation diffusion kinetics has emerged as an urgent imperative given their impact on the ultimate performance of an intercalation battery. The complexity of this problem derives in large measure from the multiple length scales, spanning in range from atomistic to mesoscale dimensions, and the out-of-equilibrium nature of processes involved in charge and mass transport within Li-ion batteries. From a design perspective, this necessitates understanding not just of thermodynamic properties of an electrode material but also requires detailed consideration of the kinetics of multiscale transport phenomena.

The working principles of an intercalation battery can be distilled down to alternating insertion and extraction of cations from a host lattice accompanied by the oxidation/reduction of a redox-active metal center.[6] The host lattice is inevitably transformed upon cation insertion and the magnitude and nature of perturbations to its atomistic and electronic structure determine the capacity and rate performance of an intercalation cell. While redox processes are fundamentally atomistic in nature involving single transition metal centers, cation intercalation can bring about phonon-driven structural transformations that span extended length scales. Intercalation-induced phase transformations can furthermore induce

inhomogeneous strain and establish charge and mass transport pathways that extend across interconnected networks of particles, giving rise to considerable mesoscale heterogeneities. The practical consequences of such mesoscale heterogeneity are quite profound including electromechanical degradation, high-current localized "hot-spots", and capacity fading.[40,41]

Intercalation-induced phase transformations are observed for both anodic[42,43] and cathodic[41,44–48] active materials and underpin heterogeneity across individual particles as well as ensembles of particles.[41,46–48] One approach to mitigating phase separation has been the scaling of materials to sub-micron dimensions. The energetic penalty of having a phase boundary within a small particle can be prohibitively expensive, thereby suppressing phase segregation;[49] furthermore, from a kinetic perspective shorter Li-ion diffusion lengths can mitigate the formation of lithium concentration gradients that occur when surface insertion proceeds more quickly than bulk diffusion.[47,48] Elucidating the progression and spatiodynamic evolution of intercalation and resulting phase transformation processes requires the use of multiscale characterization methods. Element-specific X-ray spectroscopy serves as a sensitive probe of local structure and oxidation state, and when such measurements are accessed using finely focused X-ray probes in scanning transmission X-ray microscopy (STXM) or ptychography can further capture emergent phenomena at extended length scales.[50]

Here we provide an illustrative overview of the use of synchrotron-based X-ray spectroscopy and imaging methods as probes of local atomistic and electronic

structure, and of phase heterogeneity at various length scales. Layered orthorhombic V_2O_5 long known to be an intercalation host is discussed as a model system to illustrate fundamental mechanistic ideas.[51]

Structural transformations induced upon cation intercalation have been extensively studied, both in terms of modifications of the average crystal structure as well as distortions of the local structure, using X-ray diffraction,[48,52] total scattering, solid-state nuclear magnetic resonance spectroscopy,[53] and electron microscopy.[43,54] In contrast, X-ray emission and absorption spectroscopies serve primarily as probes of electronic structure and thus allow for development of a detailed picture of where electron density resides within cathode materials.

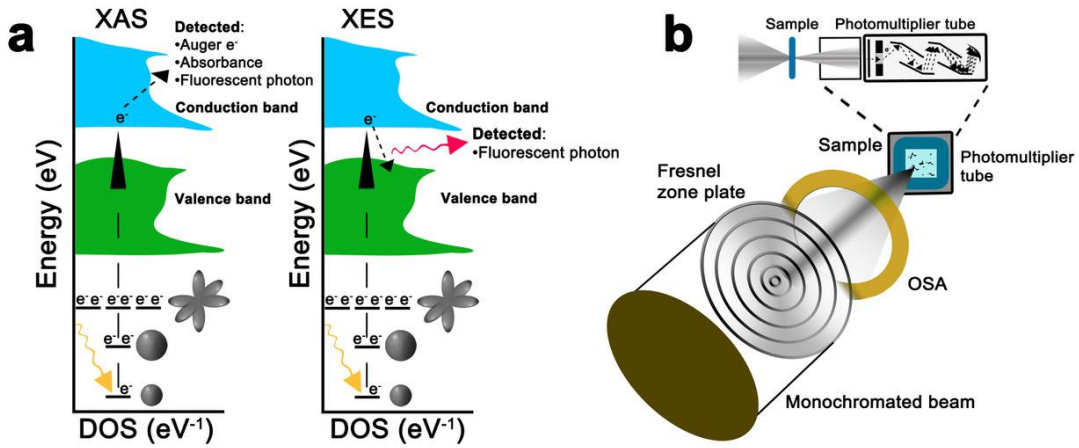

Figure I. 3: (a) Schematic depicting the excitations involved in X-ray absorption (XAS) and X-ray emission spectroscopies (XES). In XAS, a photon excites a core-level electron to the conduction band. In comparison, in XES an excited core-level electron in the conduction band relaxes to an empty lower state emitting a photon. (b) Schematic of the STXM setup: the Fresnel zone plate diffracts a monochromatic beam, which is then sorted by the order-sorting aperture. The beam is focused to the sample and transmitted photons are detected.

X-ray absorption spectroscopy (XAS) is an element-specific probe of the unoccupied density of states and offers a wealth of information ranging from oxidation state to the local coordination symmetry, and an orbital-specific view of the conduction band.[50,55] This method involves the excitation of a core-level electron into partially occupied or unoccupied states in the conduction band (Fig. I.3a), as subject to dipole selection rules (change in angular momentum quantum number $\Delta l = \pm 1$ with conservation of spin). Measurement of the absorption cross-section, performed directly in transmission mode or by the detection of Auger electrons or fluorescent photons, allows for mapping of transitions to unoccupied states. The features within the immediate vicinity of the absorption edge are denoted as X-ray absorption near-edge structure (XANES) features and to a first approximation reflect the atom-projected unoccupied density of states. Such spectra are interpreted either with the aid of "model" compounds that contain similar bonding motifs or by comparison to density functional theory (DFT) calculations.[56] The spectra thus provide rich information on oxidation state, bonding character, and chemical environment of the absorbing atom.

Further from the absorption edge (>50 eV beyond the main edge), the extended X-ray absorption fine structure (EXAFS) region contains oscillations corresponding to modifications to the X-ray absorption coefficient as a result of the photo-electron being scattered by adjacent atoms. The measured scattering amplitude and phase shift can be fitted to obtain best-fit values of nearest neighbor and next-nearest neighbor distances (out to about 5 Å), the coordination number,

and the disorder in the distances for each shell,[57] thus providing a sensitive probe of local structure. Indeed, XAS methods can be applied even to entirely amorphous samples, which is especially relevant to the study of conversion reactions such as in $Ag_2VO_2PO_4$ or $Ag_xV_2O_5$ wherein electrochemical cycling is accompanied by considerable amorphization.[58]

For transition metal oxides such as cobalt oxides, the NMC family of materials, Li_xFePO_4, and vanadium oxides that comprise the most commonly investigated intercalation hosts, the specific transitions probed include $1s \rightarrow 2p$ K-edge transitions at the O or transition metal K-edges or $2p \rightarrow 3d$ L-edge transitions at transition metal L-edges. At transition metal K-edges, the peak position of the primary absorption energy reflects the oxidation state, whereas the appearance of pre-edge absorption features (resulting from hybridization of metal-d and p states)[47,59] can be used to elucidate both oxidation state and local coordination symmetry. Transition metal L-edges are characterized by multiplet effects but also contain a wealth of information regarding oxidation states; specific states contributing to the bottom of the conduction band can oftentimes be resolved.[60,61] The availability of first-principles and multiplet calculations has provided new impetus to the interpretation of transition-metal-$L_{3,2}$-edge spectra.[62]

Recent advances in X-ray optics have allowed for XAS methods to be deployed with a high degree of spatial as well as spectral resolution permitting the use of these methods as powerful imaging tools for mapping of compositional inhomogeneities in battery materials (Fig. I.3).[50,63] In STXM, the incident beam is

focused onto the sample by diffraction through a Fresnel zone plate (ZP), with the subsequent sorting of the X-rays by the order-sorting aperture (OSA), as depicted in Figure I.3b. Images are acquired by rastering the focused beam on the sample pixel-by-pixel at a series of X-ray energies with the absorbance being detected at each pixel and each X-ray energy; the measurement thus yields a hyperspectral "stack" that corresponds to a distribution map of a specific element or chemical group. The spatial resolution of STXM is on the order of a few tens of nanometers; sub-10 nm spatial resolution is accessible from ptychography.[50,64] The ability of STXM to develop detailed compositional maps provides a powerful means of resolving compositional inhomogeneities and lithiation gradients. The application of principal component analysis (PCA)[65] methods further allows for identification of phase boundaries without *a-priori* knowledge of spectral signatures of individual phases.

As a complementary probe of the unoccupied states, X-ray emission spectroscopy (XES) methods probe the valence band. Non-resonant X-ray emission spectroscopy (NXES) is performed by exciting at an energy much greater than the upper edge of the valence band. This ensures that core-shell electrons are excited to a continuum state in the conduction band. Once electrons from the core-shell are excited to continuum states, electrons in occupied states of the valence band radiatively decay to fill the empty core-hole, releasing the excess energy as fluorescent X-ray photons (Fig. I.3), which are detected and energy resolved. A NXES spectrum thus maps the energies of occupied states in the valence band. The

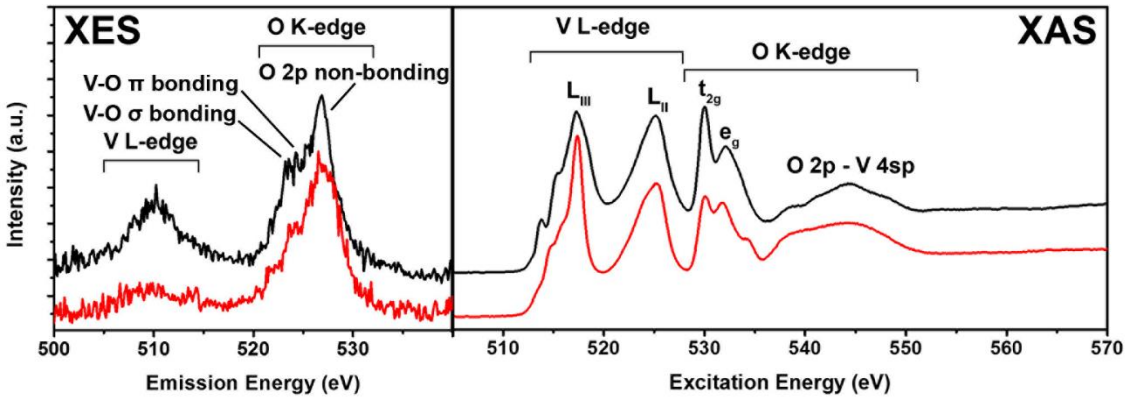

Figure I. 4: Combined XAS/XES spectra probing valence and conduction band states of α-V_2O_5. (Left) Non-resonant X-ray emission spectra (NXES) for V_2O_5 depicts the occupied states below the Fermi level. (Right) XANES spectra collected at the V L- and O K-edges probe the unoccupied density of states above the Fermi level. The evolution of NXES and XANES spectra upon lithiation is also shown suggesting a clear modification of electronic structure induced as a result of vanadium reduction.

NXES and XAS spectra can be combined on a common energy scale to determine the size of the electronic band gap by adjusting for the core-hole energy shift.[66] Figure I.4 shows the evolution of XAS and XES spectra of V_2O_5 upon lithiation.

Alternatively, resonant X-ray emission spectra (RXES) can be acquired by exciting at an energy coincident with prominent features in the XAS spectrum. In doing so, the decay process is fundamentally altered, yielding better resolved spectral features and allowing for relatively low absorption cross-section d—d (Δl=0) and charge transfer (CT) transitions to be distinguished. The evolution of the valence band with intercalation is useful for monitoring localization of electron density and the appearance of defect states.[67]

The use of X-ray spectroscopy at Li K-edge as a probe of the Li-ion local environment is attractive but given the low excitation energies (55 eV) has been

quite challenging.[68] The poor penetration of these low energy X-rays makes the Li K-edge very sensitive to the surface chemistry of the material. However, by contrasting surface-sensitive electron-yield detection with deeply penetrating fluorescence yield detection, it is possible to probe the different storage states of Li-ions at particle surfaces and in the bulk.

The open frameworks of the ternary vanadium oxides (Scheme I. 1) provide much opportunity for topotactic transformations and post-synthetic modifications. This versatility and structural flexibility lends itself to numerous potential applications. One is hard pressed to think of another strongly correlated system that be "modified on the fly" to change properties in a similar manner. Scheme 1 depicts a toolbox for post-synthetic modifications and transformations of the ternary vanadium oxide bronzes. Many of these transformations (*vide infra*) are inaccessible in the bulk owing to kinetic impediments but can be realized quite readily at nanoscale dimensions assisted by the rapid solid-state diffusion of cations within nanostructures.[69–71] It is worth noting that the intercalation/deintercalation time $t \sim [l^2/D]$ where D is the diffusion coefficient and l is the distance through which the ions need to diffuse. Shorter diffusion path lengths yield dramatically improved Li-ion insertion and diffusion kinetics.[72–74] The higher surface area of nanostructures (as long as they are prevented from agglomerating) also implies a greater active area of contact with a solution, enabling facile chemical and electrochemical modification.

Perhaps the most well-studied series of phase transformations in vanadium oxide bronzes are those induced as a result of the insertion of Li-ions.[3,6,75] From a structural perspective, α-V_2O_5 would appear to be an excellent cathode material. It is a layered van der Waals' solid with ample interlayer spacing and its d^0 electron configuration leads to several easily-accessible redox states.[6] It would seem that α-V_2O_5 satisfies many of the criteria for identifying good cathode materials established by Whittingham when evaluating Li-ion-insertion in TiS_2.[76] These criteria include: reversible insertion, a high free energy of reaction (predicted to be up to -3.58eV/Li), a wide range of stoichiometry, high diffusivity of the guest ion, good electronic conductivity, and insolubility of the cathode in the electrolyte.[6,76,77] Intercalation up to x=1 corresponds to a high theoretical capacity of 250 $mAhg^{-1}$. Finally, V^{5+} is not Jahn-Teller active, which promises greater stability of V_2O_5 as compared to other oxides.[78,79]

First proposed by Whittingham in 1976, the Li-ion storage properties of V_2O_5 have been studied in a variety of forms ranging from micron-sized bulk powders to crystalline films, xerogels, aerogels, and nanostructures synthesized by a variety of methods.[6,51,75,80] Due to the ability of the open layered frameworks to accommodate guest cations, the insertion of Li-ions yields relatively modest volume changes as compared to materials where Li insertion proceeds *via* conversion chemistry. Indeed, the maximum change in volume of 25% per V_2O_5 unit occurs upon lithiating to the *e*- and *d*- phases (as depicted in Scheme 1), and is relatively modest in comparison to the 200-300% volume changes observed upon

lithiation of materials such as SnO_2, and Si.[81,82] As has been shown previously for numerous systems, scaling to finite sizes can offset even severe size changes induced during cycling due to the ability of nanostructures to more readily accommodate strain.[70,83,84] However, the promise of V_2O_5 as a cathode material has not been borne out in full because of a number of impediments.[51] Since α-V_2O_5 shares many structural similarities to successful layered materials such as Li_xCO_2, yet is hampered by many challenges, it provides a perfect foil for a case study of impediments to the development of successful intercalation cathode materials and how these might be mitigated. Figure I.5 shows morphologies of various V_2O_5 structures prepared by vapor transport and hydrothermal processes.[48,61,85] Stark differences are noted in the intercalation and phase transformation kinetics as well as phase homogeneity as a function of the size and morphology of these structures.[48]

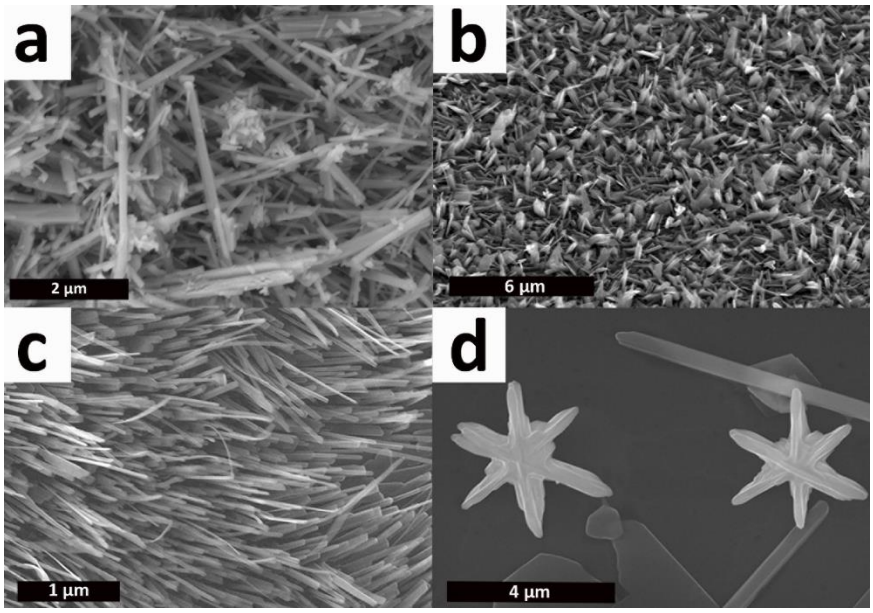

Figure I. 5: SEM images of (a) hydrothermally grown nanowires,[48] (b) nanoplatelets grown by vapor transport,[48] (c) nanowire arrays grown by vapor transport,[61] and (d) nanostars grown by vapor transport followed by hydrothermal treatment.[85]

Unlike Li_xTiS_2 or Li_xCoO_2 (or even $LiFePO_4$ at high rates), $Li_xV_2O_5$ does not form a single solid solution across the entire stoichiometry range ($0<x<1$). Instead, with increasing lithiation V_2O_5 undergoes three reversible and two irreversible phase transitions.[1,6,48] Although the range of lithium content wherein these phases are stable is somewhat dependent upon particle size and morphology, the bulk phase diagram follows a generally accepted progression. First, sites between the layers of V_2O_5 are occupied up to a stoichiometry of α-$Li_{0.1}V_2O_5$ with minimal distortion of the lattice.[1] Upon further lithiation, the material undergoes a phase transition to ε-$Li_xV_2O_5$, wherein the layers begin to distort as the VO_5 units pucker inwards to facilitate coordination of Li with the oxygen of the long vanadyl [V=O] bond ($0.35<x<0.7$).[1] Beyond x=0.7, the structure undergoes another phase

transition to δ-$Li_xV_2O_5$, wherein alternating V_2O_5 layers glide along the *b*-axis to accommodate the extra Li-ions, marking a significant, yet reversible, structural change. However, beyond x=1.0, the structure undergoes an irreversible phase transition to γ-$Li_xV_2O_5$ ($1.0<x<2.0$) wherein the up-up–down-down connectivity of the V_2O_5 layers is lost in favor of an alternating up-down-up-down connectivity.[1] Finally, beyond x=2.0, the structure is converted to rock-salt ω-$Li_xV_2O_5$, a complete departure from the original 2D structure.[1] In the bulk, it is known that the transitions between the $\alpha \leftrightarrow \varepsilon \leftrightarrow \delta$-phases are completely reversible, whereas lithiation to the γ and ω-phases are structurally irreversible (though they can be reversibly lithiated and delithiated with preservation of the γ and ω frameworks).[86] The γ-phase cycles between $0 \leq x \geq 2$, with the removal of Li-ions yielding a metastable γ'-phase of V_2O_5; this phase converts to orthorhombic V_2O_5 (the thermodynamic minimum) upon annealing to a temperature of ca. 610 K.[7] The *w*-phase can be cycled between $0.4 \leq x \geq 2.65$ with the initially formed tetragonal phase transitioning to a rock-salt structure after one cycle as a result of a reordering of the cations to minimize electrostatic repulsions.[87]

A more in-depth look at the structural progression that occurs upon lithiation is germane to fully understanding how these metastable phases relate to one another and the pristine phase. From a structural perspective, in going from the α- to the δ-phase, the inserted Li-ions coordinate with the apical oxygen atoms of the V_2O_5 square pyramidal units and the bridging oxygen atoms of the layers immediately above or below. The Li—O interaction tilts these apical oxygen atoms towards one

another and pulls the bridging oxygens slightly into the interlayer space, causing a progressive puckering of the layers along the *a*-*b* planes. This puckering and occupation of the interlayer sites by Li-ions results in a gradual increase in the interlayer spacing from 4.368 Å for the unlithiated α-phase to 4.958 Å for the ε-phase to 5.270 Å for the δ-phase and 5.600 Å for the γ-phase. As a consequence of the puckering of the layers along the *a*-*b* planes and the increase in the interlayer space, there is a concomitant decrease in the *a*-parameter of the unit cell.[6,75] This parameter decreases from 11.51 Å in the α-phase to 11.38 Å in the ε-phase to 11.24 Å in the δ-phase and 9.69 Å in the γ-phase.[6,75] The initial insertion of Li-ions induces subtle puckering of the layers with a very modest increase of the *c* parameter. Upon the addition of more Li-ions, the weak van der Waals' forces binding the layers are disrupted, resulting in a significant increase in the *c*-parameter. For low Li-ion concentrations, the intercalated ions are cuboctahedrally coordinated by eight oxygens in one layer and four from the next layer. Above a Li-ion content of $x = 0.5$, the Li-ions can no longer evenly distribute across available cuboctohedral sites and must now begin to occupy remaining sites neighbouring those already occupied by other Li-ions. This gives rise to a distinctive ε'-phase, which can be identified as a distinct subset of the ε-phase by the emergence of new vibrational modes in the Raman spectra as the Li—Li distance is halved; increased puckering is observed at this point as a result of electrostatic repulsions between adjacent Li-ions.[69,88–91] Further differentiating the ε'-phase is the emergence of stacked monoclinic and orthorhombic domains that appear to be stochastically

ordered along the (001) direction. The ε'-phase has been reported by Katzke to be incommensurately modulated and to undergo a ferroelastic transition upon cooling.[90,91]

Further lithiation in the window between $0.88 < x < 1.0$ yields the δ-phase, which is characterized by an additional increase in the puckering of the layers and an increase in the interlayer spacing. The filling of the cuboctohedral sites of the ε-phase gives way to Li-ions approaching tetrahedral coordination. In this motif, the Li-ions are coordinated with the two oxygens at the apices of the square pyramidal units in one layer as well as to the two bridging oxygens from the next layer. The severe puckering brings about a doubling of the *b*-parameter as alternate layers shift by one half of a unit cell.[6,75] Beyond $x = 1.0$, the γ-phase of $Li_xV_2O_5$ is stabilized. As illustrated in Scheme 1, the high cation concentration drives a severe distortion from the parent layered structure. While none of the structural changes through the δ-phase involve breaking of any V—O bonds, the transition to the γ-phase results in an inversion of half of the square pyramids, resulting in a transformation from an up-up-down-down pattern of connected square pyramids to an up-down-up-down pattern. This facilitates a massive increase of the puckering of the layers and results in a Li-ion coordination environment that is almost completely tetrahedral.[6,75]

With further lithiation, the ω-phase is formed at $x > 2.5$. When first formed, this phase adopts a tetragonal superstructure with rock-salt-like subunits. After cycling, this superstructure gives way to a simple disordered rock-salt structure as the lithium and vanadium cations redistribute within the array of face-centred-cubic

packed oxygens to minimize repulsive interactions.[87] This structure is yet to be definitively resolved. Indeed, an alternative description propounded by Rozier and co-workers for the $1 < x < 3$ phase space suggests the formation of mixture of vanadates ($LiVO_3$, Li_3VO_4, $LiVO_2$) and oxides (V_6O_{11}, V_2O_3) in equilibrium with the native $Li_xV_2O_5$ phase.[92] The incipient vanadate and oxide phases are thought to be produced as a result of the disproportionation of V^{4+} with the products being determined by the Li-ion content of the disproportioning phase. These authors cite the initial formation of $LiVO_3$ followed by orthovanadate Li_3VO_4, with V_6O_{11} and V_2O_3 as accompanying oxides. As the Li-ion content approaches $x = 3$, cubic Li_xVO_2 is thought to be formed and the commonly observed reversible insertion/deinsertion seen for the cycling of the *w*-phase between $1.5 < x < 3$ is alternatively ascribed to the reversible cycling of 1.5 mole of $LiVO_2$ formed per mole of V_2O_5.[92]

Scaling materials from bulk and micrometer-sized particles towards nanometer-sized dimensions substantially modifies the phase stabilities and phase boundaries both as a result of potentially altering the thermodynamic stabilities of different phases as a result of contributions to the free energy from surface/interfacial energy terms as well as due to modified kinetic energy barriers for phase transformations.[93–96] For Martensitic phase transformations proceeding through a classical nucleation and growth mechanism, phase transitions are typically initiated at imperfections; a reduction in size reduces the probability of an imperfection occurring within a specific volume and thereby can kinetically trap a

phase across a broader region of phase space than predicted by thermodynamics alone.[94,95] In other words, for a Martensitic phase transition, kinetic barriers can increase with decreasing size. The converse is typically true for phase transitions induced as a result of intercalation. The kinetic barriers for diffusion of ions in the solid state are significantly lowered within nanostructures and thus phase transitions derived from insertion/extraction of ions become much more facile. These modified phase stabilities are also particularly reflected in the reversibility of the structural transformations.

While in the bulk there is complete structural reversibility through the δ-phase, the formation of the γ- and ω-phases are irreversible. These final two phases can be reversibly lithiated and delithiated with retention of the γ-and ω-frameworks; however, once formed the severe distortions do not permit reversion to the layered a-V_2O_5 framework. However, scaling to nanometer-sized dimensions has been shown to enable structural reversibility that is unprecedented in the bulk.[48,71] Cui and co-workers found that V_2O_5 nanorods lithiated all the way to w-$Li_xV_2O_5$ phase reverted back to the unlithiated α-V_2O_5 structure upon extraction of Li-ions using Br_2 solution.[71] From an electrochemical storage perspective, this structural flexibility reduces irreversible lithiation, providing higher energy densities. The lithiation/delithiation rates are also significantly greater yielding higher power densities. Martin and co-workers have reported a doubling of the high-rate capacities of V_2O_5 nanostructured arrays prepared using an anodic aluminium oxide template as compared to thin films, and have established a clear inverse correlation

between particle size and discharge capacities for nanorods grown by templated methods.[97] Whittingham and co-workers have also shown that nanometer-sized particles show improved Li-ion insertion rates and cycling stabilities based on a systematic study of V_2O_5 particles ranging in size from tens of nanometers to micrometers.[6] At high Li-ion concentrations, Cui and co-workers note the conversion of some ultra-thin domains within V_2O_5 nanorods to the highly lithiated ω-phase within just 10 s.[71] These phase transitions pose numerous problems. First, phase transitions inevitably require energy dissipation. The nucleation and subsequent propagation of new phases is furthermore significant, and impacts the diffusion rate of Li-ions within the material.[45] Second, because the structural transitions above x=1.0 are irreversible, the viable voltage range of the material is limited.[6] Finally, dynamic phase nucleation results in inhomogeneities both between particles of different sizes and within individual particles thereby yielding local current profiles dramatically different than predicted from the global voltage of the cell.[45,47,48]

A second major challenge with V_2O_5 lies in its electronic structure and the specific crystal-field-splitting pattern of V3d-derived states in this material. The square pyramidal local coordination environment of vanadium induces splitting of V3d states into three distinct energy levels with the V3d_{xy} states forming a distinctive "split-off" conduction band that is well separated and several tenths of an eV below the rest of the conduction band.[45,47,60,66,79] Intercalation of Li-ions within α-V_2O_5 results in initial occupation of this localized V 3d_{xy}-derived band, as

evidenced by XANES spectroscopy.[45] The non-degenerate nature of this state and poor wavefunction overlap of the narrow d-bands results in local trapping of electrons.[45,60,66]

NXES and RXES of α-V_2O_5 have recently been performed using an energy-discriminating detector and an indirect band gap of 1.90±0.2 eV, has been determined.[66] The split-off conduction band is also clearly resolved at the V L-edge. In order to understand the evolution of the electronic structure of V_2O_5 upon lithiation, it is germane to first discuss the spectra of unlithiated V_2O_5. Velazquez *et al.* have used XANES to probe an oriented array of V_2O_5 nanowires at various polarizations. The angle-resolved XANES spectra are depicted in Figure I.6 and show pronounced anisotropy.[61] The spectral features can be assigned to distinct transitions with the help of previous DFT calculations.[60] The V L-edge comprises resonances that arise from the $V2p_{3/2} \rightarrow V\ 3d$ (centered at 518 eV, labeled L_3) and $V2p_{1/2} \rightarrow V3d$ (centered at 525 eV, labeled L_2) transitions. Although L_2 is less useful as a result of a Coster–Krönig Auger decay process, the L_3-edge shows fine-structure resonances that reflect the orbital characters of the bottom of the conduction band of V_2O_5. The first two features are centered at 515.6 and 516.8 eV; the former, the "split-off conduction band", corresponds to the transition of a V2p electron to the empty $V3d_{xy}$ state. The second feature represents the transition of V2p electrons to orbitals with $3d_{xz/yz}$ character. Finally, the remainder of the L_3-resonance arises from transitions to V $3d_{x2-y2/z2}$ orbitals. Just beyond the V L_2 edge, the O K-edge corresponds to transitions of an electron from O 1s to O 2p states.

Substantial hybridization between V 3d and O 2p orbitals results in two distinct sets of resonances that are reflective of the crystal field splitting of the V 3d orbitals and have approximately t_{2g} and e_g* character.[60,61] These orbital symmetry assignments are further borne out by the polarized XANES spectra (Fig. I.6). In particular, the modulation of the intensity of features derived from V3d_{xy} states is particularly pronounced, being weaker at glancing angle incidence when the electric-field vector is orthogonal to the V_2O_5 layers and strongly enhanced at normal incidence with the electric-field vector is oriented along the *ab* plane of V_2O_5.[61] At the O K-edge, there is furthermore a significant modulation of the intensity of the t_{2g} feature as a function of the orientation of the polarization vector.

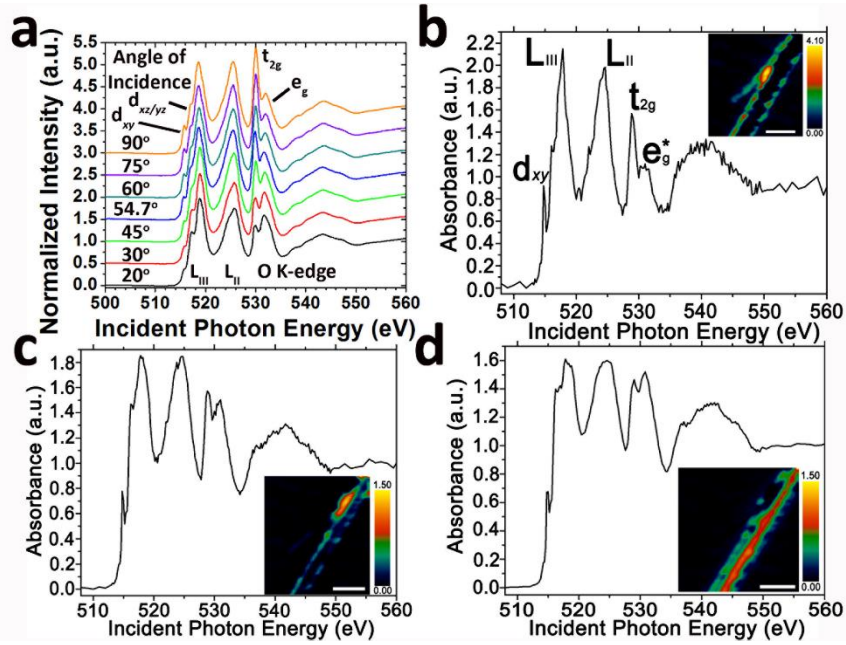

Figure I. 6: (a) Polarized XANES spectra acquired for oriented V_2O_5 nanowire arrays (shown in Fig. I.4c) with spectral assignments. (b) –(d) STXM component spectra measured for an individual $Li_xV_2O_5$ nanowire; the intensity maps corresponding to each spectral components is mapped in the inset in each case. Adapted from 45.

Figure I.3 indicates the evolution of the V L- and O K-edge spectra with increasing lithiation. Juxtaposition of the unlithiated and lithiated sample show two main effects on the lithiated sample: 1) the diminution of the V $3d_{xy}$ feature (caused by the localization of an electron in the orbital, making the feature "dark" as a result of Pauli blocking) and 2) the reversed ratio between t_{2g} and e_g* features at the O K-edge (caused by the lifting of electron spin degeneracy as well as by structural lattice distortion). Figures I.6b—d map the spatial localization of different spectral components (*vide infra*).

Further insight into electronic structure of lithiated V_2O_5 is derived from the sensitivity of the transition metal K-edge to its local coordination environment. First, the reduction of vanadium centers upon lithiation is observed as a shift of the K-edge primary onset that arises from V 1s to V 4p states to lower energies. At energies just below the main edge, a pre-edge feature arises from transitions from the V 1s to hybrid V 3d-4p states that arise as the V coordination diverges from octahedral. As such, this feature is especially sensitive to V site oxidation state and coordination symmetry.[59,98–100] Using a 2D formalism for spectral analysis developed by Chaurand *et al.*, it has been shown that that the peak centroid for the pre-edge feature reflects reduction of the average oxidation state, whereas the decreasing intensity of the feature suggests a change of local symmetry from square pyramidal to distorted octahedral.[59] Additionally, the deconvolution of multi-phase mixtures present in the XANES spectra can be done using techniques such as

principal component analysis (PCA) and multivariate curve resolution (MCR).[101,102]

The development of X-ray microscopy methods as depicted in Figure I.2b has allowed for development of a rich picture of local inhomogeneities. Figures I.5b—d illustrate the use of STXM as a probe to visualize the formation of concentration gradients and phase separation within a single particle of $Li_xV_2O_5$.[45] Detailed analysis of the lithiated sample by region of interest analysis allows for the deconvolution of the total spectrum into three distinct spectral components corresponding to different levels of lithiation as measured by the relative intensity of the $3d_{xy}$ feature at the VL_3-edge and ratio of t_{2g} and e_g* intensities at the O K-edge. Mapping the components in real space allows for distinctive domains to be identified; these domains reflect the stabilization of different Li-ion concentrations across the nanowires. Based on DFT+U calculations, the localization of electron density and the observation of "hot stripes" in Figures I.6b—c stem from (i) stage ordering phenomena wherein initial insertion of Li-ions results in the expanded layers preferentially inserting subsequent Li-ions to the point of saturation instead of insertion of Li-ions within adjacent pristine layers; and (ii) stabilization of small polarons derived from coupling of an electron with a lattice distortion.[45] Propagation of the small polaron across the lattice is energetically expensive and is thought to substantially underpin the poor rate performance of α-V_2O_5 as a cathode material.[45]

X-ray microscopy has been further deployed at more extended length scales to study inhomogeneities across multiple particles within an electrode.[40,46,103,104] These measurements have allowed for mapping of intercalation gradients dependent on the separation between particles; the average size of the particles; and the charging rate.[52,103–107] As a case in point, for Li_xFePO_4, various models have been advanced including particle-by-particle transformation ("mosaic instability") and concurrent intercalation that differ vastly in the proposed sequence of phase progression.[40,46,52,104,108–111] Delmas and collaborators have observed particle-by-particle lithiation,[52] which necessitates gain of Li-ions by one particle at the expense of another depending on local current densities and the transformation barrier.[54] Lim *et. al.* have monitored the evolution of intercalation/deintercalation process in $LiFePO_4$ with respect to rate of charge.[46] Their results suggest that highly localized heterogeneities in reaction rates of the lithiation/delithiation processes in $LiFePO_4$ determine if it follows a solid-solution mechanism or proceeds through nucleation and growth of a Li-rich (or poor phase).

Lithiation of other ternary vanadium oxides has also been studied. The *β*-phase of $Ag_xV_2O_5$ can be reversibly cycled between 1.5 and 3.6 V and has found extensive use as a cathode material for primary Li-ion batteries used in implantable defibrilators.[112,113] Lithium-ion insertion within the tunnel framework appears to be accompanied by extrusion of Ag-nanoparticles, which further serve to increase the conductivity of the cathode material.[112] The facile accessibility of multiple redox processes (reduction of Ag^+ to metallic Ag, reduction of V^{5+} to V^{4+} and further

reduction of V^{4+} to V^{3+}) renders these materials particularly useful. The lithiation of a series of ternary copper vanadium oxides have also been reported including $Cu_{2.33}V_4O_{11}$ and $Cu_{1.1}V_4O_{11}$, which exhibit stable capacities approaching 250 and 260 mAh/g, respectively.[114,115] These materials are constituted from layers of V_4O_{11} units and despite not being classical intercalation hosts undergo an unusual electrochemical reaction with Li ions wherein lithiation drives the reversible extrusion and disappearance of Cu dendrites accompanied by reversible amorphization and recrystallization of the parent electrode material. The open frameworks of the ternary vanadium oxides as illustrated in Scheme I. 1 further suggest that ion-exchange reactions beyond lithiation may allow for stabilization of metastable architectures not accessible from the elements.[116] Indeed, topotactic modification of perovskites have yielded entirely novel compounds and ion-exchange reactions of quantum dots have allowed for stabilization of remarkable nanoscale heterostructures.[116]

A detailed understanding of Li-ion insertion and diffusion is imperative for rational cathode design and must encompass multiscale phenomena: surface reactions, local hopping barriers between interstitial sites, mesoscale transport across individual particles, and transport across the span of porous electrodes. While structural transformations have been elucidated in some detail, the consequences of electronic structure perturbations introduced by lithiation are relatively less explored but clearly no less important for charge diffusion. X-ray spectroscopy methods provide a powerful means of examining the alteration of

valence and conduction band states in proximity to the Fermi level and allow for development of orbital-specific descriptions of charge localization and potential diffusion pathways. The use of hard X-ray photoemission spectroscopy allows for the valence band to be probed for the bulk and not just the surface.[45,47,67,78] When coupled to microscopy methods, XAS methods yield compositional maps with nanometer-scale spatial resolution and allow for evaluation of lithiation gradients and phase inhomogeneities across individual particles and multiparticle networks.

This dissertation focuses on the unraveling of the mechanistic details of lithiation processes and accompanying phase transformations in V_2O_5, in an effort to develop a new paradigm of rational design, both as it pertains to atomistic design of materials as well as mesoscale design of electrodes. Chapter III discusses the differences in phase progression and kinetics of lithium uptake for different sized particles, and highlights a relationship between particle size and phase homogeneity. In chapter IV, X-ray absorption spectroscopy is used to discuss the structural and electronic changes incurred upon low overpotential Li-ion insertion, as well as the mechanisms of phase progression with Li-ion insertion, and the statistical deconvolution of multiphase mixtures in the XANES spectra. Finally the mechanistic insights gained are applied in chapter V, wherein the presentation of a novel 1D-tunneled polymorph of V_2O_5 is presented which minimizes the diffusion barriers that limit the performance of single-layer V_2O_5, enabling facile Li-ion transport and eliminating phase inhomogeneity.

CHAPTER II

SCALABLE HYDROTHERMAL SYNTHESIS OF FREE-STANDING VO_2 NANOWIRES IN THE M1 PHASE*

II.1 Introduction

Vanadium (IV) dioxide, VO_2, has attracted significant research interest owing to its orders-of-magnitude first-order phase transition between insulating and metallic states that occurs at ca. 67°C in the bulk.[4,117,118] The transition temperature, T_{MIT}, is uncommonly close to room temperature, and this fortunate circumstance has inspired considerable interest in device architectures that can take advantage of the abrupt switching of electrical and optical properties accompanying this phase transition.[4,117] A partial list of proposed device architectures that have been experimentally realized (to varying extents) includes Mott field transistors,[117,119] spectrally selective thermochromic glazings for "smart window" applications,[120] frequency-agile metamaterials for electromagnetic cloaking,[121] periodic oscillators,[122] memory devices based on two-terminal device configurations (mimicking neuromorphic circuits),[123,124] and strain sensors.[125–127] In addition, VO_2 has long served as an accessible system for fundamental explorations of strongly correlated behavior in materials.[4,117,118,128] The occurrence of a structural phase transformation between monoclinic and tetragonal phases in close proximity to the electronic transition temperature has led to contrasting views regarding the relative importance of electron—

*Reprinted with permission from "Scalable Hydrothermal Synthesis of VO_2 Nanowires in the M1 Phase" by G. A. Horrocks, S. Singh, M. F. Likely, G. Sambandamurthy, and S. Banerjee, *ACS Appl. Mater. Interfaces*, 2014, **6**, 15726-15732.

electron and electron—phonon interactions in VO_2.[4,14] However, it must be noted that the electronic and structural phase transitions can be separated for both thermally induced and photoactivated processes[12,15,16] in this system. Scaling VO_2 to finite sizes allows for more robust accommodation of the strain generated during the structural phase transformation (in other words, enables protracted thermal cycling without cracking) and additionally allows for modification of the phase diagram to suppress the transition temperature and stabilize metastable phases.[127,129–131]

From a synthetic perspective, VO_2 is a challenging target since it is only stable within a narrow sliver of the V—O binary phase diagram[34] where it resides in immediate proximity to oxygen-deficient Magneli and Wadsley-type phases wherein extended defects such as crystallographic shear planes facilitate accommodation of periodic arrays of oxygen vacancies.[132] The magnitude of the metal—insulator transition (for both optical and electrical properties) and T_{MIT} thus vary sensitively as a function of oxygen stoichiometry in VO_2.[34–36,133] Optimal control of the stoichiometry of VO_2 and thereby materials exhibiting the most pronounced (above three orders of magnitude) phase transitions have been realized thus far primarily by physical vapor deposition methods such as high-temperature vapor—solid deposition,[17,26,28,117] molecular beam epitaxy,[134,135] pulsed laser deposition,[130] and sputtering.[35,120] In these methods, the structure can be dictated based on epitaxial homology with an underlying lattice-matched substrate, whereas the stoichiometry can be precisely defined by tuning the background pressure, precursor concentrations, and annealing conditions. Such variables tend to be more difficult to control in solution-phase syntheses and indeed homogeneous nucleation tends

to favor stabilization of a metastable VO_2(B) structure with the exception of reactions performed under high pressures.[32,136,137]

Solution-phase methods are desirable for improved scalability (applications such as deployment in thermochromic glazings and functional coatings will require much greater quantities of material than can possibly be obtained by physical vapor deposition), cost-effectiveness, and remain of paramount importance for obtaining high-quality materials that are decoupled from substrates. The last listed aspect is especially important for obtaining materials that can be cast onto arbitrary substrates as desired for a specific application although modulation of the metal—insulator transition of VO_2 via lattice matching or substrate coupling also remains a rich area of study.[138] Obtaining free-standing nanowires further allows for deployment of surface functionalization and colloidal chemistry approaches thereby enabling tuning of properties, incorporation within different matrices, and permitting the rational design of multicomponent nanocomposites. Sol—gel[139,140] and hydrothermal approaches[29–32] have previously been used to prepare VO_2 nanowires; the incorporation of W and Mo dopants appears to facilitate stabilization of the rutile (and upon cooling to room temperature, the M1 monoclinic) phase of VO_2. However, examples of solution-based preparation of undoped VO_2 in nanoscale form are rare, and the materials thus prepared tend to be inferior to thin films and nanobeams obtained by vapor transport methods in terms of the magnitude of the switching evinced for the electrical conductivity and optical transmittance across the phase transition.[20,31–33]

In this work, we report a robust synthetic methodology that provides access to stoichiometry-controlled solution-derived VO_2 nanowires exhibiting massive metal—

insulator transitions. Almost four orders of magnitude switching of resistance has been reproducibly realized for over 30 single-nanowire devices incorporating nanowires prepared by this method. For the prepared nanowires, both the structural and the electronic phase transitions have been characterized. The availability of free-standing VO_2 nanowires allows for examination of the intrinsic phase diagram of the solution-derived nanostructures without obscuration from substrate coupling and strain imposed by mismatches in the coefficient of thermal expansion between the lattice and the substrate. Raman spectroscopy has been used to study the structural phase transformation given the drastically different Raman signatures of the two phases. The electronic phase transition in these nanowires has further been examined by individual nanowire electronic transport measurements after integrating the nanowires within device architectures.

II.2 Experimental

VO_2 nanowires were prepared by a stepwise hydrothermal method. First, nanowires of $V_3O_7 \cdot H_2O$ were prepared *via* the hydrothermal exfoliation and reduction of bulk V_2O_5 (Sigma-Aldrich, 98%) by oxalic acid dihydrate (J.T. Bruker). In a typical reaction, 300 mg of V_2O_5 was placed in a 23 mL PTFE cup with 16 mL of deionized water (ρ = 18.2 MΩ/cm, Barnstead International Nanopure Diamond) and 75 mg of oxalic acid dihydrate. The cup was then placed in a sealed autoclave and heated at a temperature of 210°C for 72 h. This reaction can be reproducibly scaled using a 125 mL autoclave. For the large-scale reactions, 1.6304 g V_2O_5 powder and 451 mg of oxalic acid dihydrate were reacted hydrothermally in 75 mL of deionized water. The resulting nanowires were filtered and washed with copious amounts of water and acetone.

The isolated $V_3O_7 \cdot H_2O$ nanowires were then subsequently hydrothermally reduced by a 1:1 *v/v* mixture of water and 2-propanol (Fisher). In a typical reaction, 300 mg of the $V_3O_7 \cdot H_2O$ nanowires were placed in a PTFE cup with 8 mL of deionized water and 8 mL of 2-propanol. The PTFE cup was then placed within a sealed autoclave and heated at a temperature of 210°C for 72 h. The obtained mixture of VO_2(A) and VO_2(B) nanowires was isolated by filtration and washed with copious amounts of deionized water and acetone. Both hydrothermal reactions are performed at pressures less than 125 bar enabling the use of low-pressure autoclaves. The collected nanowires (mixture of VO_2(A) and VO_2(B)) were subsequently annealed at 475°C under an Ar atmosphere in a tube furnace while maintaining an Ar flow of 150 mL/min for 1 h; VO_2 nanowires crystallized in the M1 phase were recovered after cooling to room temperature.

Powder X-Ray diffraction (XRD) characterization of the prepared materials was performed using a Rigaku Ultima IV diffractometer (Cu Kα radiation; voltage of 40 kV, current of 44mA). JADE 8.5 was used for pattern fitting and phase identification. Differential scanning calorimetry (DSC, Q200 TA Instruments) was performed between -50 and 150°C under a flowing Ar atmosphere. The morphology and purity of the obtained nanowires was examined by scanning electron microscopy coupled with energy dispersive x-ray spectoscopy (SEM, EDX, Hitachi SU-70 operated at 15 kV) and transmission electron microscopy (TEM, JEOL JEM-2010 operated at an accelerating voltage of 200 kV). TEM samples were prepared by dispersing nanowires in 2-propanol by ultrasonication, and casting onto 400 mesh copper grids coated with a formvar/cabon film.

Raman spectra were acquired using a Jobin-Yvon Horiba Labram HR instrument coupled to an Olympus BX41 microscope. The 514.5 nm line from an Ar-ion laser was used as the excitation source. The Raman spectra were acquired using a 1800 lines/mm grating yielding a spectral resolution of better than 2 cm^{-1}. The *in situ* heating measurements were performed under a N_2 atmosphere using a sealed THMS 600 thermal stage from Linkam Scientific Instruments. The samples were left to equilibrate at each temperature for 300 s prior to acquiring the Raman spectrum.

Electrical transport measurements of single nanowires were performed using a variable temperature cryostat insert. The nanowires were first dispersed and cast onto Si/SiO_2 (300 nm) substrates. Subsequently, Au electrodes (70 nm) were patterned after defining contacts to the nanowires using a combination of electron-beam lithography and photolithography; Cr metal (5 nm) was used as the adhesion layer. Resistance *versus* temperature measurements were acquired for both heating and cooling cycles between 27 and 107°C. Current *versus* voltage measurements were acquired using single-nanowire devices fabricated by the same method. The current across the devices was measured by sweeping the voltage between 0 and 2 V while holding temperature constant.

II.3 Results and Discussion

The prepared nanomaterials have been characterized across the successive reductive steps as well as across the structural and electronic phase transitions of VO_2. Figure II.1 illustrates the characterization of the nanowires through each step of the synthetic

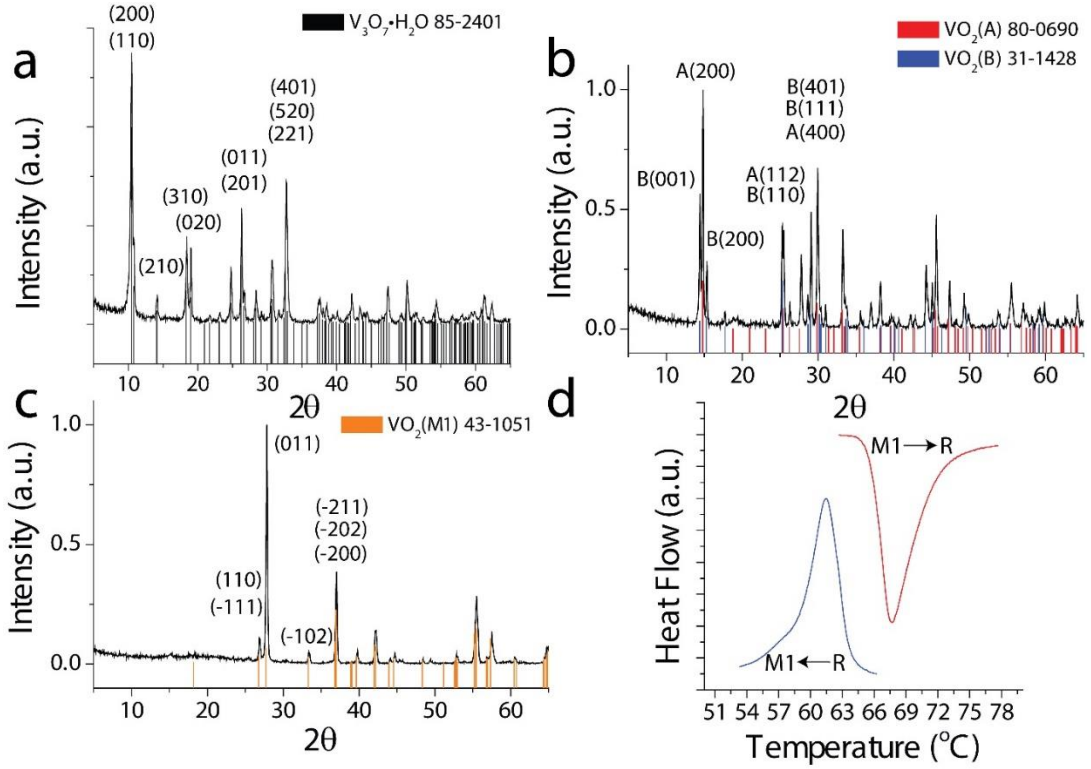

Figure II. 1 XRD patterns acquired for (A) as-synthesized $V_3O_7{\cdot}H_2O$ nanowires; (B) initial mixture of VO_2 (A) and VO_2 (B) metastable phases obtained by reduction of $V_3O_7{\cdot}H_2O$ nanowires with a 1:1 (*v*:*v*) mixture of deionized water and 2-propanol; and (C) VO_2 nanowires after annealing at 475°C for 1 h in an Ar ambient; (D) DSC plot of M1 VO_2 nanowires showing an exothermic transition upon heating centered at 67.5°C and an endothermic transition upon cooling centered at 63.1°C. Reprinted from 37.

approach. The hydrothermal reduction of V_2O_5 by oxalic acid yields phase-pure $V_3O_7{\cdot}H_2O$ nanowires as per the following reaction:

$$3V_2O_5\,(s) + H_2C_2O_4\,(aq.) \xrightarrow{hydrothermal} 2V_3O_7{\cdot}H_2O\,(s) + 2CO_2\,(g) \qquad (1)$$

Figure II.1a indicates the XRD pattern acquired for these nanowires, which can be indexed to PDF# 84-2801. Figure II.2a and b show SEM and TEM images of $V_3O_7{\cdot}H_2O$ nanowires. The nanowires are 183±34 nm wide and range up to hundreds of microns in length. The

subsequent hydrothermal reduction of V_3O_7 using a mixture of 2-propanol and water as per

$$V_3O_7{\cdot}H_2O\ (s) + 2(CH_3)_2CHOH \xrightarrow{hydrothermal} 3VO_2\ (s) + 2(CH_3)_2CHO\ (aq.) + 2H_2O\ (l) \quad (2)$$

yields a mixture of the metastable VO_2(A) (PDF#: 80-0690) and VO_2(B) (PDF#: 31-1428) phases as illustrated by the XRD pattern shown in Figure II.1b. Oxalic acid and citric acid can also be used for the reduction of $V_3O_7{\cdot}H_2O$ and do yield a similar mix of VO_2(A) and VO_2(B) phases; however, the obtained materials are poorly defined in terms of their morphologies. 2-propanol appears to be the optimal reducing/structure-directing agent for obtaining well-defined nanowires. Reaction using just deionized water yields the metastable VO_2(B) phase but with a substantial amount of other mixed-valence vanadium oxide phases resulting from incomplete reduction. While reaction with other small aliphatic molecules yield similar mixtures of the two metastable phases after reduction, the overall particle size remained significantly larger than that achieved via the 2-propanol reduction. Upon annealing the products of the 2-propanol reduction reaction, the M1 phase of VO_2 is recovered as illustrated in Figure II.1c. At temperatures less than 450°C, there is evidence for substantial remnant VO_2(B). The VO_2(A) and VO_2(B) phases have less close packed frameworks with greater void space and have been predicted to undergo an order—disorder transition with eventual recrystallization into the rutile phase of VO_2, which subsequently transforms to the M1 monoclinic phase upon cooling.[136] Fortuitously, for loosely packed powders of VO_2 nanowires, the transformation is induced well before initiation of sintering, allowing for retention of the morphology originally defined by the

hydrated V_3O_7 nanowires. Conversely, annealing under an air or oxygen ambient under the same conditions yields phase-pure V_2O_5 nanowires without appreciable sintering and with similar dimensions.[48] Note that the annealing step is performed on the powder samples and the resulting nanowires synthesized on the multi-gram scale are available for incorporation onto arbitrary substrates or within host matrices including polymers.

The thermally and electrically induced M1→R phase transition is first order in nature and accompanied by a substantial change in thermal conductivity as well as a discontinuous jump in carrier concentration. Being a first-order phase transition, the structural phase transformation is associated with a substantial latent heat and alteration of the specific heat capacity.[141,142] The latent heat at the phase transition arises from the structural distortion of the lattice and the change in entropy of the conduction electrons (which are no longer localized in the insulating state).[20,141] Figure II.1d shows pronounced endothermic and exothermic DSC profiles for the VO_2 nanowires centered at 67.5 and 61.3°C upon heating and cooling, respectively. The FWHM of the DSC profiles are 3.8 and 3.0°C, respectively. These FWHM values are much narrower than the 10—15°C FWHMs observed previously for solution-derived undoped and W-doped VO_2 nanowires.[29] As an ensemble measurement across multiple nanowires, the width of the observed transition reflects the distribution of temperatures at which the nanowires are undergoing the metal—insulator transition. The narrower ensemble DSC profile implies greater homogeneity of the transition temperature across the nanowire sample indicating much tighter stoichiometric control of the prepared nanowires. The latent heat of the

endothermic insulator→metal transition is determined to be 7.88 J/g based on integrating the area of the transition.

Figure II.2e depicts SEM images of the monoclinic VO_2 nanowires after annealing and shows well-defined nanowires with rectangular cross-sections and lengths on the order of tens of microns, while EDX analysis indicates no inadvertent dopant inclusion during the synthetic procedure. TEM images of the nanowires indicate an average width of 187 ± 77 nm (Fig. II.2f), essentially retaining the lateral dimensions of the original $V_3O_7{\cdot}H_2O$ precursor nanowires with some fragmentation resulting from the order—disorder transition discussed above. Lattice-resolved HRTEM images (Fig. II.2g) and the selected area electron diffraction (SAED) patterns acquired for an individual nanowire (Fig. II.2h) corroborate the phase assignment to the M1 monoclinic phase of VO_2. The lattice-resolved HRTEM image in Figure II.2g indicates an interplanar separation of 0.481 nm, which corresponds to the separation between the (100) planes of monoclinic VO_2.

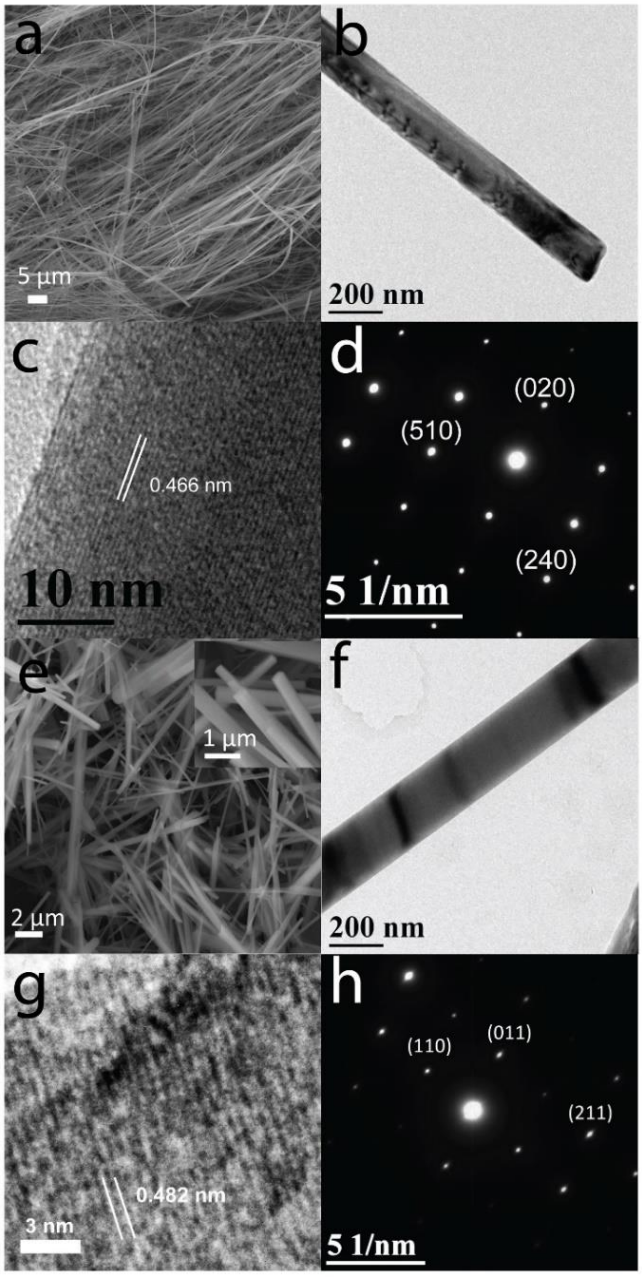

Figure II. 2 (A) SEM and (B) TEM images of $V_3O_7{\cdot}H_2O$ nanowires. (C) Lattice-resolved HRTEM image of $V_3O_7{\cdot}H_2O$ nanowires indicating an interplanar separation of 0.466 nm corresponding to the spacing between (020) lattice planes. (D) Indexed SAED pattern acquired for an individual $V_3O_7{\cdot}H_2O$ nanowire. (E) SEM image of monoclinic VO_2 nanowires with the inset indicating rectangular cross-sections. (F) TEM image of a monoclinic VO_2 nanowire. (G) HRTEM image of a monoclinic M1 phase VO_2 nanowire indicating an interplanar separation of 0.482 nm. (H) Indexed SAED pattern acquired for an individual monoclinic VO_2 nanowire. Reprinted from 37.

Raman microprobe analysis provides an excellent spatially localized probe of the structural progression of the phase transition in VO_2.[27,143–145] The M1 monoclinic, M2 monoclinic, triclinic, and rutile phases of VO_2 have distinctive Raman spectral signatures arising from their varying local symmetry. The rutile and M1 phases crystallize in $P4_2/mnm$ (D_{4h}^{14}) and $P2_1/c$ (C_{2h}^{3}) space groups, respectively, with the latter predicted to have 18 Raman-allowed modes, nine each of A_g and B_g symmetry.[27,146] Raman spectra have been acquired for individual VO_2 nanowires (by dispersing the nanowires shown in Fig. II.2e on a glass substrate) as a function of temperature across the metal—insulator transition. The spectra for a representative nanowire are depicted in Figure II.3. The modes observed at low temperatures can be assigned to the M1 monoclinic phase of VO_2 with the symmetry assignments denoted in the figure derived from group theory considerations and previously published polarized Raman spectroscopy studies.[27,146,147] In contrast, the rutile phase has a much lower Raman cross-section and does not exhibit distinct modes in keeping with its metallic character (the laser skin depth is also greatly diminished by the much greater concentration of carriers in the metallic phase). Upon heating under a nitrogen ambient, the Raman spectra does not show much of a change until between 64 and 65°C an abrupt and sudden loss of all Raman-active modes is evidenced, indicating complete conversion to the metallic rutile phase. Remarkably, the transition is not preceded by any discernible attenuation of intensity or shifts of the Raman modes suggesting that the entire nanowire is transformed as a single domain (within the limits of experimental resolution). The Raman modes are further recovered upon cooling back to 64°C.

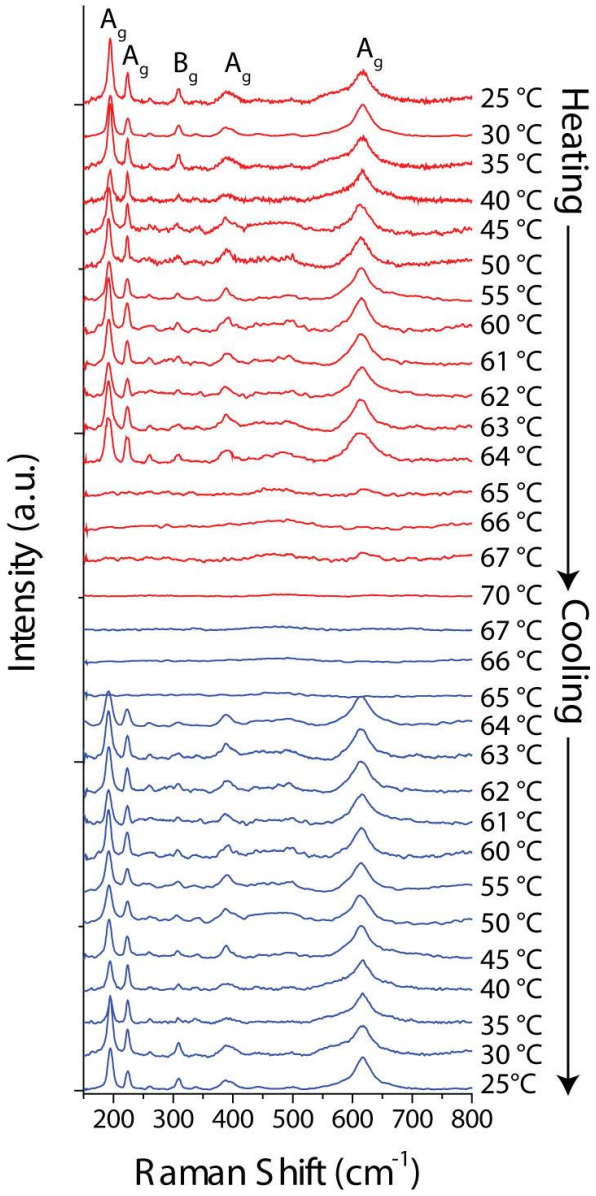

Figure II. 3 Raman spectra acquired for an individual VO_2 nanowire upon heating and cooling across the metal—insulator transition. Upon heating, all Raman-active modes of the insulating M1 monoclinic phase are lost when the nanowire transitions to the high-symmetry metallic rutile phase between 64 and 65°C. The nanowire then transitions back to the M1 phase upon cooling between 65 and 64°C. Reprinted from 37.

Unlike VO_2 nanobeams coupled to substrates grown by vapor transport, there is no evidence in the Raman data for stabilization of the M2 phase (which crystallizes in the C_{2h}^5 space group and is characterized by a splitting of the A_g mode at 221 cm^{-1} and a shift of the A_g mode at 607 cm^{-1} to 649 cm^{-1}). Consistent with the narrow lineshapes of the ensemble DSC profiles, the sharp discontinuities noted here are surmised to result from improved homogeneity in stoichiometry across the nanowires. The pronounced switching behavior thought to be characteristic of stoichiometric VO_2 is most patently manifested in electrical transport measurements of individual nanowires across their metal—insulator transitions induced by temperature or voltage, as depicted in Figure II.4. Note that the nanowires have been solution cast (from 2-propanol dispersions) onto Si/SiO_2 (300 nm) substrates and no effort has been invested in liberating the nanowires from the substrate as was previously required to observe abrupt transitions for nanobeams deposited by vapor transport where coupling to the substrate induces inhomogeneous strain.[13,28] Figure II.4a illustrates that the transition from the insulating to the metallic phase is characterized by a greater than three (almost four) orders of magnitude decrease in resistance across a span of just 0.1°C; the transition back to the insulating phase is similarly abrupt with the hysteresis of 13.2°C derived from the first-order nature of the transition. The Arrhenius behavior in the insulating phase of the nanowires is well fitted with $R(T) = R_0\exp[E_g/2kT]$ (where k is Boltzmann's constant and T is temperature) and yields an electrical bandgap

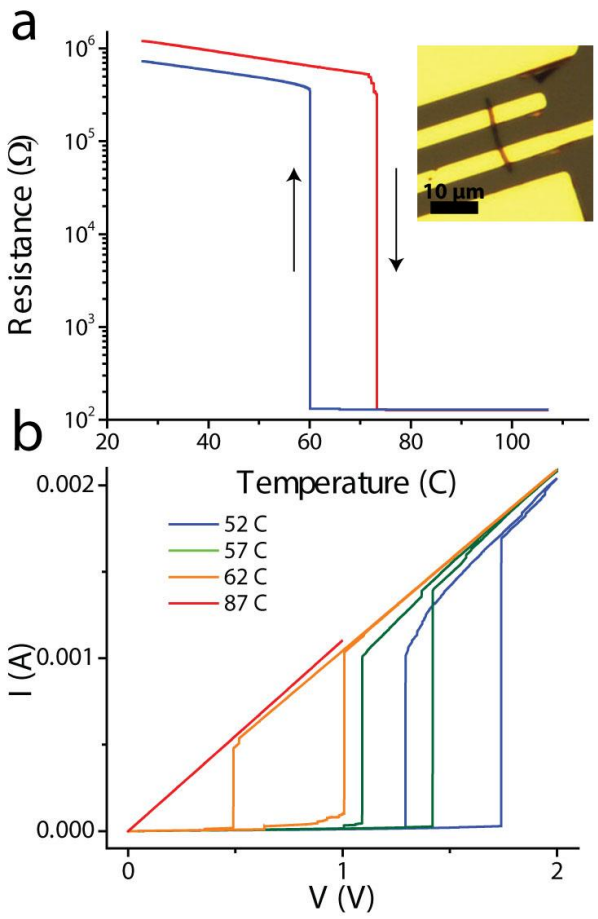

Figure II. 4 (a) Resistance *versus* temperature measured for an individual-nanowire device indicating a transition between the insulating and metallic phases within 0.1°C at 73.3°C. The inset depicts an optical micrograph of the device. (b) Current *versus* voltage measurements for single-nanowire devices show abrupt voltage-driven transitions between the insulating and the metallic phases at temperatures below the transition temperature. The threshold voltage required to induce the insulator→metal transition is clearly decreased with increasing temperature. Reprinted from 37.

(E_g) of 600 meV, which is consistent with the values observed for suspended VO_2 nanobeams and indeed the optical bandgap of VO_2.[13] The bandgap, for these nanowires is significantly greater than the 80—200 meV values observed previously for solution-grown W-doped VO_2 nanowires[33] and confirms the tight control of stoichiometry and the absence

of inadvertent doping. Dimensional confinement in high-crystalline-quality nanostructures limits the number of possible nucleation sites and thereby can kinetically inhibit initiation of a phase transformation, yielding a greater hysteresis than observed in the bulk.[148] Of the thirty devices tested (each comprising an individual nanowire), the insulator→metal transition has been observed at a temperature of 71 ± 2°C, with the transition spanning no greater than 1°C. The abruptness of these transitions are in stark contrast to previous observations for hydrothermally prepared and especially doped nanostructures that typically show broader insulator→metal (or metal→insulator) profiles spanning 3—5°C for undoped VO_2 and ranging up to 10—20°C for doped samples.[13,22,30,129,149] The current *versus* voltage plots depicted in Figure II.4b are analogously characterized by sharp switching of the conductivity above a threshold voltage with the threshold voltage required to trigger the transition being inversely correlated to temperature. For temperatures below T_{MIT}, upon reaching the specific threshold voltage, a discontinuous increase in current is evidenced indicating a transition to a metallic phase. In the insulator→metal direction, the threshold voltage (V_{th}) for the transition shows an approximately exponential V_{th} α $\exp(-T/T_0)$ dependence that is characteristic of a charge delocalization in a charge ordered system.[20,150,151] In other words, the non-equilibrium application of an electric field injects carriers into the nanowires. Beyond a critical carrier density, Thomas—Fermi screening of bound excitonic states by the injected free carriers leads to an abrupt increase of the carrier density, resulting in transformation of the system to a metallic state even at low temperatures. At low temperatures, a sharp singular, almost step-function-like, jump is noted upon reaching the

threshold voltage; at temperatures approaching (but less than) T_{MIT}, a number of discontinuous jumps are observed that are attributed to progression of the phase transition through avalanche-type events and the stabilization of a strongly correlated metallic phase.[152,153] Thermal effects are convoluted with the electric-field induced effects closer to the transition temperature, whereas the electric-field-induced delocalization of charge ordering motifs is more clearly observed at low temperatures.[153] Above T_{MIT}, no voltage-induced metal—insulator transition is evidenced and instead a linear current *versus* voltage trace is observed indicating that the VO_2 nanowire is already in a metallic state. The abruptness of the metal—insulator transition evidenced in both the thermal and electric-field-induced transitions further corroborates the good crystalline quality and tight stoichiometric control of the VO_2 nanowires.

II.4 Conclusion

In conclusion, a novel stepwise hydrothermal methodology has been developed for preparing phase-pure VO_2 nanowires based on the initial oxalic acid reduction of V_2O_5 powders to $V_3O_7{\cdot}H_2O$ nanowires that are subsequently reduced to a mixture of VO_2(A) and VO_2(B) nanowires with the help of 2-propanol. The latter metastable phases are converted to the rutile phase of VO_2 upon annealing, allowing for recovery of monoclinic M1 VO_2 nanowires with controlled-stoichiometry upon cooling. The nanowires exhibit abruptly discontinuous phase transitions exceeding three (and approaching four) orders of magnitude in electrical transport measurements, as well as sharp ensemble DSC profiles and dramatic changes of Raman spectra at the transition temperature, suggesting that this solution-phase methodology yields VO_2 nanowires of comparable quality and carefully

controlled stoichiometry as derived from physical vapor transport methods. The electrical bandgap for the synthesized nanowires is 600 meV consistent with the optical bandgap of VO_2, verifying the close control of stoichiometry. The process devised here is scalable and yields free-standing nanowires that can be dispersed on arbitrary substrates or incorporated within composite materials.

CHAPTER III

FINITE SIZE EFFECTS ON THE STRUCTURAL PROGRESSION INDUCED BY LITHIATION OF V_2O_5: A COMBINED DIFFRACTION AND RAMAN SPECTROSCOPY STUDY*

III.1 Introduction

The pressing need to develop improved rechargeable Li-ion batteries exhibiting high power and energy densities for applications such as plug-in hybrid electric vehicles poses a formidable challenge for materials design.[6,154,155] Indeed, significant innovation in materials synthesis and processing will be required to optimize the disparate components of a Li-ion battery for reliable and safe operation over hundreds of cycles. Increasing the specific capacity and cyclabilty of the cathode lies at the heart of this puzzle. Based on remarkable enhancements of cycling stabilities, power densities, and specific charge capacities observed for both nanostructured anodes and cathodes, it is now abundantly clear that appropriately scaling certain materials to nanoscale dimensions, while certainly not an universal panacea,[3,72] can provide manifold advantages due to the improved ability of nanoscale materials to accommodate strain gradients inevitably introduced upon inhomogeneous electrochemical lithiation, an increased electrolyte interface derived from their high surface areas, operation of additive capacitative and pseudo-capacitative charge

* Reproduced with permission from "Finite Size Effects on the Structural Progression Induced by Lithiation of V_2O_5: A Combined Diffraction and Raman Spectroscopy Study." Horrocks, G. A.; Likely, M. F.; Velazquez, J. M.; Banerjee, S. *J. Mater. Chem. A* **2013**, *1*, 15265–15277. Reproduced by permission of the Royal Society of Chemistry.

storage mechanisms as a consequence of the increased surface areas, and the shorter diffusion path lengths within nanoscale materials that permit more facile insertion/extraction of intercalating ions.[70,72,73,156,157] Despite incontrovertible benefits to scaling materials to nanometer-sized dimensions, the mechanistic origins of improved performance and the altered phase stabilities of electrode materials at these dimensions remain poorly understood. In this study, we use Raman spectroscopy as a local structure probe in conjunction with powder X-ray diffraction to evaluate and contrast the structural phase progression introduced upon chemical lithiation of the layered V_2O_5 framework for micrometer-sized particles, free-standing nanowires, and substrate-aligned nanoplatelets. Scaling to finite size is found to profoundly alter both the kinetics of Li-ion insertion and the thermodynamic phase stability windows of the lithiated phases.

V_2O_5 and vanadium bronzes based on variations of the V_2O_5 structure with intercalated metal ions and varying connectivity between VO_6 polyhedra are attractive candidates for cathode materials because of their abundant sites for accommodating guest species, the accessibility of V^{5+}/V^{4+} and V^{4+}/V^{3+} redox couples, and the large free energy of the Li-ion insertion reaction.[1,3,156,158] Indeed, Scanlon *et al.* have predicted energies of Li-ion insertion approaching -2.78 eV/Li for lithiation to the initial α-$Li_xV_2O_5$ phase and as much as -3.58 eV/Li for lithiation to the subsequent γ-$Li_xV_2O_5$ phase.[77] However, the high-rate performance of these electrode materials is still not optimal and significant improvements in cycling stability and lifetime are required to make these otherwise inexpensive and naturally abundant materials viable candidates for use as cathode materials. Since the first proposal by Whittingham in 1976,[51] V_2O_5 has been examined as

a host for Li-ions in various avatars ranging from micrometer-sized particles to highly porous xerogels and aerogels, thin films of varying crystallinity prepared by physical vapor deposition, and nanostructures synthesized using hydrothermal or electrodeposition approaches.[72,75,156,158] Considerable variations in phase stability windows for different lithiated phases as a function of extent of discharge has been noted across these different morphologies with the frequent manifestation of two-phase windows.[75]

The abundant interstitial sites available within the open layered framework of V_2O_5 offer the additional benefit of not exhibiting the extreme volume changes that are commonly seen in lithium intercalation hosts such as the current state-of-the-art anode materials SnO_2 and Si.[81,82] Compared with the extreme volume changes exhibited by the insertion/alloying process of these two materials of ~240% and ~300%, respectively, for SnO_2 and Si;[81,82] the volume changes exhibited for V_2O_5 are significantly smaller. There is a moderate collapse of the overall structure through the reversible phase regime at $x < 1.0$, followed by expansion to the highly distorted γ-phase after $x = 1.0$. As such, lithiation to the ε- and δ-phases causes a ~25% volume reduction per V_2O_5 unit compared to the neat orthorhombic phase; and lithiation to the γ-phase is accompanied ~4% expansion relative to orthorhombic V_2O_5.[75]

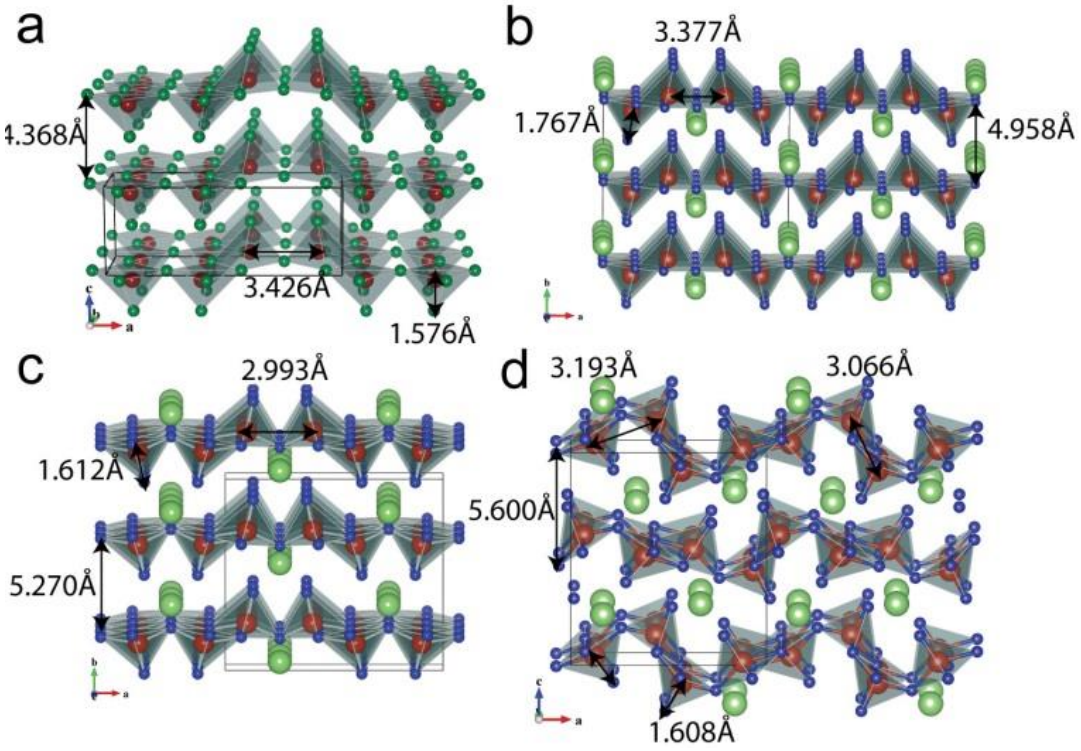

Figure III. 1 Crystal structures depicting (a) the orthorhombic phase of V_2O_5 (*Pmmn*); (b) puckering of layers upon Li-ion insertion for the ε-phase (*Pmmn*);[21] (c) increased puckering with stabilization of the δ-phase (*Amma*);[10] (d) rearrangement of square pyramids upon conversion to the γ-phase (*Pnma*).[4] The Li-ions are depicted as green spheres. The vanadium cations are depicted as red spheres surrounded by square pyramids with blue oxygen atoms at the corners. Reprinted from 48.

Figure III.1a depicts the orthorhombic crystal structure of V_2O_5, which can be conceptualized as sheets of alternating pairs of VO_5 square pyramids linked via corner and edge sharing (space group: *Pmmn*).[70,156,158] The layers are weakly electrostatically bound along the crystallographic *c*-axis with interstitial sites readily available between the layers. For relatively low discharge levels of $x < 1$ in $Li_xV_2O_5$, the distortions to the orthorhombic V_2O_5 lattice are relatively minor involving puckering of the layers and gliding motions.[81] Consequently, the strains engendered within the V_2O_5 lattice with increasing lithiation can

be accommodated through a range of subtle atomic rearrangements depending on the specific morphology of the putative cathode material, making available a wealth of accessible crystalline phases (including some that are metastable in nature) and allowing for facile interconversion between different phases.[81,82,86,159–161] Facile surface reconstruction and flexion of nanostructures can substantially alter the structural phase progression upon lithiation of V_2O_5 in this regime with significant consequences for storage capacities and particularly for high rate performance. Here, we compare the differences in structural phase progression upon lithiation of V_2O_5 for nanometer-sized crystalline V_2O_5 as compared to micrometer-sized particles that represent "bulk" behavior.

Initial explorations of the phase diagram of lithiated V_2O_5 relied on traditional high-temperature solid-state routes.[162–166] However, the room-temperature phase diagram of V_2O_5 has also been extensively examined by inserting Li-ions by electrochemical means[6,159,166] or *via* topotactic reaction of this layered framework with *n*-butyllithium or LiI. This chemical lithiation approach has been shown to parallel electrochemical lithiation with high fidelity and is based on the following reaction:[164]

$V_2O_5 + xC_4H_9Li \rightarrow Li_xV_2O_5 + \frac{x}{2}C_8H_{18}$ (butane and butene products have also been reported).

Indeed, we have adopted this chemical lithiation route in comparing the structural progression upon lithiation of crystalline V_2O_5 nanowires and nanoplatelet films to that of micrometer-sized grains.

Several room temperature phases of $Li_xV_2O_5$ are known to exist, with their stabilities dependent on the lithium content. Keeping in mind the caveat noted above for

the variabilities in the phase stability windows of different phases as a function of morphology, for bulk micrometer-sized grains, a consensus has evolved around the following structural progression:[3,6,75,159] an α-phase, only slightly distorted from the parent orthorhombic phase depicted in Figure III.1a, is stabilized for $x < 0.1$; an ε phase is observed for $0.35 < x < 0.8$ (Fig. III.1b, an incommensurate ε'-phase is distinguished above $x > 0.53$);[167] a puckered δ phase (Fig. III.1c) is stabilized for $0.88 < x < 1.0$; a strongly distorted γ phase emerges for $x > 1.0$ as depicted in Fig. III.1d; and a rock-salt ω phase is observed for $x \geq 3$.[6] For low extents of discharge, the α↔ε↔δ-phase transitions are entirely reversible and indeed these phases can also be interconverted by thermal annealing.[3,6,71,155] In stark contrast, in the bulk, lithiation beyond $x > 1$ results in irreversible transformation to the γ phase. A metastable γ' phase (but not the parent orthorhombic V_2O_5 phase or the slightly lithiated α phase) retaining the structural framework of the γ phase is recovered upon delithiation. Analogously, lithiation beyond $x > 2$ irreversibly transforms the material to the rock-salt ω-phase.[86]

While in the bulk, the ω framework is retained upon delithiation of the material, Cui and co-workers have exemplified the remarkably altered phase stabilities manifested for nanometer-sized particles by demonstrating complete reversion to the parent orthorhombic phase upon delithiation of ω-$Li_3V_2O_5$ nanowires using Br_2 solution as the oxidant.[71] For V_2O_5 nanowires grown by a vapor—solid process, these authors have further evidenced complete conversion to ω-$Li_3V_2O_5$ within 10s upon chemical lithiation with *n*-butyllithium, suggesting a Li-ion diffusion constant that is three orders of magnitude greater than in the bulk.[71] Analogously Whittingham's group has

systematically compared the capacities and cycling stabilities of a series of nano- and micrometer-sized V_2O_5 samples and has found that finite size effects play a major role.[3] Nanowires prepared via annealing $H_xV_4O_{10}{\cdot}nH_2O$ nanostructures initially synthesized via a sol—gel process show superior performance as compared to larger structures. Sides and Martin have shown a clear inverse correlation between the diameter of V_2O_5 nanorods prepared by a templated growth process and the specific discharge capacities obtained at low temperatures.[97] Martin and co-workers have also demonstrated a two-fold improvement in the high-rate capabilities of polycrystalline 115 nm diameter V_2O_5 nanorods grown by templated growth methods as compared to a 250 nm thin film.[168] This ability to accommodate and release lithium iona very quickly promises to provide gains in the power density of 3-D architecture cells.

A more detailed discussion of the structures of the lithiated phases is germane to obtaining mechanistic understanding of the lithiation process and unraveling the origin of finite size effects. Upon incorporation of lithium-ions in the interlayer sites, the apical oxygens of the VO_5 square pyramids tend to form coordinative interactions with the Li-ions, thereby pinching together the apices of the square pyramids, and initiating the puckering of the layers.[70,156,158] In this structure, the apical V—O bond lengths are extended and the corner shared oxygens are nudged slightly into the interlayer space (Fig. III.1).[70,156,158] For the α-phase, these alterations are slight and yield only modest changes in the unit cell parameters. However, much more pronounced puckering is evidenced with continued lithium incorporation, resulting in stabilization of the ε-phase (Fig. III.1b). In ε-$Li_xV_2O_5$, there is a considerable increase in the *c* parameter from 4.37Å to 4.54Å as the

intercalated lithium ions disrupt the weak electrostatic interaction between the layers (the *c*-parameter can increase to as much as 4.68Å for a metastable highly lithiated ε'-$Li_xV_2O_5$ phase).[1,169] The Li-ions occupy cubooctahedral cavities enclosed by eight oxygen atoms of one V_2O_5 layer and four oxygen atoms of the adjacent layer.[167] There is a concomitant decrease of the *a* parameter as a result of the puckering of the sheets, which brings the VO_5 polyhedra in closer contact.[163] With further incorporation of Li-ions, the δ-phase is stabilized as depicted in Figure III.1c. The inserted Li-ions have a tetrahedral local coordination geometry involving interactions between downward pointing vanadyl oxygens and distorted chaining oxygens pushing upwards from the layer below.[163] Most notably, alternate layers glide by half a unit cell parameter (*b*/2) along the crystallographic *b* axis, thereby resulting in a doubling of the unit cell parameter to 9.91Å.[3,6,155,163] None of these changes from the parent orthorhombic phase up to the δ-phase depicted in Figure III.1c invoke cleavage of covalent V—O bonds and thus proceed quite readily through atomic displacements and are entirely reversible. However, beyond $x = 1$, the γ-phase phase is stabilized (Fig. III.1d) with much more severe puckering and inversion of VO_5 square pyramids to yield an alternating up and down pattern instead of the alternating pairs of VO_5 pyramids observed for lower extents of Li-incorporation (Figs. III.1a—c).[3,6,155,170]

The γ-phase can be cycled with no structural change between $0 \leq x \leq 2$.[159] Discharge beyond the γ-phase yields the disordered rock-salt structure of the ω-phase up to a lithium content of $x = 3$.[159,169] In the bulk, this is another structurally irreversible phase with isostructural lithiation/delithiation possible between $0.4 \leq x \leq 2.65$.[3,159] Although, as noted above, a much altered phase diagram is noted for nanorods.[166] To recapitulate the room-

temperature phase diagrams of lithiated V_2O_5 observed in the bulk, lithiation of this material proceeds through a combination of solid-solution formation and structural transformations. Considerable heterogeneity is typical of lithiation processes in the bulk and the extents of lithiation are often different at surfaces and within the bulk of the material. Indeed, this is one possible reason for the two-phase coexistence regimes often observed upon lithiation of V_2O_5. Diffusion barriers formed at interfaces between the varying lithiated phases can serve to diminish high rate performance.

While X-ray diffraction techniques enable determination of the average structure, there has been increasing interest in using Raman spectroscopy as a local probe to examine structural distortions induced as a result of Li-ion incorporation.[75,89,171–181] Indeed, Raman spectroscopy has been used to track the lithiation of V_2O_5 for bulk powders[173–176] thin films,[177–180] and even *in situ* within an electrochemical cell.[89,172,173] Raman spectroscopy provides a sensitive measure of the coupling between different atoms and the distortions in symmetry, thereby serving as an especially excellent probe for tracking structural changes introduced within a single-phase regime. To consider the Raman spectra observed for the different phases, it is worth noting that orthorhombic V_2O_5 phase is characterized

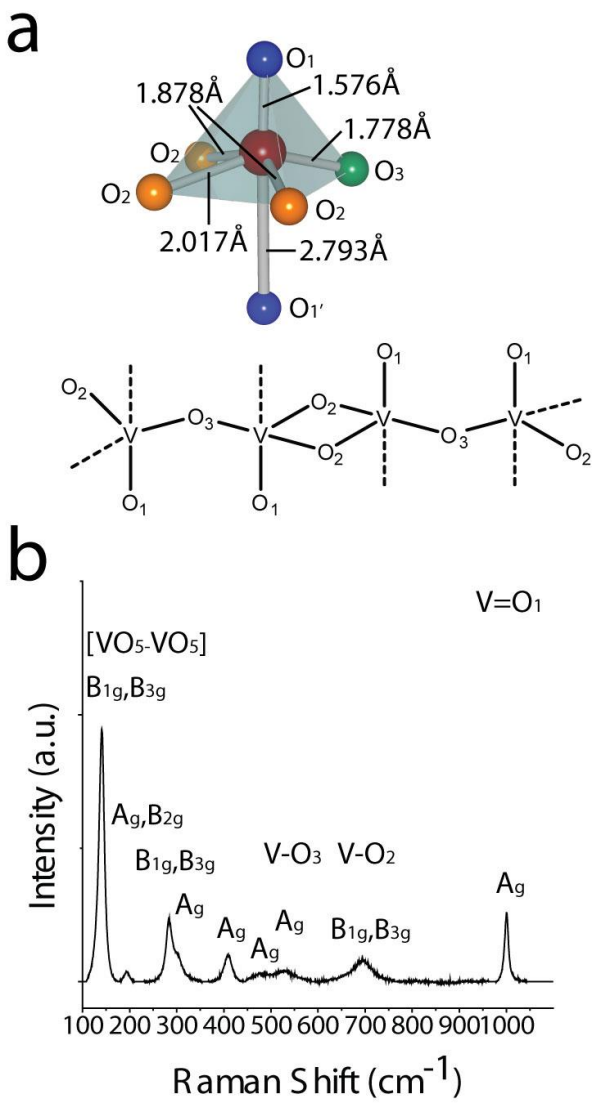

Figure III. 2 (a) Structure of a VO_5 square pyramid indicating bond distances to the crystallographically inequivalent oxygen atoms. The lower panel depicts two V_2O_5 repeating units illustrating the connectivity of the VO_5 square pyramids. (b) Raman spectrum of the orthorhombic phase of V_2O_5 indicating the mode assignments.[15,35] The spectrum has been acquired for the bulk powder sample. Reprinted from 48.

by a point group symmetry of D_{2h} with 21 allowed Raman modes.[179] Figure III.2a indicates the three different crystallographically inequivalent oxygen atoms within the unit cell of

V_2O_5 along with the relevant V—O bond distances. A short vanadyl oxygen (denoted as O1) is located at the apex of the square pyramid at a distance of 1.577Å from the vanadium center; bridging oxygens connecting the polyhedra are labeled O3 and are at a distance of 1.779Å from the vanadium sites; the pair of oxygen atoms labeled O2 connect the ladders and are characterized by a V—O distance of 1.878Å. Phonon state calculations and normal mode analyses have been previously published and are used here to assign the observed Raman bands.[51,169,174] Notably, to the best of our knowledge, no detailed study of the structural phase progression of V_2O_5 nanowires upon lithiation has thus far been reported. We report here a time course Raman and X-ray diffraction study wherein micrometer-sized V_2O_5 powders, V_2O_5 nanowires prepared by hydrothermal synthesis, and V_2O_5 nanoplatelet films deposited onto Si/SiO_2 substrates by chemical vapor transport are reacted with large molar excesses of *n*-butyllithium. The structural phase progression in each of the samples is tracked as a function of time.

III.2 Experimental

III.2.1 Synthesis of V_2O_5 Nanowires

V_2O_5 powder (Sigma-Aldrich 99.5%) was used as-received as the "bulk" sample in our measurements. The powder was constituted from grains with dimensions ranging from tens to hundreds of micrometers.

V_2O_5 nanowires were synthesized via hydrothermal reduction of bulk V_2O_5 (Sigma-Aldrich 99.5%) and oxalic acid (J.T. Baker), which yielded nanowires of V_3O_7 (see Fig. A.1, Supporting Information, for a XRD pattern and SEM image). These nanowires were subsequently oxidized in air at 300°C within a muffle furnace to yield

nanowires of V_2O_5. Prior to lithiation, paper-like nanowire samples were ground into fine powder to ensure even wetting by the electrolyte.

Nanostructured arrays of V_2O_5 were synthesized via chemical vapor deposition (CVD) using a method that we have previously reported.[61,182] Briefly, Si/SiO_2 (300 nm) substrates with a 1.5 nm Co layer (deposited by electron-beam evaporation) were placed in a single-zone tube furnace within a 1" diameter quartz tube. A ceramic boat containing V_2O_4 powder (Sigma-Aldrich 99%) was placed upstream of the substrates. The reactor was first evacuated to 10^{-3} torr and then heated to a temperature of 900°C. Upon reaching this temperature, Ar and O_2 flows were introduced and allowed to flow for 3-5 h, prior to allowing the furnace to cool naturally to room temperature.

III.2.2 Chemical Lithiation

Lithiation of all samples was carried out within a glove bag under an Ar ambient. Chemical lithiation was achieved via immersion of the powders or substrates for varying periods of time in a molar excess (4:1 $Li:V_2O_5$) of 2.5M *n*-butyllithium solution in hexanes (Sigma-Aldrich) diluted to 0.025M in toluene dried using a commercial solvent purification system (Innovative). Lithiated samples were washed with copious amounts of hexanes within the glovebag to remove unreacted precursors and reaction side products. Samples were then allowed to dry under an argon atmosphere. Delithiation was accomplished by immersion of the lithiated samples in pure liquid Br_2 for 2 h, followed by rinsing with copious amounts of hexanes.

III.2.3 Characterization

XRD patterns were collected using a Rigaku Ultima IV instrument (Cu Kα radiation, voltage 40 kV, current 44 mA). Pattern fitting and phase identification was achieved with the help of JADE 8.5. The morphology of the nanowires was evaluated before and after lithiation by scanning electron microscopy (SEM, Hitachi SU-70 operated at 25 kV equipped with an X-ray detector).

A Jobin-Yvon Horiba Labram HR instrument coupled to an Olympus BX41 microscope was used to acquire Raman spectra. The 514.5 nm line from an Ar-ion laser was used as the excitation source. The Raman spectra were acquired with spectral resolution better than 2 cm^{-1} using an 1800 lines/mm grating. The samples were placed within a sealed Linkam stage under a nitrogen atmosphere, and filters were used to attenuate the incident laser power to prevent photo-oxidation of samples, and to diminish the possibility of photo-induced phase transitions.

III.3 Results and Discussion

III.3.1 Electron Microscopy Observations

Figure III.3 shows SEM images of the as-prepared V_2O_5 nanowires prepared by hydrothermal synthesis and the nanostructured arrays prepared by chemical vapor deposition.[61,182] The as-prepared nanowires are obtained in the form of free-standing powders. These wires are 150-250 nm in diameter and range several hundreds of micrometers in length. The vertically oriented nanostructured arrays are platelet-like in shape with thicknesses on the order of 20—50 nm, lateral dimensions of several hundreds of nanometers, and heights ranging from several hundred nanometers to 5 μm (Fig. III.3b).

The nanowire morphology is seen to be retained upon chemical lithiation for the hydrothermally grown nanowires although the grinding process reduces their length (Fig. III.3c). As shown by Figure III.3d, vertically-integrated nanostructured V_2O_5 arrays remain well-adhered to the Si/SiO_2 substrate upon chemical lithiation and no discernible delamination has been observed across the surface.

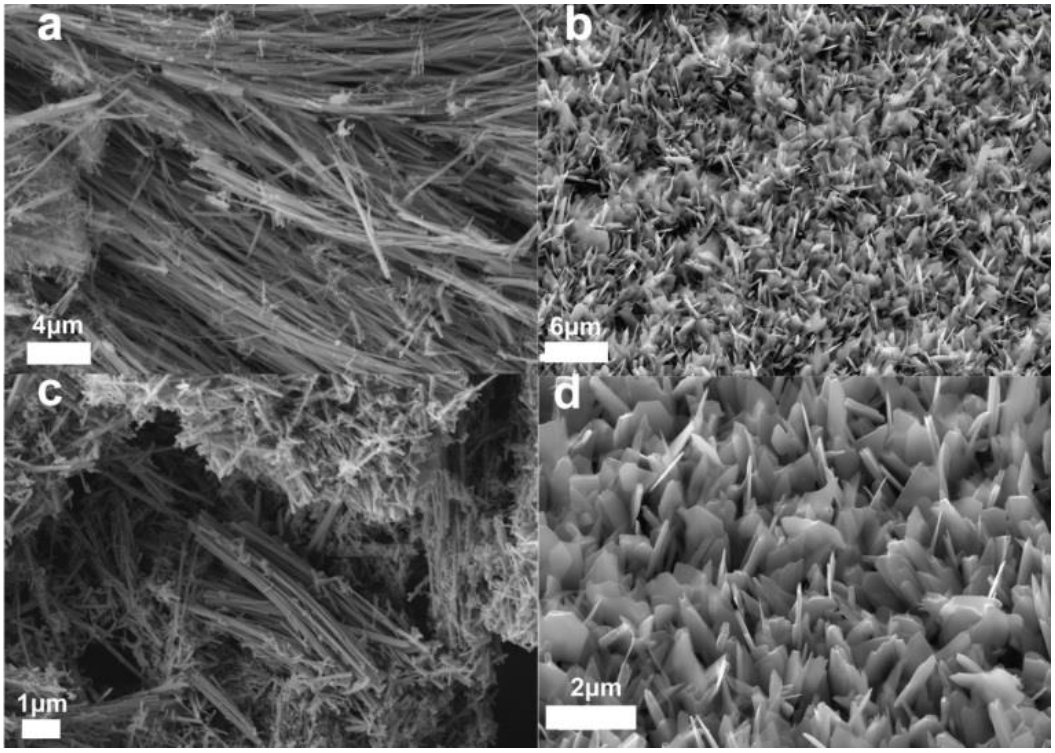

Figure III. 3 SEM images of (a) Hydrothermally grown V_2O_5 nanowires; (b) CVD-grown V_2O_5 nanostructures; (c) hydrothermally-grown V_2O_5 nanowires after grinding and reaction for 30 min with *n*-butyllithium; (d) CVD grown nanostructures after reaction for 30 min with *n*-butyllithium. Reprinted from 48.

III.3.2 Raman Spectroscopy of V_2O_5

As noted above, Raman spectroscopy is a powerful probe of local structure and provides a detailed perspective of structural transformations induced in V_2O_5 with increasing extent of lithiation.[75,173] Understanding the symmetry and displacements involved in the Raman modes of the starting compound V_2O_5 is critical to evaluating the structural progression. Figure III.2b depicts the Raman spectrum of orthorhombic V_2O_5. The mode assignments discussed below are based on normal mode analysis and previous phonon calculations.[75]

The low frequency modes at 105, 141, and 195 cm^{-1} have been attributed to external modes corresponding to the displacements of [VO_5] units with respect to each other.[71] The intensity of these modes thus serves as a good measure of long-range order within the V_2O_5 planes. Baddour-Hadjean and co-workers have ascribed the 195 cm^{-1} mode to translational displacements along the *x* axis (A_g+B_{2g} symmetry) and the 145 cm^{-1} mode to a mix of the shearing and rotation of the ladders with B_{1g} and B_{3g} symmetry, respectively.[75,89,169,171,172,178] Of the higher-frequency internal vibrational modes, a sharp Raman band is seen at 995 cm^{-1} and is assigned to the vanadyl stretch (V—O1) within the VO_5 square pyramids (Fig. III.2a shows the labelling of the different crystallographically inequivalent oxygen atoms).[75,89,169,171,172,178] The short bond length of 1.58Å (Fig. III.2a) is reflected in the high frequency of this stretch. The next highest mode at 698 cm^{-1} is ascribed to an anti-phase stretching vibration of the V—O2 bond (Fig. III.2b). Another mode at 524 cm^{-1} is ascribed to the stretching of inter-chain V—O2 bonds. The bending of the V-O3-V bridging unit gives rise to a relatively weaker band at 476 cm^{-1}. Two other

modes at 403 and 294 cm^{-1} can be assigned to bond rocking oscillations involving the apical oxygen (O1) atoms.[75,89,169,171,172,178] The *z*-motion of intra-ladder oxygen atoms gives rise to a mode at 302 cm^{-1}. While all of these modes show some change upon lithium insertion, the [VO_5-VO_5] mode at 145 cm^{-1} and the vanadyl oxygen stretch at 995 cm^{-1} are the most sensitive to structural changes induced by lithium insertion indicating changes in long-range ordering and local symmetry, respectively.

III.3.3 Chemical Lithiation of Bulk Particles

In this work, we have focused on examining the structural progression upon chemical lithiation in the $x < 1$ regime for micrometer-sized V_2O_5 powder, hydrothermally grown V_2O_5 nanowires, and CVD-grown nanostructured arrays. Figure III.4 shows XRD patterns acquired for the three samples upon being subjected to chemical lithiation with a molar excess of *n*-butyllithium.

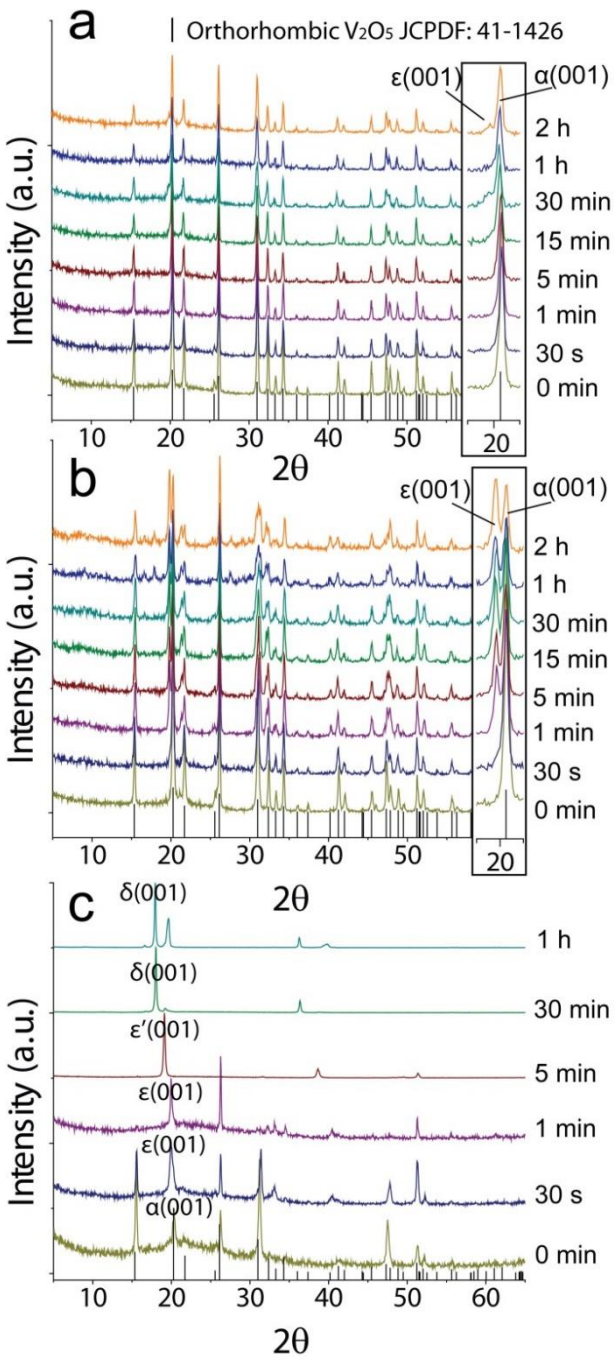

Figure III. 4 XRD patterns acquired for (a) bulk V_2O_5 powder, (b) hydrothermally grown V_2O_5 nanowires, and (c) CVD-grown nanostructured arrays as a function of increasing chemical lithiation time. The reflections of the orthorhombic phase of V_2O_5 (JCPDS# 41-1426) are also plotted for comparison. The insets to (a) and (b) show a magnified view of the (001) reflections of the α and ε phases. Reprinted from 48.

The bulk powder can be indexed to the orthorhombic *shcherbinaite* phase of V_2O_5 (Joint Committee on Powder Diffraction Standards (JCPDS) #41-1426). For lithiation times from 30 s to 2 h, there is little change in the powder diffraction pattern for the bulk powder sample suggesting that the structure is not altered beyond the α phase ($x < 0.1$). As more lithium ions insert into the α-phase, a slight shift of the (001) reflection is evidenced from $2\theta = 20.32°$ to $2\theta = 20.20°$ suggesting a slight increase (by 0.02Å) of the *c*-parameter as the inserted lithium ions disrupt the weak electrostatic interactions between the adjacent layers. After chemical lithiation for 30 min, a new reflection begins to emerge at $2\theta = 19.8°$ that corresponds to the (001) reflection of the ε-phase of $Li_{0.4}V_2O_5$ (inset to Fig. III.4a).[88] This shoulder continues to grow in intensity for the remainder of the chemical lithiation process. However, the sample clearly remains overwhelmingly composed of the α-phase (perhaps with surface nucleation of ε-phase); indicating that the lithium content in the bulk of the sample does not surpass $x = 0.1$.

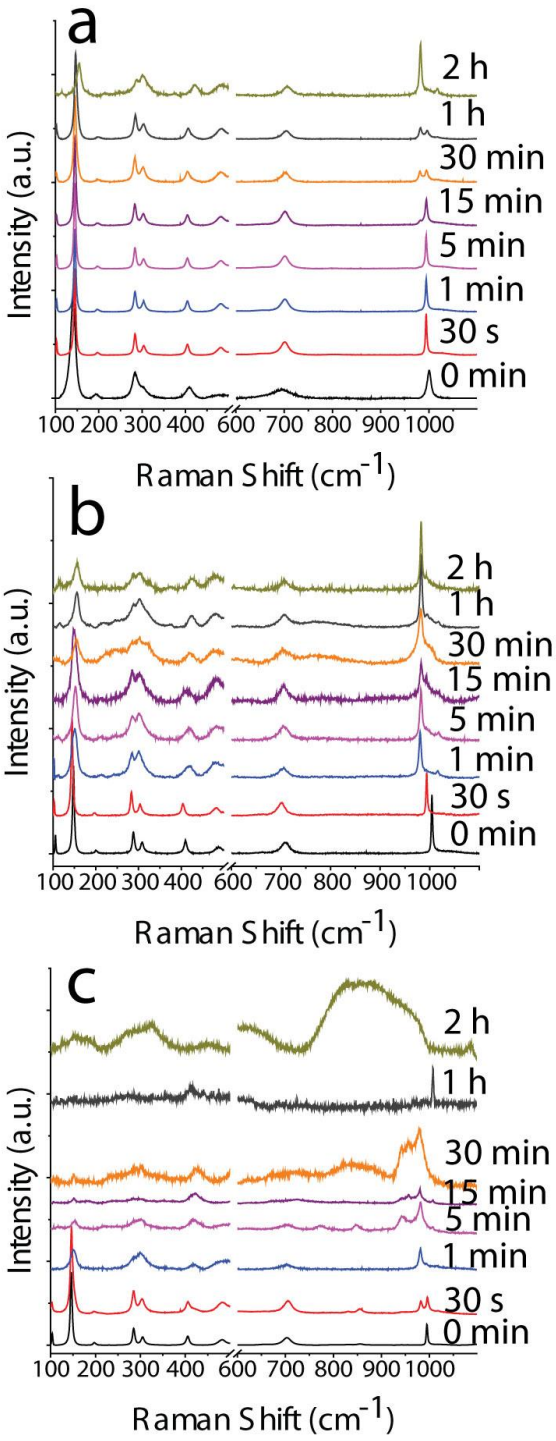

Figure III. 5 Raman spectra acquired for (a) bulk V_2O_5 powder, (b) hydrothermally grown V_2O_5 nanowires, and (c) CVD-grown nanostructured V_2O_5 arrays as a function of increasing chemical lithiation time. Reprinted from 48.

The Raman spectra shown in Figure III.5a shows more pronounced changes indicative of stabilization of the α phase. After 30 s of lithiation, the highest intensity [VO_5-VO_5] external mode is shifted from its position at 140.8 cm^{-1} for the unlithiated phase to 143.9 cm^{-1}. With increasing extent of Li-insertion, this Raman band further hardens to 146.0 cm^{-1}. A pronounced decrease in intensity (relative to the vanadyl stretch) proceeds concomitantly with hardening of this mode. This decrease in intensity attests to the loss of long-range order along the planes of VO_5 polyhedra.[75,89,169,171,172,178] The hardening of this mode indicates increased interaction between adjacent square pyramidal VO_5 units, which is further reflected by a decrease of the *a* parameter (from 11.51Å for the α phase to 11.38Å for the ε-phase).[75,89,169,171,172,178] After 2 h of chemical lithiation, the [VO_5-VO_5] external mode is shifted to 153.9 cm^{-1}, broadened to a FWHM of 5.6 cm^{-1}, and significantly diminished in intensity (Fig. III.5a). These changes suggest a continual loss of in-plane ordering as the layers begin to pucker, bringing the square pyramidal units in closer proximity. The broadening of this mode could be due to relaxation of selection rules owing to the breaking of symmetry as well as inhomogeneities in the extent of remnant order across the micrometer-sized grains of the sample as the α (and subsequently ε) domains are nucleated and grow from the edges exposed to the electrolyte.

As for the prominent high-frequency vanadyl stretch, only 30 s chemical lithiation induces a shift of this peak from 1000 to 993 cm^{-1}, with this softening consistent with an increase in the V—O bond length induced upon formation of the α-phase (Fig. III.5a). The first indication of emergence of the ε-phase occurs with the appearance of a shoulder to the vanadyl stretch at 980 cm^{-1} after lithiation for 15 min. This shoulder rapidly grows into

its own distinct spectral feature upon chemical lithiation for 30 min, and finally represents the most significant mode in the vanadyl stretching region after lithiation for 2 h. The V—O1 distance has been reported to increase from 1.58Å in the α-phase to 1.60Å in the ε-phase, which is consistent with the observed red-shift of the vanadyl stretch. Scanlon et al. have moreover predicted that the O1 atom vacancy represents the most stable defect and thus likely to be created during reduction.[77] Throughout this series, there is no significant change in the peak positions of the internal modes at 404 and 524 cm^{-1} until the 2 h time period as the ε-phase begins to emerge. At this point, these two modes have been noted to be shifted to 420 and 534 cm^{-1}, respectively. This shift can also be attributed to the decrease of the *a* parameter as the puckering draws the edge-sharing square pyramids closer together.

After 30 min of chemical lithiation, an additional low-intensity feature appears in the vanadyl region at 1017 cm^{-1}, possibly indicating the appearance of an additional phase. The δ phase appears to be the most likely candidate since it has a prominent stretching mode at ca. 1008 cm^{-1}.[89] The hardening of this mode with increasing lithiation (as compared to the V—O stretch observed for the ε-phase) has been ascribed to the strong puckering of layers noted in the δ-phase (Fig. III.1c), which brings the O1 atoms capping adjacent VO_5 square pyramids in relatively close proximity (O1—O1 separations of 2.77 Å for the δ-phase as compared to 3.00Å for α and ε phases). The steric repulsions induced between adjacent O1 atoms is thought to harden this phonon again in the δ-phase.[75] The intensity of the δ-phase Raman mode remains rather low even after 2 h of lithiation, suggesting that his phase is confined to the surface of the V_2O_5 grains.

The apparent discrepancy in the relative concentrations of the lithiated phases detected by XRD (primarily α with emergence of a minor ε-phase contribution after 2 h) and Raman spectroscopy (emergence of ε-phase after just 15 min and its eventual ascendancy at 2 h with detection of trace amounts of δ) is worthy of comment. The relatively higher concentration of the ε-phase noted in the Raman measurements could be due to the relatively greater sensitivity of this technique to changes in symmetry as a result of puckering (the powder diffraction pattern is less capable of distinguishing between α and incipient (lower end of Li concentration range) ε phases. As a second more likely possibility, the probing depth for Raman spectroscopy is considerably shallower (50—100 nm) and surface species may have a disproportionately greater contribution. In other words, the surface layers of the micron-sized grains are likely to have transformed to the ε-phase beginning at 15 min and progressing to almost full conversion in 2 h. Such a discrepancy between XRD and Raman results has also been previously observed while investigating the structural modifications of a composite cathode using these two analytical techniques and has been similarly attributed to diffusion gradients within V_2O_5 grains.[89]

III.3.4 Chemical Lithiation of Hydrothermally Prepared Nanowires

Next, we turn our attention to chemical lithiation of the hydrothermally prepared nanowires depicted in Figure III.3a. The nanowires have been lithiated in much the same way as the bulk powder samples using an equivalent molar excess of *n*-butyllithium. Figure III.4b indicates the XRD patterns and Figure III.5b indicates the Raman spectra acquired for these nanowires with increasing insertion of Li-ions over a period of 2 h.

The XRD pattern for the as-prepared nanowires in Figure III.5b corroborates that the nanowires crystallize in the orthorhombic *shcherbinaite* phase of V_2O_5 (JCPDS #41-1426). A much more accelerated structural progression is observed for these nanowires as compared to their bulk counterpart upon lithiation with *n*-butyllithium. After just 30 s of lithiation, the (001) reflection of the ε-phase emerges as a shoulder to the (001) reflection of the α-phase indicating much faster uptake of lithium. This reflection becomes a well-resolved feature after just 1 min of chemical lithiation and then continues to grow in intensity for the remainder of the lithiation period, surpassing the (001) reflection of the α-phase at the 2 h mark. Notably, the (001) reflection for the α-phase is not discernibly shifted over the 2 h time period, suggesting that this feature is derived from regions of the nanowires that are less accessible to Li-ions. These regions are clearly diminished in spatial extent with increasing lithiation as indicated by the decrease of the relative intensity of the (001) reflection of the α-phase. Notably, Chan and co-workers have noted the presence of diffusion barriers between lithiated and unlithiated phases within individual V_2O_5 nanorods grown by chemical vapor transport.[71] There is a clear shift of the (001) reflection of the ε-phase from $2\theta = 19.88°$ (after 1 min) to $2\theta = 19.80°$ (after 2 h) indicating an increase of the *c* parameter of the ε-phase from 4.466 Å to 4.484Å. Based on the unit cell parameters, the initially lithiated phase has $x < 0.33$, whereas x is ca. 0.4 for the ε-phase after 2 h of lithiation.[88,171] These observations thus suggest a picture wherein lithiation of specific favored regions (most likely at ends and surfaces of the nanowires) results in rapid nucleation of the ε-phase. Subsequent chemical lithiation results both in growth of the incipient ε-phase nuclei at the expense of the α-phase (as Li-ions diffuse

inwards from the surface) as well as increasing incorporation of Li-ions within the ε-phase to form $Li_xV_2O_5$ solid-solutions with higher *x* values. The free energy for incorporation of additional Li-ions in the ε-phase appears to be comparable to the energy required to grow the ε-phase nuclei (by inwards diffusion of Li-ions) since these two processes proceed in parallel. Figure III.5b also indicates that the (200) reflection at $2\theta = 15.4°$ in the unlithiated phase is shifted to $2\theta = 15.5°$ after 2 h of chemical lithiation. This shift indicates the contraction of the unit cell in the *a* direction as expected from a transition to the ε-phase.

The Raman spectra in Figure III.5b further corroborate a much hastened structural progression. The vanadyl stretch occurs at 1003 cm^{-1} for the as-prepared nanowires, which is somewhat higher than the 1000 cm^{-1} Raman shift noted for V_2O_5 powders. The increased stiffness of the V—O1 bonds may be a result of compressive strain induced within the nanowires during thermal oxidation of V_3O_7 to V_2O_5. After 30 s of chemical lithiation, the vanadyl stretch is shifted to 993 cm^{-1}, which suggests elongation of the V—O1 bond as a result of lithiation to the α-phase. The lithiation process likely relieves the compressive strain within the nanowires. Remarkably, after only 1 min of lithiation, the vanadyl stretch is shifted to 980 cm^{-1} suggesting transformation to the ε-phase. These results indicate rapid and complete transformation of V_2O_5 within the probing depth of the 514.5 nm laser to the ε-phase. As with the bulk, the formation of the ε-phase is also suggested by an abrupt shift of the [VO_5-VO_5] external modes from 143 cm^{-1} in the α-phase to 149 cm^{-1} suggestive of increased in-plane rigidity that accompanies shrinking of the *a* parameter due to puckering of the layers. This band is further successively broadened and decreased in intensity with increasing extent of lithiation. The internal modes at 404 and 524 cm^{-1} are

also shifted to 424 and 542 cm^{-1}, respectively, indicating greater puckering of the layers.[75,169,172] The 288 and 308 cm^{-1} modes also broaden and their intensities become similar as they begin to coalesce into a single band suggesting a modification of the rocking motion due to the presence of Li-ions in the cubooctahedral cavities, as is characteristic of the ε-phase with *x* in proximity of 0.4—0.5.[172]

After lithiation for 1 min, we note the emergence of a shoulder at 1017 cm^{-1} as also noted for the bulk in Fig. III. 5a. This feature grows in intensity and some spectral weight is observed as a high-frequency tail to the vanadyl stretch suggesting again surface nucleation of the δ-phase. Notably, we do not observe any bands characteristic of the Li-rich ε' phase of V_2O_5 suggesting that $x < 0.5$ in these materials.[89]

Taken together the XRD and Raman data indicate a much more rapid structural progression wherein the ε-phase is nucleated <1 min after immersion of the nanowires in the *n*-butyllithium solution. The initial nucleation of the ε-phase likely happens at the surfaces (based on the differences in surface-sensitive Raman and ensemble-averaged X-ray diffraction), following which the ε-phase nuclei expand inwards by the diffusion of Li-ions. Concurrent with growth in the spatial extent of the ε-phase, additional Li-ions are further accommodated within this phase with the stoichiometry *x* of $Li_xV_2O_5$ changing from ca. 0.3 to 0.4. A stark contrast between the bulk and nanowire samples is seen in the Raman measurements. For the former samples, the ε-phase is dominant only after 2 h, whereas for the latter, full conversion to the ε-phase is noted after 1 min.

III.3.5 Chemical Lithiation of CVD-Grown Nanostructures

The CVD-grown nanostructures shown in Figure III.3b have dimensions further reduced from that of the hydrothermally grown nanowires. The chemical lithiation of these structures shows the profound impact of the reduction in Li-ion diffusion path length on the structural progression and kinetics of lithium-ion uptake.

Figure III.4c shows XRD patterns and Figure III.5c shows Raman spectra acquired for the CVD grown nanostructures during the lithiation process. The XRD pattern is characterized by strong intensities of the (00*l*) reflections given the highly oriented nature of these nanoplatelets on the Si/SiO_2 substrate and their preferential growth direction.[61,182] Nevertheless, the shifts of the peak positions provide insight into structural changes induced by chemical lithiation. After 30 s of lithiation, there is a clear shift of the (001) reflection from $2\theta = 20.35°$ for the unlithiated samples to $2\theta = 20.0°$ indicating formation of α-phase containing about the maximum lithium content for the pure phase (*x* of ca. 0.1 in $Li_xV_2O_5$). After lithiation for only 5 min, the (001) reflection is shifted to $2\theta = 19.1°$, which corresponds to a *c*-parameter of 4.65Å. This value suggests that the Li-rich ε'-phase is almost maximally lithiated with *x* of ca. 0.9 adjacent to phase boundary with the δ-phase. Such a lattice parameter has been previously been observed upon solid-solution formation for V_2O_5 thin film electrodes wherein Li-ions are accommodated in the metastable ε'-phase instead of inducing a phase transition to the δ-phase (Fig. III.1c).[75] After lithiation for 30 min, the reflection appears at $2\theta = 18°$ suggesting stabilization of the δ phase with *x* of ca. 1. A slight shift to $2\theta = 17.95°$ with retention of the δ phase is observed upon lithiation for 1 h.

Given the small volume of the active cathode material on the Si/SiO_2 substrates and their highly preferential growth (which decreases the number of useful reflections), the indexing of the reflections is somewhat ambiguous. In contrast, Raman spectroscopy provides more insight into the structural evolution of each phase. The vanadyl stretch for the V_2O_5 nanostructured arrays appears at 994 cm^{-1}. After 30 s of lithiation, the vanadyl stretch is observed to be split into two modes at 982 and 996 cm^{-1} that are indicative of the presence of both α and ε-phases (Fig. III.5c). The external [VO_5-VO_5] translational modes are further shifted from 145 to 150 cm^{-1} and indicate some broadening. After 1 min, the Raman spectra indicate complete conversion to the ε phase with the vanadyl stretch at 981 cm^{-1} being the sole mode in the high-frequency region. Furthermore, there is a clear shift of the [VO_5-VO_5] mode to 151 cm^{-1} and a large decrease in intensity of this peak. The 282 and 302 cm^{-1} bands further broaden and begin to coalesce as observed for x contents in ε-$Li_xV_2O_5$ approaching ca. 0.4—0.5.[89] These spectral changes suggest stabilization of the ε-phase with some loss of long-range order and increased puckering and separation of the layers.

After 5 min of chemical lithiation, the [VO_5-VO_5] mode is greatly diminished and is shifted to 155 cm^{-1}. The mid-frequency internal modes also become less defined. Interestingly, the vanadyl region becomes substantially more complex with the appearance of two additional features. The 981 cm^{-1} mode has the highest intensity and a new band appears at 941 cm^{-1} along with a weak feature at 1006 cm^{-1}. These spectral features are characteristic of highly-lithiated ε'-phases.[75,89,169,171,172] At Li contents of $x > 0.53$ in $Li_xV_2O_5$, Li-ions that have been occupying alternating cubooctahedral crystallographic

sites need must situate any additional inserted Li-ions in adjacent sites.[88,171] The Li—Li distance thus shrinks dramatically from 7.2 to 3.6 Å. The additional vibrational modes reflect the coupling of the V_2O_5 phonons with the Li-ions as well as the greatly enhanced puckering that is induced within this structure due to the repulsion between the Li ions (reflecting a competition between filled and unfilled cubooctahedral cavities) as well as localization of V^{4+} ions.[88] Indeed, the repulsive interactions between proximally located Li-ions has been demonstrated to induce extended disorder in the form of stacking faults that are not observed for the relatively Li-deficient ε-phase.[90] Katzke et al. have proposed the stabilization of randomly disordered orthorhombic and monoclinic layers stacked along the [001] direction.[90] The introduction of these monoclinic domains reduces the symmetry giving rise to additional Raman-active modes. The ε' structure has further been reported to be incommensurately modulated and undergoes a ferroelastic phase transition upon cooling.[91] At 15 min, these features are mostly retained with further loss of intensity for the low-frequency external modes suggesting increasing *x* values for ε'-$Li_xV_2O_5$. The 1006 cm^{-1} peak suggests the presence of the δ-phase on the surfaces as also noted in the preceding sections.

After 30 min of lithiation, the 1006 cm^{-1} mode is no longer observed and instead we note three prominent vanadyl stretching features at 980, 957, and 941 cm^{-1}, indicative of stabilization of the γ-phase[75,89,176] (Fig. III.1d). The presence of a broad peak between 800 and 900 cm^{-1} confirms this assignment. At 30 min, the [VO_5-VO_5] mode is barely discernible above the noise of the baseline suggesting extensive disorder. The emergence of multiple spectral features in the vanadyl region reflects the reduced symmetry of the γ-

phase (Fig. III.1d) wherein the ladders are no longer equivalent and thus there exist distinct sets of vanadium sites with two distinctive V—O bonds40 (V1—O1 and V2—O1).[4] The metastable δ-phase has been shown to undergo a transformation to the γ-phase under the influence of laser irradiation.[169] Such laser-induced transformation cannot be ruled out in this case especially given the observation of the δ phase by XRD. Indeed, with continuing lithiation for 1 h, and after further reduction of laser power, we are able to see a broad, weak, feature at 425 $cm^{-1,}$ as well as the emergence of a strong, well-defined, V—O1 spectral feature at 1008 cm^{-1}. The position of the vanadyl feature is diagnostic of the δ-phase. Its shift to higher frequency is attributed to the introduction of steric repulsions between vanadyl oxygens as the lattice becomes severely puckered,[75] and the O1—O1 interatomic distance shortens from 3.35 Å in the orthorhombic phase to 2.76 Å in the δ-phase. After 2 h, well-defined Raman modes are no longer observed suggesting extensive amorphization of highly lithiated structures.

Whereas Raman spectra indicate that the freestanding nanowires are primarily in the ε-phase after lithiation for 2 h, the CVD-grown nanostructured arrays show complete conversion to the ε'-phase (with $x > 0.53$) upon chemical lithiation for just 5 min, a laser induced transition from the an initially stabilized δ- to the γ-phase for 30 min of lithiation, and retention of this δ-phase upon lithiation for 1 h. Further lithiation for up to 2 h results in transformation to an unknown highly lithiated and apparently amorphized phase.

III.3.6 Comparison of Lithiation of Bulk Powder, Free Nanowires, and Nanostructured Arrays

The discussion above clearly indicates that the rate of structural progression follows the order: CVD-grown nanostructured arrays >> hydrothermally grown nanowires > bulk powder. The discrepancies between the structural assignments derived from the Raman and XRD data point to the Li-insertion reaction primarily being a surface phenomenon. Monophasic regions are observed in Raman spectra, whereas multiphase regions observed in XRD patterns suggesting that complete phase transformation at surfaces precedes lithiation of the sample cores. Figure III.6 illustrates the stark differences between the three samples analyzed here after reaction times of 1 min, 5 min, 30 min, and 2 h.

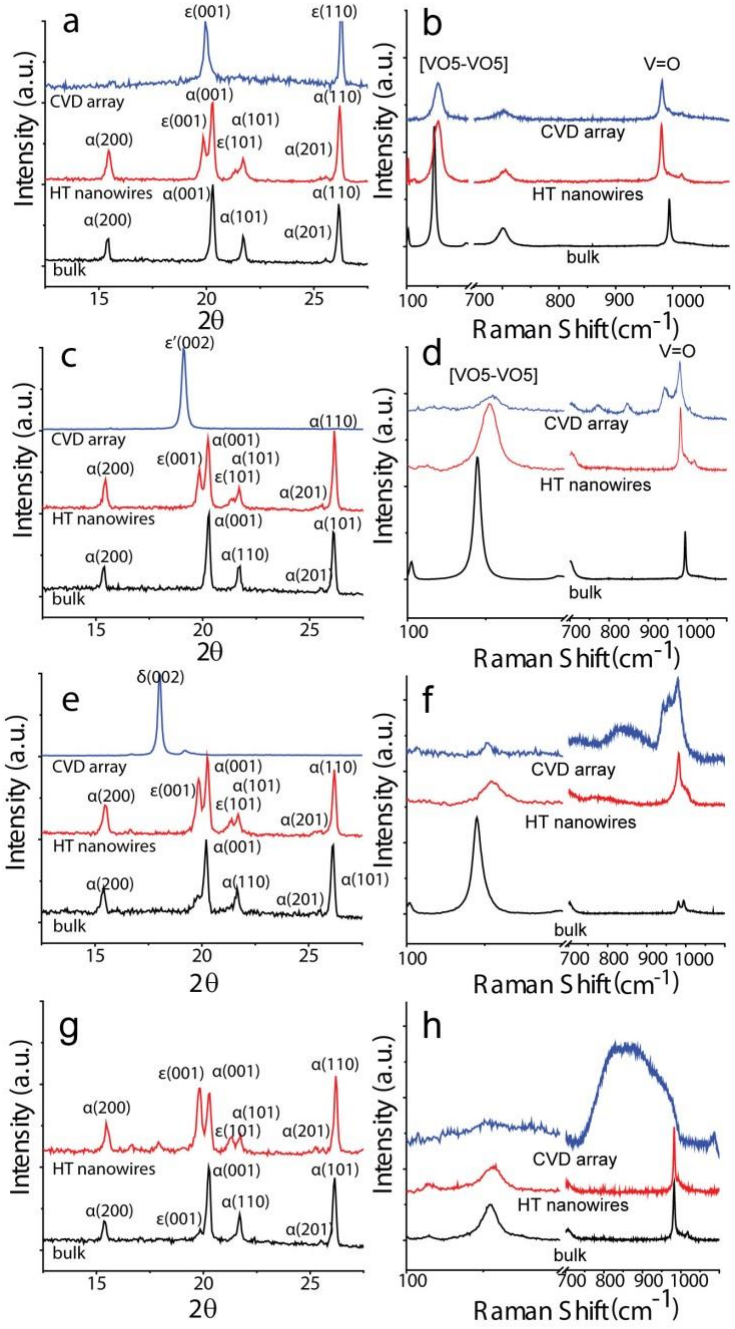

Figure III. 6 Comparisons of the three samples (micrometer-sized "bulk" powder, hydrothermally grown nanowires, and CVD-grown nanostructures) after chemical lithiation for different time periods. (a) XRD patterns and (b) Raman spectra acquired after 1 min of lithiation; (c) XRD patterns and (d) Raman spectra acquired after 5 min; (e) XRD patterns and (f) Raman spectra acquired after 30 min; and (g) XRD patterns and (h) Raman spectra acquired after 2 h of lithiation. Reprinted from 48.

After chemical lithiation for 1 min (Figs. III.6a and b), XRD shows the micrometer-sized bulk particles are completely in the α-phase, the hydrothermally grown nanowires are a mixture of α and ε-phases, whereas the nanostructured arrays are fully transformed to the ε-phase. The Raman spectra reflect the lithiation in the 50—100 nm regions at the surfaces of the samples and indicate that the bulk particles are in the α-phase, the hydrothermally grown nanowires are in the ε-phase, and the CVD-grown nanostructured arrays are also in the ε-phase. The primary contrast between the latter two systems appears to be the complete conversion to the ε-phase evidenced for the nanostructured arrays, whereas XRD results indicate that the cores of the hydrothermally grown nanowires are still in the α-phase.

After chemical lithiation for 5 min (Figs. III.6c and d), XRD shows that the bulk powders are still primarily in the α-phase, the hydrothermally grown nanowires are proceeding to transition from the α to the ε phase, and the nanostructured arrays are in the Li-rich ε'-phase with $x > 0.53$. Raman spectroscopy corroborates these distinctions with the bulk powder still in the α-phase, the hydrothermally grown nanowires in the ε-phase (with some surficial δ-species), and the CVD-grown nanostructured arrays indicating clear signatures of the Li-rich ε'-phase. At this time interval, the contrast in the Li-ion uptakes between the different structures is very clearly evident.

After chemical lithiation for 30 min (Figs. III.6e and f), XRD indicates the initial emergence of the ε-phase in the bulk powder, which is still primarily in the α phase. In contrast, in the hydrothermally grown nanowires, the ε-rich phase has grown at the expense of the α-phase. The nanostructured arrays in turn appear to have transformed to

the δ-phase. Raman spectra indicate the presence of a mix of α and ε phases for the bulk, the ε-phase for the hydrothermally grown nanowires, and the γ-phase for the nanostructured arrays. It is worth noting that the γ-phase is thought to originate from laser-induced transformation of the δ-phase since upon continuing lithiation for 1 h, the δ-phase is unequivocally observed at reduced laser powers (Fig. III.5c).

After 2 h of chemical lithiation (Figs. III.6g and h), XRD indicates that the bulk powders are primarily in the α-phase with some evidence for likely surficial ε-phase. In contrast, XRD results indicate that the ε-phase dominates in the hydrothermally grown nanowires although the α phase is still present. The XRD pattern for the nanostructured arrays (not shown) indicates the absence of any reflections suggesting complete amorphization. Raman spectra for the bulk and the hydrothermally grown nanowires indicate stabilization of the ε-phase. This data suggest that a ca. 100 nm surficial region of the bulk has now transformed to the ε phase although the cores are still essentially unlithiated. In contrast, a much greater proportion of the nanowires are in the ε-phase due to their higher surface-to-volume ratio. Remarkably, Raman spectra for the nanostructured arrays further corroborate amorphization of the samples suggesting strongly accelerated uptake of Li-ions.

In light of these comparisons, the reduction in diffusion path lengths induced by scaling to nanometer-sized dimensions is observed to profoundly alter the kinetics of structural transitions induced upon lithiation. The bulk material, with average particle dimensions in the micron regime, is the slowest to uptake lithium. The free standing nanowires, with average diameters of 150-250 nm are lithiated much more quickly than

the bulk. Notably, even at these dimensions, differences between surficial and core lithiation are observed although they are clearly much less pronounced than in the bulk. The nanostructured arrays show dramatically accelerated kinetics of Li-ion insertion/extraction far outpacing the bulk and hydrothermally grown nanowires and with a relatively uniform core/surface lithiation profile. Remarkably, these materials appear to be amorphized upon 2 h of chemical lithiation.

III.3.7 Delithiation of V_2O_5 Bulk Powder, Hydrothermally Grown Nanowires, and CVD-grown Nanostructured Arrays

The delithiation and re-oxidation of all the chemically lithiated samples has been studied via Raman spectroscopy. The samples lithiated for different time periods (Fig. III.7) have all been delithiated for 2 h by immersion in liquid Br_2. For the micrometer-sized bulk powder, Figure III.7a indicates recovery of the α-phase after delithiation even for the 2 h lithiated sample that had transformed to the ε-phase (Fig. III.5a). Comparison to the unlithiated V_2O_5 starting material indicates that the vanadyl peak is shifted to somewhat lower frequencies, 996 cm^{-1} as compared to 1000 cm-1 for the bulk sample. The [VO_5-VO_5] external mode is furthermore shifted to 145 cm^{-1} as compared to 141 cm^{-1} in the bulk. Since the samples lithiated for different amounts of time (with different extents of surficial lithiation) are all delithiated to the same extent, the differences from the unlithiated starting material likely originate from remnant incorporated lithium, suggesting stabilization of the α-phase upon re-oxidation of the sample. These results are analogous to recovery of the α (but not the unlithiated orthorhombic) phase observed recently in an *in situ* electrochemical lithiation study.[89] The downshift of the vanadyl

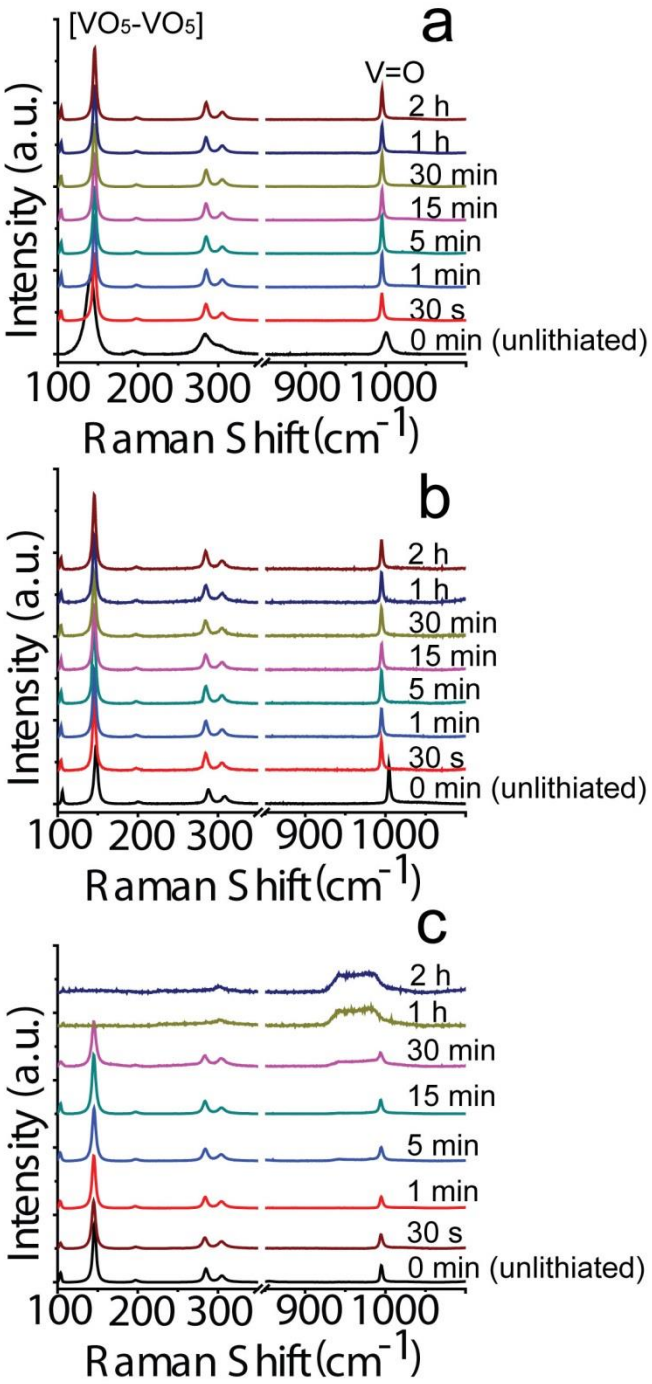

Figure III. 7 Raman spectra of V_2O_5 as (a) bulk powder; (b) hydrothermally grown nanowires; and (c) CVD-grown nanostructured arrays lithiated for varying extents of time noted alongside the spectra after then being subjected to chemical delithiation for 2 h with Br_2(l). Reprinted from 48.

stretching mode indicates an extended V—O1 bond and could also imply the presence of oxygen vacancies.[75] The relatively higher frequency of the [VO_5—VO_5] external modes suggests a somewhat reduced a parameter.

Analogously, the hydrothermally lithiated nanowires also appear to revert to the α-phase (Fig. III.7b) even for the samples chemically lithiated for 2 h (thought to form ε-$Li_xV_2O_5$ with *x* of ca. 0.4). The CVD nanostructures, however, show that for samples lithiated for up to 30 min there is relatively complete reversion to the unlithiated structure. Notably, the [VO_5—VO_5] external modes for the delithiated samples occur at 145 cm^{-1}, unshifted from the 145 cm^{-1} bands observed for the unlithiated samples. For the CVD-grown nanostructured V_2O_5 arrays, Figure III.7c indicates that the Raman bands revert to those of the orthorhombic unlithiated phase for samples lithiated for up to 30 min (stabilized in the δ phase). Unlike for delithiation of the bulk phase, no evidence for reversion halting at the α-phase is observed in these samples. Also in contrast to the bulk and hydrothermally grown nanowires, the CVD-nanostructured array samples lithiated for longer time periods do not revert to the orthorhombic or α-phase upon delithiation. Broad Raman features do develop in the 930 to 1000 cm^{-1} region, likely arising from V—O stretching modes. A weak band further appears at 301 cm^{-1} (Fig III.7c). Chemical lithiation of the V_2O_5 nanostructured arrays for 2 h is thus observed to induce irreversible amorphization but complete delithiation can be achieved for samples transformed to the δ phase.

III.4 Conclusion

We have investigated the structural transitions induced within bulk V_2O_5, hydrothermally grown V_2O_5 nanowires (diameters on the order of 150—250 nm), and CVD-grown V_2O_5 nanowire arrays (platelet dimensions of ca. 50 nm) upon chemical lithiation with a molar excess of n-butyllithium. Scaling V_2O_5 to nanometer-sized dimensions is seen to profoundly alter the kinetics of Li-ion uptake and the rates at which phase transitions are induced within this structure. Based on XRD and Raman spectroscopy measurements, gradients in chemical composition are established in the bulk and hydrothermally grown nanowires samples with lithiation and ensuing phase transitions initiated at the surfaces and propagating towards the interior. Stark differences in conversion of the core are noted for the bulk and the hydrothermally grown nanowires. For instance, at 2 h, the surface of the bulk powder is primarily in the ε-phase (Fig. III.5a), whereas the vast majority of the sample is unlithiated or in the α-phase (Fig. III.4a). In contrast, the surfaces of the nanowires are primarily in the ε-phase (Fig. III.5b) and the ε-phase also dominates the diffraction pattern for the hydrothermally grown nanowires after lithiation for 2 h (Fig. III.4b). The CVD-grown nanostructured arrays behave very differently with a much accelerated sequence of phase transitions and with the extent of lithiation at the surface and within the bulk in much better concord.

Raman spectroscopy has been noted to serve as an excellent probe of local structure within the lithiated materials and allows for development of a detailed picture of the phase progression.[75] Based on the Raman spectra shown in Figure III.5, the bulk sample is rapidly lithiated to the α phase (within 30 s at least at the surfaces of the grains).

The nucleation of the ε-phase is initiated after 15 min and this phase dominates after 2 h. In contrast, for the hydrothermally grown nanowires, the α-phase is again stabilized within 30 s but the ε-phase gains primacy after just 1 min of chemical lithiation. The ε-phase rapidly grows in spatial extent with continuing lithiation and also accommodates additional Li-ions up to *x* of ca. 0.4. A much more hastened phase progression is seen for the CVD-grown nanostructured arrays. The ε-phase is nucleated within just 30 s and is the dominant phase after 1 min of chemical lithiation. Lithiation for 5 min induces stabilization of the ε'-phase with $x > 0.53$, which then transforms to the δ-phase with $x >$ ca. 0.9 after 30 min of lithiation. Continuing lithiation for 2 h induces substantial amorphization of the nanoplatelets.

Stark differences are also observed in delithiation of the different systems examined here. The hydrothermally grown nanowires and the bulk powders revert back to the α-phase (but not the unlithiated orthorhombic phase) regardless of the crystal structure reached after 2 h of lithiation. In contrast, the nanostructured V_2O_5 arrays can be completely delithiated back to the orthorhombic phase for samples that have been lithiated to the δ-phase after 30 min of reaction with *n*-butyllithium. However, further lithiation induces irreversible amorphization of these nanostructures.

In conclusion, scaling to finite size substantially accelerates the structural phase progressions of dimensionally confined materials upon discharge, likely as a result of the enhanced Li-ion insertion and diffusion gradients as well as the relatively facile accommodation of structural strains induced within the materials upon nucleation of a phase transition. Indeed, within the 1D nanowires and 2D thin nanoplatelets examined

here, the nucleated phase only needs to propagate in one- or two-dimensions, whereas a substantially more energetically prohibitive three-dimensional distortion in structure is required upon lithiation of bulk powders.[7128] The much accelerated kinetics of Li-ion uptake noted here portends substantial enhancements of powder density for nanostructured V_2O_5 electrodes. Future work will focus on examining inhomogeneous lithiation and the nature of diffusion barriers within individual V_2O_5 nanowires based on sub-difffraction-limit Raman imaging and examining finite size effects on the lithiation of vanadium oxide bronze phases such as β'-$Cu_xV_2O_5$. [183,184]

CHAPTER IV

VANADIUM K-EDGE X-RAY ABSORPTION SEPCTROSCOPY AS A PROBE OF HETEROGENEOUS LITHIATION OF V_2O_5: FIRST PRINCIPLES MODELING AND PRINCIPAL COMPONENT ANALYSIS*

IV.1 Introduction

The push towards sustainable power generation and the further electrification of society places ever increasing demands on batteries and other electrical energy storage systems. While high capacity anode materials such as Si and Sn/SnO_x have become available in recent years,[70,81] current batteries are greatly limited by the storage capacities and operational kinetics of cathode materials. The insertion of Li-ions within a cathode material during the discharging of a battery brings about a profound modification of both the geometric and electronic structure of the host in a manner that is still not entirely understood. In particular, the sequence of structural transitions and band filling is strongly rate dependent in several cathode materials such as $LiFePO_4$ with phase diagrams characterized by the appearance of metastable phases and unusual phase coexistence regimes.[41,53,185] Spatial and temporal heterogeneities during the insertion/extraction of Li-ions have been implicated as being amongst the primary causes for preventing the power and energy densities of Li-ion host materials from reaching their theoretical maximum

* Reprinted with permission from "Vanadium K-Edge X-Ray Absorption Spectroscopy as a Probe of the Heterogeneous Lithiation of V_2O_5: First-Principles Modeling and Principal Component Analysis.: Horrocks, G. A.; Braham, E. J.; Liang, Y.; De Jesus, L. R.; Jude, J.; Velázquez, J. M.; Prendergast, D.; Banerjee, S. *J. Phys. Chem. C* **2016**, *120*, 23922–23932. Copyright 2016 American Chemical Society.

values.[6,186,187] However, the characterization and mitigation of such heterogeneities remains a considerable challenge.

The difficulties in development of an optimal cathode material lie in the requirements of the material to accommodate a large number of guest Li-ions and facilitate efficient Li-ion diffusion while also enabling electronic conduction.[6,188,189] Scaling to nanometer-sized dimensions as well as employing surface coatings and conductive fillers have helped increase electrical conductivity,[73] but inhomogeneities are inevitable as a result of lithiation gradients and dynamic phase nucleation/growth phenomena. Recently, there has been great interest in the phase evolution induced during cation insertion or removal, and the influence of finite size and nanostructuring on the phase stabilities of intercalation materials.[53,185,190,191] Indeed, several studies indicate that there are multiple pathways through which the host lattice can accommodate cation insertion. For instance, non-equilibrium stabilization of a metastable solid-solution emerges as a viable alternative to nucleation and growth of the lithiated phase upon cation insertion in nanoscale $LiFePO_4$ at high rates.[190,192] Given the complexity and heterogeneity of intercalated phases, a mixture of ensemble and single-nanowire probes have been used to probe the dynamics of the phase evolution including X-ray and neutron scattering,[53,193] *in situ* electron microscopy,[194,195] and Raman as well as X-ray imaging techniques.[45,191,196] X-ray absorption spectroscopy involves the excitation of core level electrons and yields resonances that are sensitive to both the local geometric and electronic structure and can thus serve as an excellent element-specific probe of intercalation-induced structural perturbations and phase evolution in transition metal oxides.[58,67,78,197–199] The V K-edge,

which is dominated by dipole-allowed transitions of V 1s electrons to V 4p states can be used as a semi-quantitative probe of nominal valence, local site symmetry, and local structure upon charge or discharge for vanadium compounds. Indeed, a considerable body of information exists regarding the V K-, V L-, and O K-edges of the binary vanadium oxides;[60,61,98,99,200–204] of these compounds, V_2O_5 has long been known to serve as an excellent intercalation host owing to its layered structure and ready accessibility of multiple vanadium redox couples. In this study, well-defined single-crystalline nanowires of V_2O_5 are used as a model system to probe phase evolution upon Li-ion intercalation.

The thermodynamically stable α-phase of V_2O_5 crystallizes with an alternating up-up-down-down motif of distorted [VO_5] square pyramids linked in the *ab* plane by corner and edge sharing (Fig. IV.1, inset). The layers are bound by van der Waals' and electrostatic interactions along the *c* axis, which define a quasi-octahedral coordination environment for the V atoms upon taking into consideration a long V—O bond with the distant oxygen atom in the next layer.[6,75] Three types of oxygen atoms can be distinguished within the square pyramids as indicated in the inset to Figure IV.1: vanadyl (apical oxygens), bridging oxygen atoms that link two adjacent square pyramids, and chaining oxygen atoms that connect three [VO_5] square pyramids. The adoption of such a layered structure and the abundance of interstitial sites allows for the facile accommodation of guest cations. The phase evolution of the intercalated phase, $Li_xV_2O_5$, as a function of the stoichiometry *x* has been mapped in extensive detail.[3,5,6] Upon the initial insertion of Li-ions, the α-phase is stabilized, where the interlayer spacing is increased and the 2D sheets slightly pucker along the *a* direction (Fig. IV.1(a)). Beyond $x > 0.1$, the ε-phase is

nucleated, yielding a phase mixture (α+ε $Li_xV_2O_5$) up to $x \approx 0.35$ at which point phase-pure ε-$Li_xV_2O_5$ is stabilized.[6,88] Up to a stoichiometry of $x = 0.5$, the interlayer spacing continues to expand to accommodate additional Li-ions, whereas the 2D sheets are increasingly puckered to accommodate the distortion of the square pyramids to facilitate coordination of apical oxygens to the intercalated Li-ions wherein they define a cuboctahedral coordination environment.[167] At $x = 0.5$, the even filling of Li-ions is no longer possible, leading to the formation of an incommensurately filled ε′-phase.[167] Notably, this is not a distinct phase but reflects the increased occupancy of the interstitial sites. At a x value greater than 0.7, nucleation of the δ-phase is initiated, which is accompanied by sliding of alternating planes by half of a unit cell along the *b* direction.[162,163] The δ-phase has a relatively narrow range of phase stability and is phase pure between $0.9 \leq x \leq 1.0$.[6,75] Above $x = 1.0$, the up-up-down-down pattern of the square pyramids is partially inverted to an up-down-up-down motif and the γ-phase is stabilized with a distinctive 3D geometry. In this structure, Li-ions are situated within tetrahedral environments defined by the apical oxygens of the square pyramids and the bridging oxygens of the layer below.[6,75] At full capacity, orthorhombic V_2O_5 is able to accommodate up to three Li-ions per V_2O_5 unit, albeit with a substantial structural rearrangement to a pseudo-cubic ω-phase.[92] In recent work, we have used Raman spectroscopy and X-ray diffraction to examine the evolution of intercalation-induced phase transformations in V_2O_5 with different particle size distributions and have observed the presence of multiphase mixtures and pronounced lithiation gradients even within nanowires that are only ca. 200 nm in diameter.[48] However, such methods are limited to

probing long-range order (X-ray diffraction) or only qualitatively indicating the presence of multiple phases (Raman spectroscopy).[48] In contrast, scanning transmission X-ray microscopy (STXM) maps of charge density indicate pronounced compositional gradients and phase domains within individual nanowires upon Li-ion insertion.[45] The intercalation gradients and charge inhomogeneities are thought to originate from (i) staging phenomena wherein a Li-ion is preferentially inserted within a layer that is already partially lithiated instead of an unlithiated layer as well as (ii) the localization of electron density within small polarons wherein the added electron localizes on a low-lying V $3d_{xy}$ level that couples to a local structural distortion.[45] Such localized reduction implies the potential utility of a local structure tool such as element-specific V K-edge X-ray absorption spectroscopy for discerning relative concentrations of distinctive vanadium sites with increasing lithium concentration. Indeed, a distinctive pre-edge feature observed in V K-edge spectra is essentially local in character and originates from the broken octahedral symmetry (specifically, square pyramidal) of the vanadium centers in V_2O_5 (Fig. IV.1c);[98,99,202,205] this feature is retained even upon the loss of 3D structural coherence in V_2O_5 xerogels with an expanded interlayer spacing and is furthermore observed even in the molecular solid $VOPO_4 \cdot 2H_2O$.[201,202] The vanadyl bond is perturbed by lithium intercalation as the apical oxygen atoms define a coordination environment for the inserted Li-ions and thus its spectroscopic signature can serve as a probe of local symmetry and nominal valence.[48,75] While intercalation induced changes are less pronounced at the V K-edge as compared to V L- and O K-edges wherein polaronic features are predominant,

careful analysis of the pre-edge structure of V K-edge absorption features reveal a wealth of information regarding both local symmetry and the vanadium valence.[59,206,207]

In this work, we present a V K-edge X-ray absorption near edge structure (XANES) spectroscopy study of the chemical lithiation of V_2O_5 nanowires. The XANES features are analyzed with the help of the excited electron and core hole (XCH) approach that is based on occupancy constraint density functional theory calculations. The calculations show that the pre-edge feature can be mainly attributed to dipole-allowed transitions from V 1s to 4p states. Experimental spectra for these systems are deconvoluted and monitored using principal component analysis (PCA) with multivariate curve resolution (MCR). The latter approach has been shown to be a powerful tool for the deconvolution of spectral data into component curves representative of the relative concentration of the species contributing to complex experimental data, and yet has thus far not found extensive use in the examination of intercalation processes.[102,207] The MCR analysis allows for mapping of the evolution of the symmetry and oxidation state of vanadium sites in V_2O_5 nanowires during the initial stages of chemical lithiation. The data suggest the nucleation and growth of a highly lithiated phase at the expense of a low-lithiated phase without stabilization of a solid solution.

IV.2 Experimental

IV.2.1 Synthesis and Chemical Lithiation of V_2O_5 Nanowires

Orthorhombic V_2O_5 nanowires were synthesized by the hydrothermal reduction of bulk V_2O_5 to $V_3O_7{\cdot}H_2O$ nanowires, which are subsequently oxidized and dehydrated by annealing at 350°C in air to yield nanowires of V_2O_5.[48] Stoichiometric chemical lithiation

was performed by reaction of the V_2O_5 nanowires with a stoichiometric amount of *n*-butyllithium in 20 mL of toluene for 4 days under an argon atmosphere in a glovebox as per:

$$V_2O_5 + xC_4H_9Li \rightarrow Li_xV_2O_5 + \frac{x}{2}C_8H_{18}\ldots(1)$$

After lithiation, the toluene solution was decanted and the recovered powder was washed with copious amounts of hexanes, and left to dry under an Ar atmosphere.

IV.2.2 V K-edge XANES Measurements and Deconvolution

XANES measurements were performed at NIST beamline X23A2 of the National Synchrotron Light Source at Brookhaven National Laboratory. The powder samples were diluted with boron nitride and sealed with Kapton™ tape under an Ar atmosphere in a glove bag prior to the measurements. A Si(311) monochromater was used for the experiments, yielding a spectral resolution of ($\Delta E/E$) of 2×10^{-4}. The incident and transmitted flux were measured using ion chambers filled with nitrogen gas. Spectra were acquired in triplicate for each sample; pre- and post-edge normalized using ATHENA to achieve an edge jump of unity; and calibrated and aligned using a metallic vanadium foil sample.[208,209] For polarized XANES experiments, a four-element silicon drift detector was used to collect fluorescent emission signals.

The transmission mode spectra were collated into a single matrix and used in principal component analysis (PCA) and MCR. PCA and MCR were performed using Matlab v8.5.0.197613 (The Mathworks) and PLS Toolbox v8.0 (Eigenvector, Inc). PCA preprocessing included normalization and mean centering. PCA results were used to select the number of relevant components for MCR. MCR was performed with normalization

preprocessing and non-negativity constraints. Three component curves were generated as per the results of PCA analysis. Scores are representative of the ratio of each of the three component curves in the description of the experimental data. Scores shown represent the average score of three replicates; error bars represent the first standard deviation from this analysis.

IV.2.3 STXM Measurements of Individual Nanowires

STXM measurements were collected at the spectromicroscopy beamline 10ID-1 of the Canadian Light Source, Saskatoon, SK. Right circularly polarized X-rays were used in the experiments focused by a 25-nm Fresnel lens zone plate to obtain spatial resolution better than 30 nm. The incident photon flux (I_o) count rate was adjusted to a value <20MHz and optimized to ca. 17 MHz as measured at 560 eV by the STXM detector within a hole located close to the sample of interest. The flux rate was altered by adjusting the exit slits to 17/16 mm (dispersive/non-dispersive). A 500 line mm^{-1} plane grating monochromator was used for the collection of V L- and O K-edge stacks from 508 to 560 eV with energy steps of 0.2 eV in the region-of-interest and 1 eV in the continuum region beyond the specific elemental edges with a dwell time of 1 ms at each section. The nanowire was raster scanned by the X-ray beam with transmitted beam intensities measured at the detector. All STXM data were analyzed and processed using aXis2000 software (http://unicorn.mcmaster.ca/aXis2000.html). STXM maps are derived based on singular value decomposition of the image stack in aXis2000 and by using as a reference the region of interest (ROI) spectra identified within different regions of the same image sequence.

IV.2.4 Electronic Structure Calculations and Analysis of XANES Data

The ground-state electronic structure calculations were performed within the framework of density functional theory (DFT),[210,211] using the Vienna *ab initio* Simulation Package (VASP).[212] The electron-electron interactions were modeled by the Perdew−Burke−Ernzerhof (PBE) formulation of the generalized-gradient approximation (GGA) of the exchange-correlation functional.[213,214] To account for the strong Coulomb interaction at the V sites, an on-site Hubbard U potential of 3.0 eV was included in the total-energy calculation and a 500 eV energy cutoff was used to truncate the plane-wave basis set.[215–217] All the structures investigated in this work were relaxed until each Cartesian component of the forces was less than 0.01 eV/Å.

The XANES simulations were performed using the PWscf code in the Quantum ESPRESSO package with the Shirley optimal basis set for efficient Brillouin zone sampling. The XCH approach was adopted to generate the XANES spectra wherein an electron was removed from the inner shell of the excited atom in a supercell to account for the excited state core—hole interactions. The core-level is not explicitly included in the calculation but incorporated in a modified V pseudopotential that is generated with one less electron on the 1s orbital. Consequently, the occupied part of the system has one additional excited electron and the entire electronic system is relaxed to its ground state within DFT. A 1×3×2 supercell was used for the calculations and was extrapolated from a unit cell of V_2O_5 with a = 11.503 Å; b = 3.557 Å; and c = 4.369 Å. The supercell dimensions are large enough to decouple spurious interactions between core—hole images. A broadening of 1.2 eV was applied to reproduce broadening that arises in

experimental results and the inevitable disorder in the alignment of the nanowires. Based on past studies an order parameter (dichroic ratio) of -0.425 was determined (where a value of -1 represents a perfectly aligned sample). As a result of the imperfect alignment of the nanowires, the spectral features are somewhat broadened.

IV.3 Results and Discussion

IV.3.1 Vanadium K-edge XANES Spectroscopy of $Li_xV_2O_5$

According to the dipole selection rules, V K-edge XANES spectra correspond to the excitation of V 1s core-level electrons to 4p states. In general, the lineshape and peak positions of transition metal K-edge spectra are quite sensitive to the oxidation state of metal ions given the broad energy dispersion of p final states.[100,200] Figure IV.1Ai and 1Aiii depict angle-resolved (at 20° and 90° incidence of the X-ray beam) V K-edge spectra acquired for oriented arrays of V_2O_5 nanowires grown on Si substrates.[61,182] Spectra collected for randomly oriented V_2O_5 nanowires in transmission mode are displayed in Figure IV.1Bi. In each case, the spectra are characterized by three broad features labeled *a*—*c*. A prominent pre-edge feature (labeled *a*) centered at ca. 5470.2 eV is observed before the ionization threshold (the white line absorption appears at ca. 5480 eV); the intensity and peak position of this feature depend sensitively on the local asymmetry and

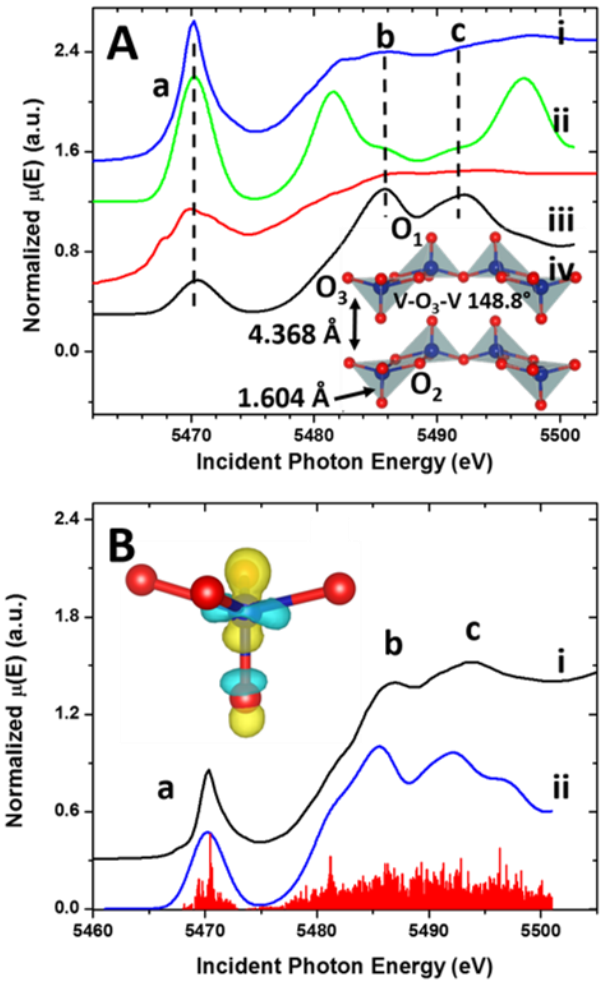

Figure IV. 1 (A) Comparison of experimental and calculated XANES spectra of oriented array of V_2O_5 nanowires acquired at (i) an incident photon angle of 90° relative to substrate and (iii) incident photon angle of 20° relative to substrate. Calculated spectra for pristine V_2O_5 obtained using the XCH-XAS method for incident photon angles of (ii) 90° and (iv) 20° relative to the V_2O_5 layers are depicted immediately below the experimental spectra to enable comparison. The inset depicts the crystal structure of V_2O_5 with vanadyl (O_1), triply coordinated chaining oxygen (O_2), and doubly coordinated bridging oxygen (O_3). Red spheres depict oxygen atoms and blue spheres depict vanadium atoms. The V=O bond length, interlayer spacing, and angle of puckering (V-O3-V) of the layers is indicated for this structure. (B) XANES spectra of (i) free powder of V_2O_5 nanowires acquired in transmission mode, (ii) calculated spectrum for pristine V_2O_5 obtained at 54.7° angle of incidence of the photon beam. The red fill under (ii) represents the contribution to the absorption intensity from the states that arise from V ($3d$ e_g + $4p$) + O $2p_z$ mixing. The inset depicts the isosurface plot for the final state that is the primary contributor to the pre-edge resonance. All calculated spectra reflect a Lorentzian broadening of 1.2 eV. Reprinted from 47.

oxidation state of vanadium atoms, as has been extensively documented in the literature.[59,98,200] In general, there is a consensus that this absorption is derived from transitions from V 1s to hybrid V 4p—3d states that become accessible due to the deviation from octahedral symmetry and covalency.[59,98–100] As suggested by the inset to Figure IV.1A, the [VO_5] square pyramids of V_2O_5 are strongly distorted with a short apical bond and relatively longer bonds to the four oxygen atoms at the base of the pyramid, resulting in a lowering of the site symmetry to C_s; this broken symmetry allows for mixing of V 3d—4p states. Furthermore, the hybridization of V 3d with O 2p orbitals yields unoccupied states with considerable *ungerade* character that become symmetry-allowed in the XANES experiment. It is worth noting that the bottom of the conduction band in V_2O_5 comprises V 3d states split by crystal field splitting into higher-lying e_g ($3d_{x2-y2}$ and $3d_{z2}$) and lower lying t_{2g} ($3d_{xz}$, $3d_{yz}$, $3d_{xy}$) states.[61,79,218] The $3d_{xy}$ state is further split-off from the t_{2g} set and forms the lowest lying conduction band level due to the lowering of symmetry. As shown by previous time-dependent DFT calculations,[99] V K-edge XANES spectra do not directly map the V 4p projected density of states but instead are reflective of the extent of hybridization of the 4p states with V 3d states.

The spectrum for pristine V_2O_5 as calculated from the XCH approach is shown in Figure IV.1Bii. The calculated spectra projected along the appropriate vectors are shown alongside the experimental spectra in Figure IV.1Aii and IV.1Aiv. The calculated spectrum in Figure IV.1Bii has been angle averaged to match experimental broadening arising from measuring a randomly oriented dispersion of nanowires. The calculation clearly reproduces the pre-edge feature as observed in the XAS measurement. More

importantly, the XCH calculation allows for analysis of the XAS excited states based on examination of the wavefunction of the supercell configuration. The red vertical bars at the bottom of Figure IV.1B plot the oscillator strengths of individual excited states, which have been aligned with the simulated spectrum. Selecting the individual excited state with the largest oscillator strength, it is then possible to visualize the associated partial charge density, as shown in the inset to Figure IV.1B. This excited state clearly features V $3d_z^2$ states localized at the excited V site; however, it is also evident that its charge distribution is asymmetric with respect to the V_2O_5 plane. Consistent with previous studies, the primary origin of pre-edge peak is the excitation of V 1s core level electrons to V 4p states mixed with V 3d e_g ($3d_{x2-y2}$ and $3d_{z2}$) character and hybridized with O $2p_z$ states.[98,204] The isosurface for the excited V atom plotted in the inset of Figure IV.1B allows for visualization of the electron density distribution of the final state, which is more strongly weighted above the plane of the inverted square pyramid. This asymmetry of electron density emphasizes the importance of the strong apical vanadyl bond, which has hybridized O $2p_z$ and V $3d_{z2}$ states (as compared to an unhybridized V $3d_{z2}$ state). Indeed, this absorption is strongly enhanced at normal incidence of the X-ray beam when the electric field vector of the incident X-rays is parallel to the V=O bond. It is clear from the directional hybridization along the V=O bond that the primary absorption has a dipolar and not a quadrupolar origin. At glancing incidence of the X-ray beam, two shoulders at 5467.7 and 5472.6 eV become discernible in the V K-edge XANES spectra (Fig. IV.1A); the lower energy shoulder includes contributions from V $3d_{xy}$ and V $3d_{xz}$ states that are symmetry matched for admixing with the V $4p_y$ component.[99] Weak quadrupolar V 1s→

3d transitions also contribute to the spectral intensity, particularly in the glancing incidence spectrum where the contribution from the dipolar vanadyl component is relatively lower. Of the relatively weak quadrupolar component, transitions to V $3d_{xy}$ and $3d_{x2-y2}$ states are the primary contributors to the spectral intensity.[98]

The white line absorption appears at ca. 5480 eV for V_2O_5.[98,219] The absorption edge arises due to dipole allowed $1s \rightarrow 4p$ transitions, and is sensitive to the vanadium oxidation state, generally adhering to Kunzl's law.[58,59] Beyond the edge jump, broad features are discernible at 5487 and 5494 eV and are labeled *b* and *c*, respectively.[98,219] These features are not as readily reproduced in the single-particle excitation or excitonic approaches available from density functional theory. Based on real-space multiple scattering calculations, more distant shells beyond nearest neighbor interactions, and not just electronic transitions to specific conduction band states, are required to model these

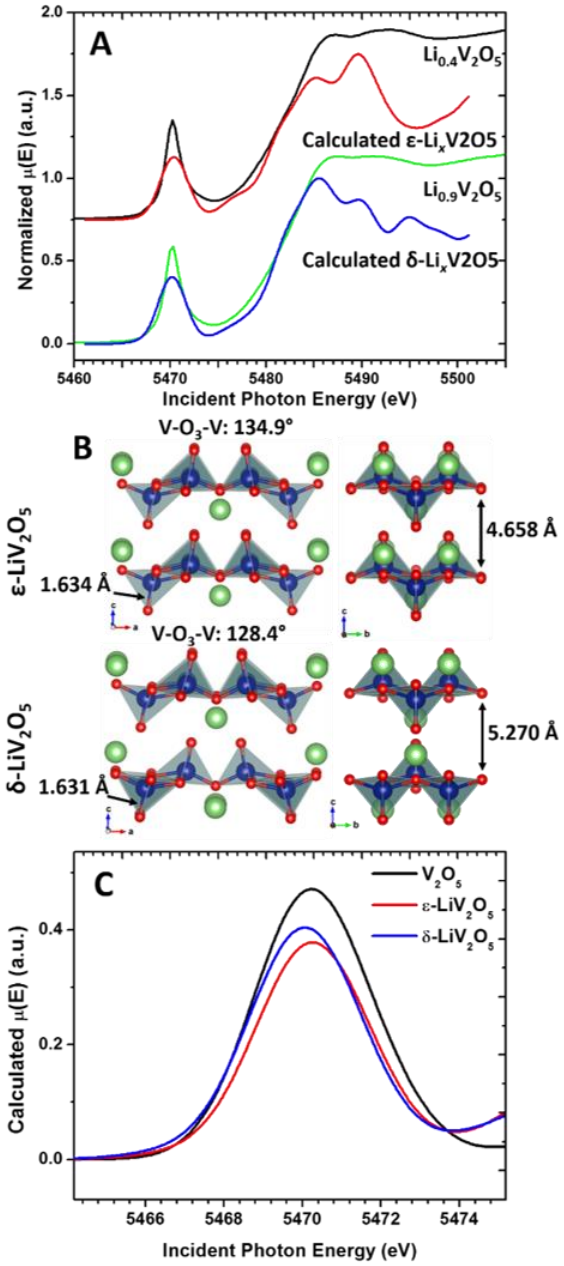

Figure IV. 2 (A) Comparison of $Li_xV_2O_5$ nanowires with nominal *x* values of 0.4 and 0.9 with XCH-XAS calculated spectra; the spectra reflect a Lorentzian broadening of 1.2 eV. (B) Relaxed structures of ε- and δ-LiV_2O_5 phases used for XCH-XAS calculations in (A). The V=O length, interlayer spacing, and angle of puckering (V-O3-V) of the layers has been indicated for each phase. Red spheres depict oxygen atoms and blue spheres depict vanadium atoms, and green spheres, depict Li atoms. (C) Pre-edge region of calculated spectra indicating a diminution of pre-edge intensity accompanying lithiation. Reprinted from 47.

absorption features, which are thought to reflect a more complex scattering background as a result of the large scattering amplitude of ejected photoelectrons in this energy range.[98,219] The broadening of the spectral features as a result of this multiple scattering background obscures transitions to discrete electronic states. It is worth noting that orientational averaging across the nanowires also contributes to broadening of spectral features.

Figure IV.2A plots the measured spectra acquired at 54.7° incidence of the X-ray beam for nominal Li-ion stoichiometries *x* of 0.4 and 0.9 where as noted above the predominant $Li_xV_2O_5$ phases are expected to be the expanded and puckered ε-phase and the δ-phase (wherein alternating planes are shifted along the *b* direction by half a unit cell length), respectively.[162,163] The XCH-calculated spectra for ε- and δ-LiV_2O_5 are plotted alongside the experimental spectra; the relaxed structures used for the spectral simulations are depicted in Figure IV.2B. The changes to the interlayer spacing and V=O bond length are indicated, as well as the decrease in the V-O3-V angle as the puckering of the layers increases with phase evolution from the α (148.8°)→ε (134.9°)→δ (128.4°) phase. The good agreement of the pre-edge region between experiment and calculated spectra suggest that the V K-edge spectra capture the perturbations to the local geometry induced upon phase progression from V_2O_5 to ε- and then δ-$Li_xV_2O_5$ with increasing lithiation. An overlay of the pre-edge region of the calculated spectra shown in Figure IV.2C predicts that lithiation of V_2O_5 should induce a shift of the absorption to lower energies as well as a reduction of the peak intensity. Indeed, the experimental spectra in Figure IV.2A and Figure IV.3 clearly bears out this prediction. Figures IV.3A and B plot the V K-edge

spectra obtained at different concentrations of Li-ions. Upon the initial insertion of Li-ions (*x* of ca. 0.1), the pre-edge feature increases in intensity and is asymmetrically broadened at the lower energy tail. Differential (Δμ-XANES) spectra have been calculated by taking the difference between pre- and post-edge XANES spectra for $Li_xV_2O_5$ and V_2O_5 as per the method introduced by Ramaker,[199,220] and are shown in Figure A.2 (Supporting Information). A distinct peak is observed at 5470.2 eV in Figure A.2. The increase in the pre-edge intensity is a result of the incorporated Li-ions bringing about a further distortion of the square pyramids away from octahedral symmetry as a result of the puckering of the layers to enable Li—O coordination and the increased interlayer separation that further disrupts the long V—O interaction between layers. Fig. IV.2B shows the relaxed structures as calculated from DFT as well as the respective V=O bond lengths, interlayer spacings, and V-O3-V bond angles.[45] These parameters are derived from structures relaxed until each Cartesian component of the forces is less than 0.01 eV/Å. The asymmetric broadening and shift[202] of the area-weighted centroid to lower energies is a result of the reduction of a fraction of the V^{5+} sites to V^{4+} sites upon insertion of Li-ions. Indeed, our recent work indicates that upon initial reduction of vanadium sites, the electron remains localized within V $3d_{xy}$ orbitals with stabilization of a small polaron.[5,45] Upon such localized reduction, the excitation of core electrons

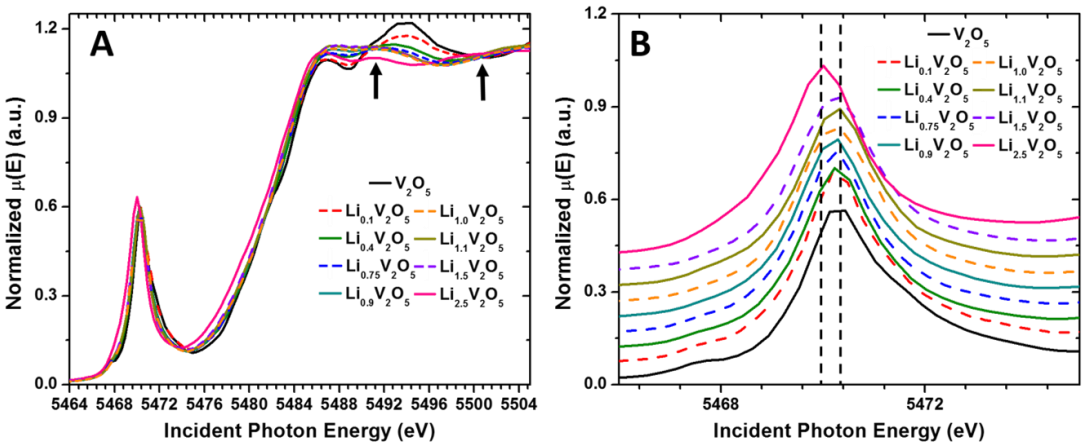

Figure IV. 3 (A) Comparison of $Li_xV_2O_5$ nanowires with nominal *x* values of 0.4 and 0.9 with XCH-XAS calculated spectra; the spectra reflect a Lorentzian broadening of 1.2 eV. (B) Relaxed structures of ε- and δ-LiV_2O_5 phases used for XCH-XAS calculations in (A). The V=O length, interlayer spacing, and angle of puckering (V-O3-V) of the layers has been indicated for each phase. Red spheres depict oxygen atoms and blue spheres depict vanadium atoms, and green spheres, depict Li atoms. (C) Pre-edge region of calculated spectra indicating a diminution of pre-edge intensity accompanying lithiation. Reprinted from 47.

requires less energy due to more screening charge at the excited atom,[58,200] and thus the pre-edge feature is shifted to lower energy.

As the Li content increases beyond $x = 0.1$, the pre-edge feature is further shifted to lower energies due to an increasing proportion of reduced vanadium sites. In addition to the red-shift of the peak position, the increase in V^{4+} character contributes to the broadening of the pre-edge peak, which is evidenced in the ΔμXANES spectra of Figure A.3 by the asymmetric sinusoidal lineshape near 5470 eV. The broadening is evidenced by the intensity of the positive peak in the difference spectrum (0.059) being higher at its maxima of 5469.5 eV than the negative peak minima (-0.051) at 5470.7 eV. With

continuing lithiation, Figure IV.3A as well as Figure IV.4A and B illustrate the appearance of two distinct isosbestic points within the $0.1 \leq x \leq 1.5$ regime at 5491.2 and 5500.4 eV.

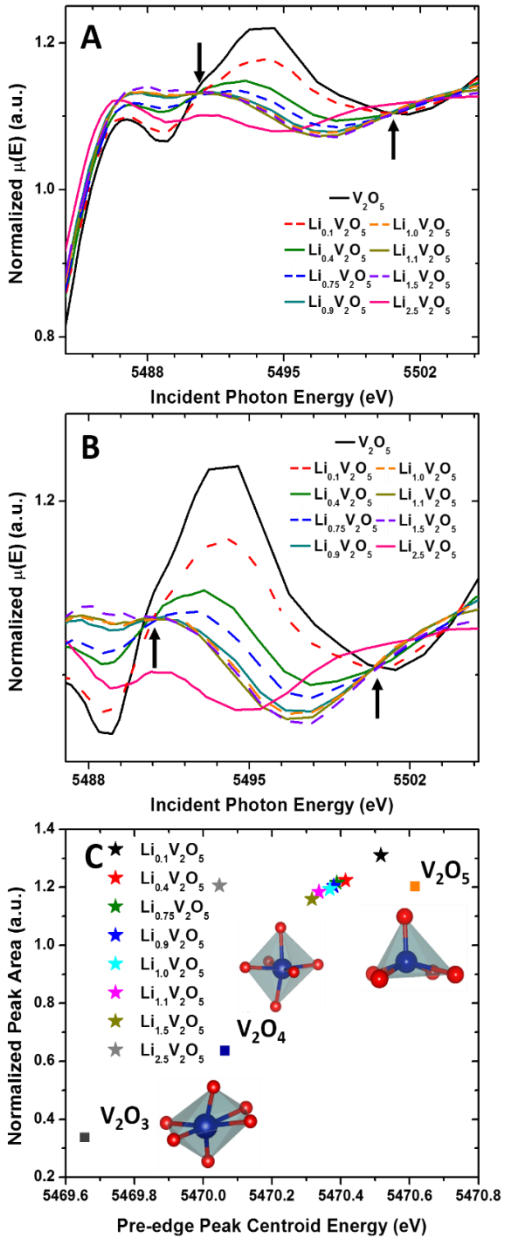

Figure IV. 4 (A) Post-edge region of XANES spectra from Figure IV.3A, indicating isosbestic points in the two-phase regime between $0.1 \leq x \leq 1.5$. An enhanced view of the isosbestic points is depicted in panel (B). (C) 2D intensity and peak position plot of the pre-edge peak of $Li_xV_2O_5$ nanowires mapping the evolution of the oxidation state and site symmetry of vanadium atoms with increasing lithiation. Reprinted from 47.

The spectra acquired for $Li_{0.1}V_2O_5$ and $Li_{0.4}V_2O_5$ are characterized by a distinct absorption at ca. 5494.0 eV that is shifted from the absorption of V_2O_5. Further lithiation leads to smearing of this feature but distinctive isosbestic points are observed at the low and high energy ends of this feature and indicate that within this stoichiometry range, lithiation proceeds through classical two phase behavior wherein the concentration of one species grows at the expense of the other. At $x = 2.5$ with stabilization of the ω-phase (Fig. A.3) shows the indexed XRD pattern for this phase), the pre-edge peak is shifted to a substantially lower energy (5470.0 eV) and the edge jump resonance is shifted to a lower energy by ca. 0.5 eV. The latter spectrum does not intersect at the isosbestic point indicating conversion to an altogether different crystal structure from the two phases observed in the $0.1 < x < 1.5$ range.

The pronounced and mostly monotonic changes in the intensity and peak positions of the pre-edge feature apparent in Figure IV.3B can be understood in terms of modifications to the formal vanadium oxidation state and the coordination environment as predicted for ε- and δ-LiV_2O_5 in Figure IV.2. In a seminal paper, Giuli *et al.* first reported the correlation of vanadium oxidation state and symmetry with pre-edge peak height and energy in 2004 and developed a two-dimensional plot relating these parameters across a wide range of minerals.[221] Chaurand *et al.* have since refined this formalism wherein the area and position of the V K-edge pre-edge peak can be plotted on a 2D plot and compared to reference compounds of known oxidation states and symmetries.[58,59,221] Much can be surmised about the local geometry and oxidation state of a compound based on the relative

positioning of the intensity and peak position of the pre-edge feature, respectively, in such a plot. The 2D plot in Figure IV.4C enables comparison of $Li_xV_2O_5$ phases of varying Li-ion stoichiometries to binary vanadium oxide standards. A monotonic shift of the pre-edge feature to lower energies is consistent with increased reduction of vanadium sites. The intensity of the pre-edge feature is closely related to the local vanadium coordination geometry. The lithiation-induced diminution of the pre-edge peak intensity is further corroborated by the calculated spectra depicted in Figure IV.2C. The binary vanadium oxide VO with perfectly octahedral symmetry does not have a pre-edge feature at all due to the perfect octahedral symmetry that precludes V 4p-3d hybridization. The greater the structure deviates from octahedral symmetry, the stronger the extent of V 4p—3d hybridization, which in turn is reflected in a stronger pre-edge absorption. For instance, Figure IV.4C indicates a substantial pre-edge intensity for V_2O_4 constituted from Jahn-Teller-distorted octahedra.[19] As noted above, the *ungerade* character of the final states (Fig. IV.1B, inset) resulting from substantial p—d hybridization results in the transitions becoming dipole allowed for V_2O_5. Figure IV.4C indicates that the initial formation of $Li_{0.1}V_2O_5$ results in a shift of the peak centroid from 5740.62 to 5740.52 eV, whereas the peak area shows a significant increase owing to the broadening that occurs as a result of the formation of V^{4+} sites as well as an increased distortion of the [VO_5] square pyramids to facilitate Li—O coordinative interactions. Further lithiation to x = 0.4 brings about a further significant shift of the pre-edge centroid energy to 5740.1 eV reflecting increased reduction. The intensity of the pre-edge absorption reverts to that of V_2O_5 as a result of the slightly more symmetric [VO_5] square pyramids stabilized in the ε-phase. Note that

Raman spectroscopy indicates that V=O bonds are elongated in the ε-phase as a result of the lower oxidation state thereby increasing the local symmetry.[48,75] Sipr *et al.* have predicted a direct correlation between the length of the V=O bonds and the intensity of the pre-edge absorption and have suggested that such a feature should entirely disappear for bond lengths in excess of 2.2 Å. DFT calculations indeed suggest that the V=O bond length increases from 1.604 Å to 1.634 Å for ε-LiV_2O_5 and 1.631 Å for δ-LiV_2O_5 (Fig. IV.2B). From x = 0.4 through x = 1.5, there is a monotonic shift of the pre-edge peak to successively lower energy and an associated decrease in peak area. While severe puckering and gliding of the layers occurs upon conversion to the δ-phase at x = 0.9 with eventual inversion of square pyramids upon forming the γ-phase at 1.0, the local symmetry becomes more octahedral-like as the structure is transformed from a 2D layered solid to a 3D framework and this is reflected in a reduced intensity of the pre-edge feature. The highly lithiated ω-$Li_{2.5}V_2O_5$ is an outlier in Figure IV.4C (Fig A.3 indicates that this structure can be indexed predominantly to the ω phase). The peak position of 5470.0 eV indicates reduction of all vanadium sites beyond V^{4+}. The high intensity of the structure suggests a strong degree of local asymmetry, which would belie claims of stabilization of a disordered rock-salt structure. It is worth noting that a structure solution for this phase has proved elusive and some authors claim that a mixture of various reduced vanadium oxides, including Li_2VO_4, $LiVO_2$, and V_2O_3 is instead stabilized.[92] A conclusive determination of the origin of the anomalous behavior observed for this sample is not possible given the absence of a structure solution.

IV.3.2 MCR Analysis of V K-edge XANES Spectra

The presence of isosbestic points in the XANES spectra plotted in Figures IV.3A, IV.4A and IV.4B as well as the broadening of the spectra upon lithiation most clearly discernible in the Δμ-XANES spectra plotted in Figure A.2 suggest that lithiation of V_2O_5 is heterogeneous. Indeed, previous Raman and STXM analysis suggest the presence of lithiation gradients, which in turn result in the stabilization of distinctive domains.[18,43] Given the presence of spectral signatures from distinct vanadium sites, PCA provides a means for chemometric spectral deconvolution and can be used to evaluate the chemical species present in the data matrix. Indeed, the application of PCA and MCR to the V_2O_5 cathode system was first reported by Conti *et al.* at the Cu K-edge for doped samples.[102] Typically, a positive-definite constraint is used in chemometric spectral deconvolution in order to guide the model away from creating unphysical factors containing values of negative concentrations for present species.

MCR spectra have been calculated from the PCA results and the calculated variance of XANES spectra acquired in triplicate for the stoichiometrically lithiated samples (Fig. IV.5). The percentages of calculated functions indicated in Figure IV.5 correspond to the amount of the total variance that is used to build a given function, whereas scores on these functions represent the fraction of a sample's variance that is described by the calculated function. The sum of the three functions account for approximately 100% of the variance across the spectral dataset *sans* residuals. Owing to this fact, selecting the correct number of components is key to a physically meaningful MCR calculation. The inclusion of additional components has been tested and does not

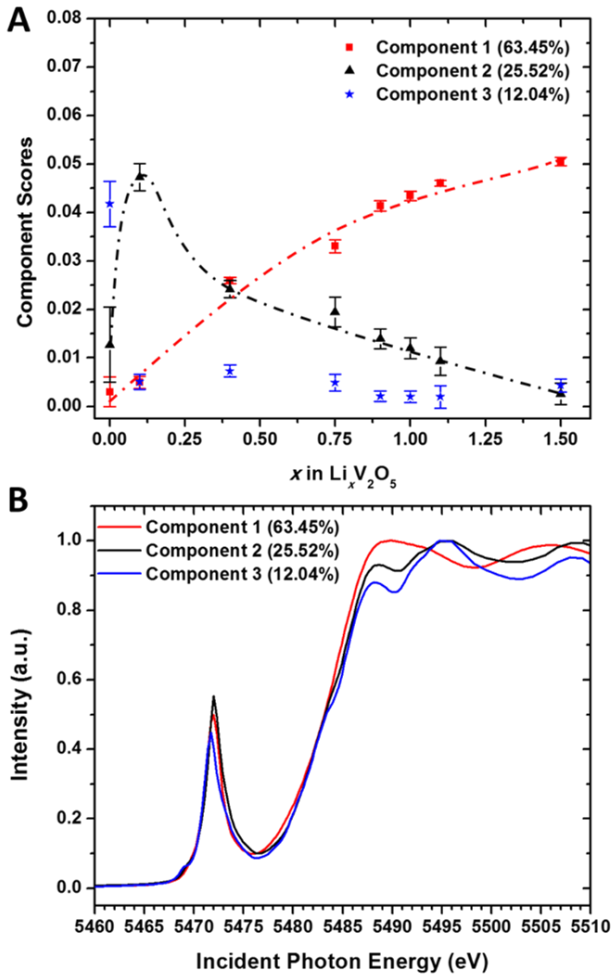

Figure IV. 5 (A) Scores of each lithiated sample on components as determined by MCR analysis; the scores were calculated by analysis of spectral data acquired in triplicate. The error bars represent the first standard deviations in each case. The lines indicated for components 1 and 2 are guides to the eye. (B) MCR-generated XANES spectra. Reprinted from 47.

yield any additional distinctive spectral signatures and thus a three-component model is posited to be sufficient to describe the variances in the current data set. The calculated components are plotted in Figure IV.5B. MCR spectra are representative of the total spectral variances and do not directly correspond to experimental spectra but the

components can nevertheless be assigned to characteristic vanadium symmetry and oxidation state.

The V K-edge XANES spectra of unlithiated V_2O_5 nanowires are shown to be well described by component 3 to the exclusion of all other components, and thus this component can be reasonably assigned as primarily being characteristic of pristine V_2O_5. Upon lithiation to $x = 0.1$, the contribution of component 3 drops to a near null score, and instead the spectral profile is predominantly described by component 2, which in turn is thus posited to be descriptive of the low lithium-content α-phase, characterized by a high V^{5+}/V^{4+} ratio (Fig. A.4, Supporting Information, compares the powder XRD patterns of unlithiated and α-$Li_xV_2O_5$). Upon increasing lithiation, to $x = 0.4$ the contribution of component 2 to the total variance decreases, and instead component 1 makes up the difference. Indeed, this trend persists up to $x = 1.5$ with progressively increased weighting of component 1 and reduced scores for component 2. Since component 1 is the sole component that contributes meaningfully to the $x = 1.5$ spectrum, the physical interpretation of this function is that it represents a relatively highly lithiated (and thus more reduced) V_2O_5 phase, wherein the V^{5+}/V^{4+} ratio is less than 0.5, which would correspond to the closely related high Li-ion-content ε- and δ- LiV_2O_5 phases depicted in Figure IV.2B. The evolution of the MCR scores indicates that V_2O_5 is first transformed to a low lithium-content phase, which serves as the precursor for gradual conversion to more highly lithiated phases. The discrete components generated by MCR (Fig. IV.5B) are consistent with the above assignments, particularly with regards to the evolution of intensity of the pre-edge feature. From component 3 to component 2, an increase in pre-

edge peak intensity and broadening is observed as ascribed above to the transition from pristine V_2O_5 to the puckered α-$Li_xV_2O_5$ phase characterized by more strongly distorted [VO_5] square pyramids. Subsequently, upon more extensive lithiation, a pronounced decrease in intensity and peak width of the pre-edge feature is observed for component 1. While the shift to lower energies is not precisely captured for the pre-edge feature, the primary absorption edge is clearly shifted to lower energies from component 3 to 2 to 1, consistent with increasing lithiation (Fig. IV.5B). Similarly, in the region above the absorption edge, a two-peak structure with distinctive features at 5488.1 and 5495.5 eV are observed for components 1 and 2, whereas with increasing lithiation, this feature is greatly broadened as observed in Figure IV.2 for the more extensively lithiated samples.

IV.3.3 Dynamics of Li-ion insertion at Low Rates

The chemical lithiation of V_2O_5 under stoichiometric conditions can be seen as an analog to low rate discharge of an electrochemical cell or to discharging a cell at a low applied overpotential. The use of chemical lithiation allows for phase progression to be monitored without interference from binders or conductive fillers commonly used in electrode construction. Additionally, the homogeneity of lithiation *via* solution-phase reaction eliminates the inherent directionality associated with electrochemical insertion. Consequently, any phase heterogeneities observed are purely the products of diffusion barriers and kinetic traps inherent to the material rather than spatial inhomogeneities within an electrode. The MCR analysis suggests that initial lithiation of V_2O_5 results in the homogeneous stabilization of the low-lithium-content α-$Li_xV_2O_5$ phase with *x* of ca.

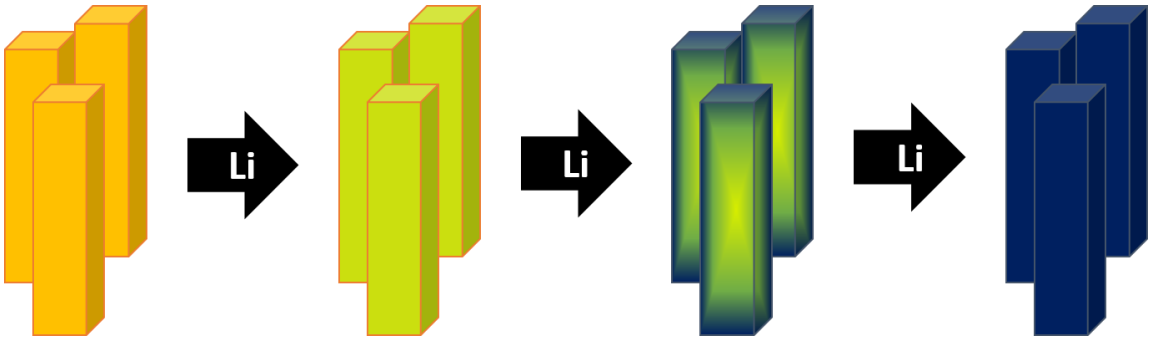

Figure IV. 6 Schematic illustration of the phase progression induced by chemical lithiation of V_2O_5 as determined from V K-edge XANES measurements. Pristine V_2O_5 is first homogeneously converted to the low-lithium-ion α-phase. From this point, further insertion of Li-ions results in supersaturation of the low-concentration phase, resulting in nucleation of the high Li-ion concentration phase at nanowire edges. This high-lithium-ion phase then propagates through the wire until full conversion is achieved. Reprinted from 47.

0.1. After the transformation of the pristine orthorhombic phase of V_2O_5 to the low-lithium-content α-phase, any further incorporation of Li-ions necessitates the nucleation of a higher lithium-content phase. This phase subsequently grows at the expense of the low-lithium phase upon increasing insertion of Li-ions as schematically illustrated in Figure IV.6. The phase segregation between low- and high-lithium-content phases is thought to be a result of the stabilization of small polarons in V_2O_5, which impede equilibration of charge density. Individual nanowire STXM studies of lithiated V_2O_5 nanowires indicate that trapping of an electron in V $3d_{xy}$ states and an accompanying structural distortion can limit both ionic and electronic conduction.[45] Nudged elastic barrier calculations suggest a 0.22 eV barrier to the diffusion of Li-ions as a result of polaron formation. With increasing lithiation, the α-$Li_xV_2O_5$ phase becomes supersaturated, leading to the nucleation of the higher lithium content phase, which can

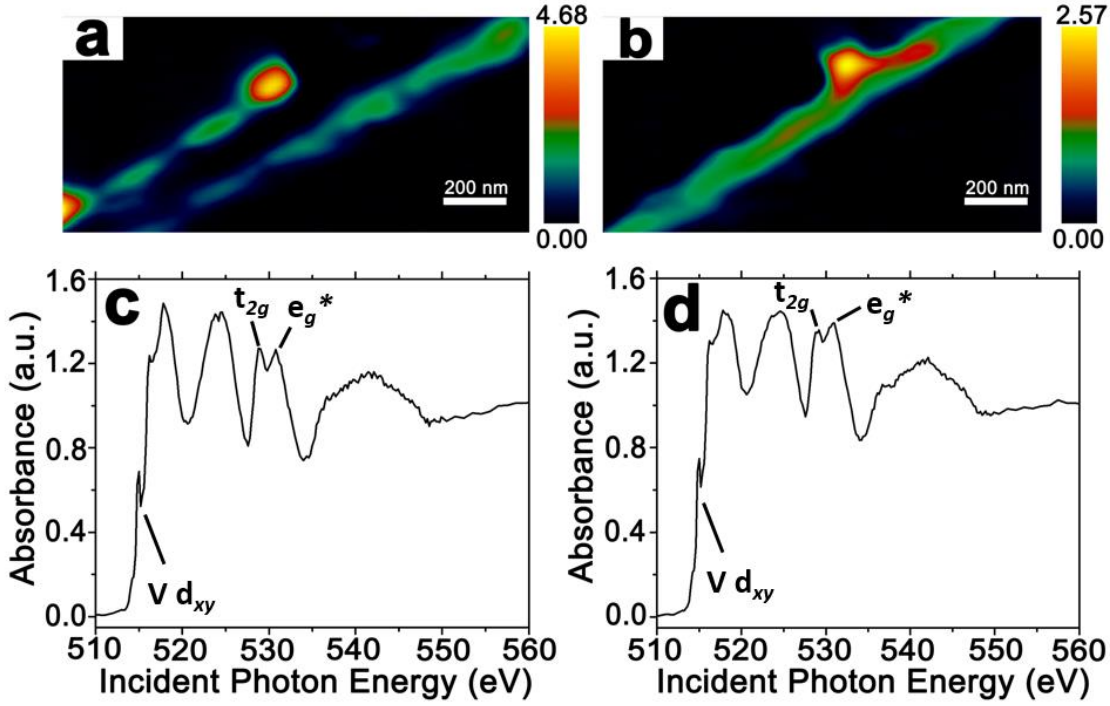

Figure IV. 7 Two distinct spectral contributions can be deconvoluted and spatially resolved for an individual nanowire of LiV_2O_5 (x = 1). Panels (a) and (b) represent intensity maps for spectral contributions plotted in (c) and (d), respectively. The edges of the nanowire as viewed in this figure correspond to the *ab* planes that define the top and bottom of the nanowire; these regions are relatively less lithiated based on the relatively lower t_{2g}:e_g* ratio. In contrast, the central region of the nanowire, as viewed between the layers represent a high-lithium-ion phase of the nanowire as indicated by the inversion of the t_{2g}:e_g* ratio. Reprinted from 47.

be preferentially stabilized across specific regions of the nanowires. The high-lithium-content phase then grows preferentially instead of nucleating additional lithiated phases with intermediate extents of lithiation (Fig. IV.6). To directly probe this phenomenon, an individual V_2O_5 nanowire stoichiometrically reacted to obtain a LiV_2O_5 stoichiometry has been imaged by STXM as shown in Figure IV.7. STXM images have been acquired at V L and O K-edges. The V L_{III} resonance corresponds to transitions from singlet V $2p^6 3d^0$

into V $2p^5 3d^1$ states as modified by crystal field splitting and multiplet effects.[45,60,61] The first sharp low-energy feature at the V L_{III} edge is attributed to a transition to a final state of predominantly V $3d_{xy}$ symmetry observed at ca. 514.9 eV, whereas the second feature at ca. 515.5 eV is thought to be primarily V $3d_{xz/yz}$ in origin.[45,60] Life-time broadening, arising from a Coster-Kronig Auger decay process, which fills the X-ray excited $2p_{1/2}$ hole with a $2p_{3/2}$ electron, renders the V L_{II} edge less informative. In contrast, the O K-edge corresponds to transitions of core level O1s electrons to O 2p states that are hybridized with V3d states and are thus split into two sets of features reflective of sideways O2p—V3d π interactions with V3d orbitals of t_{2g} symmetry (V$3d_{xy}$, $3d_{xz}$, $3d_{yz}$; centered at ca. 529.7 eV) and collinear O2p—V3d σ interactions with V3d orbitals of e_g symmetry (V$3d_{z2}$, $3d_{x2-y2}$). Based on density functional theory calculations, ensemble V L- and O K-edge X-ray absorption near edge structure measurements, and STXM imaging, the lithiation and concomitant reduction of V_2O_5 modifies the X-ray absorption spectra in the following manner: (1) the V$3d_{xy}$ feature at the V L_{III} edge, which represents the lowest lying level in the conduction band, is strongly diminished as a result of localized reduction (DFT calculations predict that electrons are localized in these orbitals wherein they couple with a structural distortion to define a polaron); (2) the ratio of t_{2g}:e_g features is greatly diminished at the O K-edge as a result of the localized structural polarization, rehybridization of the V=O bonds, and the electron correlation induced loss of spin degeneracy, which splits the V3d states into two non-degenerate spin channels.[45] These spectral features are thus strongly dependent on the extent of lithiation. In Figure IV.7, region of interest analysis of STXM data acquired for an individual nanowire allows for

the identification of two distinct domains that show a marked contrast in the ratio of the t_{2g} and e_g features. The distinctive stabilization of two domains provides direct corroboration of the V K-edge findings suggesting nucleation and growth of a highly lithiated V_2O_5 (Fig. IV.7b and d) from α-V_2O_5 (Fig. IV.7a and c) with a pronounced phase coexistence regime.

The observation of lithiation gradients and phase coexistence by V K-edge XANES spectroscopy suggests a primary role for nucleation and growth of the highly lithiated phases. Indeed, such a classical nucleation and growth pathway is observed for $LiFePO_4$ at low rates and gives rise to pronounced phase inhomogeneities between Li-rich and Li-poor phases.[190] However, in this compound, high-rate lithiation proceeds *via* an alternative single-phase pathway involving the stabilization of a solid solution; the metastable solid solution spinodally decomposes into a thermodynamically more stable mixture of highly lithiated $LiFePO_4$ and pristine $FePO_4$ domains upon removal of the driving force.[53,185] However, the XRD patterns in Figure A.4B suggest that the $Li_xV_2O_5$ nanowires examined here are unchanged from a few minutes after lithiation up to several weeks. Concurrent with the observation of two-phase behavior, this data appears to rule out spinodal decomposition as the origin of the observed phase coexistence and instead suggests the nucleation and growth of the highly lithiated phase at the expense of the low-Li-concentration phase. It is likely that the diffusion barriers resulting from small polaron formation will also impede spinodal decomposition of the highly lithiated phases.

IV.4 Conclusion

The formation of concentration gradients and phase segregation within cathode materials during discharge leads to the generation of intercalation induced stresses and subsequent loss of electrode capacity. Understanding heterogeneities in phase evolution and reduction is thus imperative for cathode design. V K-edge XANES spectroscopy is shown to be an excellent probe of vanadium local structure and allows for mapping of the lithiation-induced phase evolution of V_2O_5. The peak position and intensity of the pre-edge feature and the position of the primary absorption serve as sensitive probes of the vanadium oxidation state and local symmetry. The DFT-based XCH calculations yield spectra that are in excellent agreement with the XAS measurements, and capture the subtle chemical shifts induced by lithiation, including the peak intensity and relative alignment. The XAS calculation also confirms the origin of the sharp pre-edge feature of V_2O_5 ; this feature arises from a dipolar (and not a quadrupolar) transition from V 1s to hybrid V 4p—3d states that are further hybridized with O $2p_z$ states of the apical oxygen atoms. With increasing lithiation, the pre-edge feature as well as the absorption edge are shifted to lower energies, whereas the intensities of the pre-edge features are initially increased and then monotonically decreased reflecting the distortions to the local symmetry of the vanadium atoms and mapping the changes of the vanadyl bond. The presence of isosbestic points in the V K-edge spectra are suggestive of a classical two-phase mixture in the range $0.1 < x < 1.5$ for $Li_xV_2O_5$. MCR analysis of the V K-edge XANES data allows for mapping of the phase evolution. The incorporation of Li-ions into the host V_2O_5 lattice is seen to progress by initially forming a homogeneous low-lithium-content phase, which upon

supersaturation nucleates a high-Li-content phase. The latter phase grows at the expense of the former with increasing lithiation without the stabilization of solid-solutions of varying Li content. The observed phase segregation between Li-rich and poor phases is attributed to the stabilization of small polarons that impede ion and electron transport in this material and has further been verified by STXM imaging of individual stoichiometrically lithiated nanowires.[45] More generally, MCR methods are shown to be an excellent probe for mapping phase mixtures stabilized during discharge of cathode materials from X-ray absorption spectroscopy data.

CHAPTER V

MITIGATING CATION DIFFUSION LIMITATIONS AND INTERCALATION-INDUCED FRAMEWORK TRANSITIONS IN A 1D TUNNEL-STRUCTURED POLYMORPH OF V_2O_5[*]

V.1 Introduction

As a result of their superior energy density, power density, and cyclability, Li-ion batteries have emerged as the principal energy storage technology for most commercial applications. However, there remain many limitations to Li-ion batteries that have thus far hindered realization of their full potential in applications such as electric vehicles and grid-level storage. Existing capacity/volume and power/weight ratios are inadequate, and the cyclability and cost of large Li-ion battery packs represents a further impediment to more widespread adoption of this technology. The part of the battery architecture most opportune for further improvements is the cathode. In general, the design of an effective cathode requires balancing of many correlated and only partially correlated material characteristics.[222] High electronic and ionic conductivities are of primary importance, but safety, earth abundance, and cost are salient concerns as well.[187,223] While achieving the highest energy densities, layered cathodes based upon the LiCoO2 structure, including the Li-rich NMC materials that substitute cobalt

[*] Reprinted with permission from "Mitigating Cation Diffusion Limitations and Intercalation-Induced Framework Transitions in a 1D Tunnel-Structured Polymorph of V_2O_5" Horrocks, G. A.; Parija, A.; Dr Jesus, L. R.; Wangoh, L.; Andrews, J. L.; Jude, J. W.; Jaye, C.; Fischer, D. A.; Piper, L. F. J.; Banerjee, S. *Submitted.*

centers for nickel and manganese are still plagued by poor high rate performance, high cost due to the relative scarcity of cobalt and nickel, and safety considerations[186] derived from the highly oxidizing nature of the delithiated phase. Owing in large part to the high-rate and safety limitations of the Li-rich NMC materials, there has recently been considerable interest in the olivine LiFePO4 family of materials.[224] Although LiFePO4 has a lower energy density than the layered cathode materials, it exhibits distinctive advantages in terms of cost, safety, and high-rate performance. The interest in LiFePO4 stems largely from its improved high-rate performance. This characteristic arises from the ability to access a non-equilibrium solid-solution pathway, wherein upon lithiation, the nucleation of the Li-rich LiFePO4 phase is subverted by stabilization of a metastable solid-solution LixFePO4 phase that mediates a gradual evolution between FePO4 and LiFePO4 at high rates. This pathway thereby precludes the need to go through an energy dissipative nucleation and growth process wherein the Li-rich phase is nucleated and grows upon supersaturation of the Li-poor phase.[53,185] However, upon removal of an applied voltage, the metastable phase undergoes spinodal decomposition to form a mixture of LiFePO4 and FePO4. Inhomogeneities in extent of lithiation or depth of discharge across the cathode, either across the span of an individual particle, or across the constituent particles of a porous electrode undergoing sequential particle-by-particle transformation, are deleterious for long-term cyclability since they give rise to highly enhanced local current densities and establish large inhomogeneous strain gradients.[40–42,46,225] One approach to

mitigating such inhomogeneities involves the careful design of mesoscale frameworks; however, heterogeneity in large measure derives from surface and material characteristics. Consequently, the design of structures that can reversibly and continuously accommodate large concentrations of Li-ions without substantial distortion or transformation of the framework has emerged as a critical imperative for realization of efficient high-rate cycling. Such design requires consideration of both geometric and electronic structure.[67,226–229]

The layered vanadium oxide phases have long been of interest as potential cathode materials due to their ability to (somewhat) reversibly accommodate a high density of guest cations (up to x = 3.0 in LixV2O5 for Li+), as well as their relatively low cost, and stability in their fully oxidized state.[3,5,230] However, in the bulk, orthorhombic layered V2O5 suffers from poor Li-ion diffusion, poor electrical conductivity, and a predilection for anti-site disorder. In this material, lithiation brings about a series of phase transformations involving an increase of interlayer spacing, puckering of the individual layers, rearrangement of [VO5] square pyramids, and finally conversion to a highly disordered cubic phase.[1,6,48,231] While phase separation is strongly suppressed for ultra-thin V2O5 nanoplatelets with thicknesses < 80 nm, considerable evidence for phase inhomogeneity is observed upon lithiation of V2O5 nanowires with diameters on the order of 100—200 nm.[45,47,48] In recent work, we have established that the origin of pronounced lithiation gradients and resulting phase separation in orthorhombic V2O5 is (i) stage ordering of Li-ions within the layered V2O5 lattice wherein individual layers are

filled prior to initiating lithiation of a subsequent layer; and (ii) stabilization of small polarons at low Li-ion concentrations wherein a lattice distortion couples with localized electron density necessitating the transport of the entire quasiparticle across the lattice.[45,47] Mitigating these impediments and addressing the energy dissipation and inevitable hysteresis accompanying intercalation-induced phase transformations requires either nanostructuring or the identification of an entirely different framework.

Ternary vanadium oxides with the formula MxV2O5 (where M is an intercalated cation and x is its stoichiometry) provide a rich tapestry of open framework structures with intercalated species.[1,5,232] Topochemical de-intercalation of cations from these structures yield metastable V2O5 frameworks that represent local minima on the free energy landscape that are nevertheless unable to convert to the thermodynamically stable orthorhombic V2O5 phase at reasonable temperatures.[2,233–235] Several of these structures show strikingly different bonding motifs and electronic structure as compared to the orthorhombic layered phase of V2O5. For instance, the recently reported ζ-phase of V_2O_5[2] retains many of the characteristics that make the orthorhombic V2O5 system attractive; the V+5/V+4 redox couple is easily accessible and the vanadium-centered polyhedra enclose a 1D tunnel with a high concentration of interstitial sites.[236] However, in contrast to orthorhombic V2O5, the ζ-phase structure exhibits increased covalency (which should serve to facilitate ionic diffusion through the structure) and the V 3d states at the top of the conduction band are energy degenerate as compared to

orthorhombic V2O5, which is characterized by a "split-off" V 3dxy-derived state.[66] The increased overlap of V 3d states allows for delocalization of charge and is hypothesized to reduce electron localization and small polaron formation.[66] However, modifications to electronic and geometric structure upon Li-ion intercalation have not thus far been studied for this material.

In this work, we investigate the chemical and electrochemical lithiation of nanowires of the novel 1D tunnel-structured ζ-phase of V2O5. Using a combination of X-ray absorption near-edge structure (XANES) spectroscopy, hard X-ray photoemission spectroscopy (HAXPES), powder X-ray diffraction (XRD), and density functional theory (DFT) calculations, we correlate the structural and electronic changes induced by Li-ion insertion within this material and investigate barriers to ionic diffusion within the 1D tunnels of ζ-V2O5. The distinctive atomistic and electronic structure of this material is found to substantially mitigate polaronic barriers and permits continuous incorporation of Li-ions without a large distortion of the framework.

V.2 Experimental

V.2.1. Synthesis of ζ-V_2O_5 Nanowires and their Chemical Lithiation

Nanowires of β-$Ag_{0.33}V_2O_5$ were synthesized by the hydrothermal reaction of bulk α-V_2O_5 (Sigma-Aldrich 99.5%) with silver acetate (Sigma-Aldrich), as previously reported.[2] ζ-V_2O_5 nanowires were obtained by topochemical leaching of Ag-ions from the β-$Ag_{0.33}V_2O_5$ nanowires by hydrothermal treatment with 15 mL of 0.71M HCl at 210°C

for 24 h.[2] The leached ζ-V_2O_5 nanowires were washed with water and isopropanol, and dried in air.

Orthorhombic layered V_2O_5 nanowires used to contrast the electronic structure changes induced by lithiation in XANES and HAXPES experiments were prepared as reported elsewhere[48] by the hydrothermal reduction of bulk V_2O_5 (Sigma-Aldrich) by oxalic acid (Sigma-Aldrich) to form nanowires of V_3O_7, which were subsequently oxidized in air at 350°C to yield V_2O_5.

The ζ-V_2O_5 nanowires were chemically lithiated by reaction with stoichiometric amounts of *n*-butyllithium in anhydrous toluene (EMD Millipore) for 96 h under an Ar atmosphere. The lithiated β(β')-$Li_xV_2O_5$ nanowires wires were then rinsed with copious amounts of hexanes, and allowed to dry under Ar. The samples were sealed under Ar for transport to synchrotron facilities for further characterization.

V.2.2. Electrochemical Lithiation and Cyclic Voltammetry

A thin film of ζ-V_2O_5 nanowires was deposited onto indium tin oxide-coated glass slides (Delta Technologies, Ltd.) by dispersing the nanowires in an ethanol/water solution and spray coating onto the heated substrate. Cyclic voltammetry was performed using a three electrode setup with the ζ-V_2O_5 thin film as the working electrode, and Li foil as the counter and reference electrodes. A 1.0 M solution of lithium trifluoromethanesulfonyl imide (LiTFSI, Sigma-Aldrich) in 1:1 mixture of ethylene carbonate (EC) : dimethyl carbonate (DMC, both from Sigma-Aldrich) was used as the electrolyte. The potential was scanned at a rate of 0.5 mV/s between 4.50 V and 2.00 V using a BioLogic SP-200 potentiostat.

V.2.3. Structural Characterization

All synthesized samples were characterized by powder XRD using a Bruker-AXS Advance D8 Bragg-Bretano X-ray Diffractometer with a Cu Kα radiation source (λ =1.54 Å). The nanowire morphology was examined by scanning electron microscopy (SEM, Hitachi SU-70 operated at 20 kV) and transmission electron microscopy (TEM, JEOL 2010 operated at 200 kV). Selected area electron diffraction patterns were acquired during TEM analysis to confirm the crystal structure.

V.2.4. Electronic Structure Characterization

XANES spectroscopy data was collected at the National Institute of Standards and Technology beamline U7A at the National Synchrotron Light Source of Brookhaven National Laboratory. A 1200 lines/mm toroidal mirror spherical grating monochromator with a nominal energy resolution of 0.1 eV was used for energy selection of the incident X-rays. Spectra were collected in partial electron yield mode. Auger electrons from the sample were detected by a channeltron multiplier set at an entrance grid bias of -200 V. All samples were mounted within the ultra-high-vacuum chamber using Cu tape. Charging of the sample was prevented by use of a charge compensation gun. The reference standard was an evaporated vanadium mesh, which allowed for calibration of the energy scale. All spectra were normalized to the incident beam intensity measured by photoemission from a Au grid with 90% transmittance situated upstream of the sample. Spectra were acquired at both V L- and O K-edges in a single scan. All spectra have been pre- and post-edge normalized using the Athena suite of data processing tools.[209]

HAXPES data was collected at the National Institute of Standards and Technology bending magnet beamline X24 of the National Synchrotron Light Source of Brookhaven National Laboratory. Spectra were collected at an incident photon beam energy of ca. 4 keV with a 500 eV pass energy and Gaussian instrumental broadening of 0.45 eV. A gold foil reference in electrical contact with the samples was used for energy alignment of the HAXPES spectra to the fermi level, with Au reference scans performed before and after each sample spectrum to account for energy alignment shifts. There was no evidence of charging observed during measurement.

V.2.5. DFT Calculations

Electronic structure calculations were performed using density functional theory (DFT)[210] as implemented in the Vienna *ab initio* simulation package (VASP).[212,237] Generalized gradient approximation (GGA) of Perdew–Burke–Ernzerhof (PBE) functionals were implemented to describe the electron exchange-correlation interactions.[213] Electron—ion interactions were incorporated using the projector-augmented wave (PAW) formalism. Electronic structure was described within a plane-wave basis with a well-converged kinetic energy cutoff of 600 eV.[217] A rotationally invariant density functional theory (DFT+U) formalism of Dudarev el al. was used for the addition of on-site Coulomb interactions.[238] The effective on-site coulomb interaction parameter of U = 4.0 eV was used as previously benchmarked in literature.[239] Also, all the structural calculations were performed using the vdw-DF2 functionals developed by Langreth and Lundqvist,[240–243] to include the van der Waals' interactions. For the total energy convergence and the calculation of electron density the first Brillouin zone was

sampled with a Γ-centered centered Monkhorst-Pack reciprocal grid of 2×2×2 k-points. However, a 4×4×4 k-points grid was considered for accurate density of state calculations. A 1x2x1 supercell was considered for all the electronic calculations. Unless otherwise mentioned, the cell shape, volume, and atomic positions were fully relaxed for all structures. All the structures were relaxed until each residual Cartesian force component decreased to values less than 0.03 eV $Å^{-1}$ for each atom. The criterion for the convergence of the self-consistency cycles is 10^{-6} eV. A threshold value of 10^{-6} eV was used for the convergence of electronic self-consistency cycles.

GGA+U calculations based on the formalism of Dudarev et al. with the addition of a Hubbard term, as implemented in VASP, were performed to remove the non-cancellation of self-interaction errors of d-electrons of vanadium atoms. A value of U = 4.0 eV was used as previously benchmarked in the literature. In order to account for der Waals' interactions, vdW-DF2 functionals were used as developed by Langreth and Lundqvist.

V.3 Results and Discussion

V.3.1. Structural Changes upon Li-ion Insertion

The ζ-phase of V_2O_5 has a 42-atoms unit cell characterized by three crystallographically inequivalent vanadium atoms (Fig. V.1A). Two sets of VO_6 octahedra form edge-sharing chains along the *b*-direction, which are further linked by corner sharing in the *a*-direction. Edge-sharing VO_5 square pyramids form chains along the *b*-direction, which serve to connect the chains of edge-sharing octahedra in the *c*-direction.[2] These features together define 1D tunnels that propagate along the *b*-direction and define an open

framework amenable to cation intercalation and diffusion. Upon Li-ion intercalation, two distinct interstitial sites within the tunnels are filled as a function of Li-ion concentration (Fig. V.1B). For $x \leq 0.33$, the Li-ions reside in five-coordinate β-sites yielding β-$Li_xV_2O_5$.[233] With increasing concentration of Li-ions, above $x = 0.33$, and up to the stoichiometric limit of $x = 0.66$, smaller and more closely spaced quasi-tetrahedral β′ sites shifted half-an-unit-cell length are occupied instead (Fig. V.1B).[5,128,233]

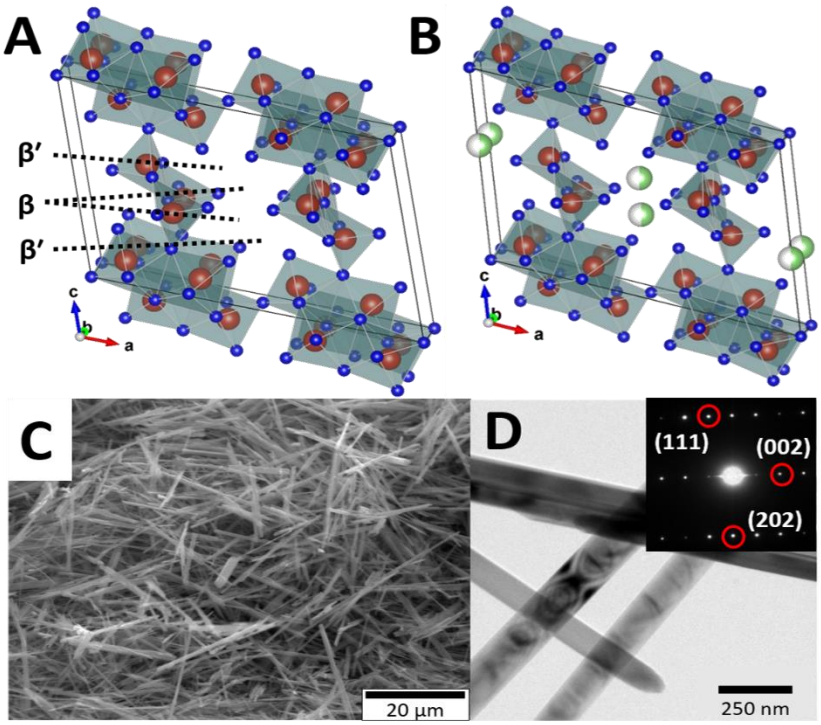

Figure V. 1: Crystal structures of A) Empty 1D ζ-V_2O_5 with the locations of the β and β′ intercalation sites indicated and B) fully intercalated β'-$Li_{0.66}V_2O_5$. Red vanadium atoms are depicted at the centers of polyhedra defined by blue oxygen atoms. Li atoms are shaded in green. The distinctive β and β' sites along the tunnel are noted. The black lines demarcate the unit cell in each case. C) SEM image and D) TEM image of as synthesized ζ- V_2O_5 nanowires. The inset to (D) indicates an indexed SAED pattern along the (010) zone axis.

Figures V.1C and D illustrate SEM and TEM images of the as-synthesized ζ-phase V_2O_5 nanowires, respectively. The lateral dimensions of the nanowires range from 147±36 nm based on electron microscopy measurements of 60 nanowires. The nanowires span several microns in length and are single crystalline as also illustrated by the SAED pattern in Figure V.1D.[2] Figure V.2A depicts a powder XRD pattern acquired for the as-synthesized ζ-V_2O_5 nanowires, which has been indexed as per our previous structure refinement.[2] The pattern is contrasted to patterns acquired for chemically lithiated nanowires with nominal Li-ion stoichiometries of $x = 0.33$ and 0.66 in $Li_xV_2O_5$. The shifts of the reflections are quite subtle indicating that the structural framework is largely preserved upon lithiation (Fig. V.2B shows a magnified view). No new phases are observed and indeed the diffraction patterns indicate phase-pure materials, which is in stark contrast to lithiation of orthorhombic V_2O_5 nanowires of comparable dimensions wherein phase mixtures are obtained due to constraints on Li-ion diffusion and nucleation

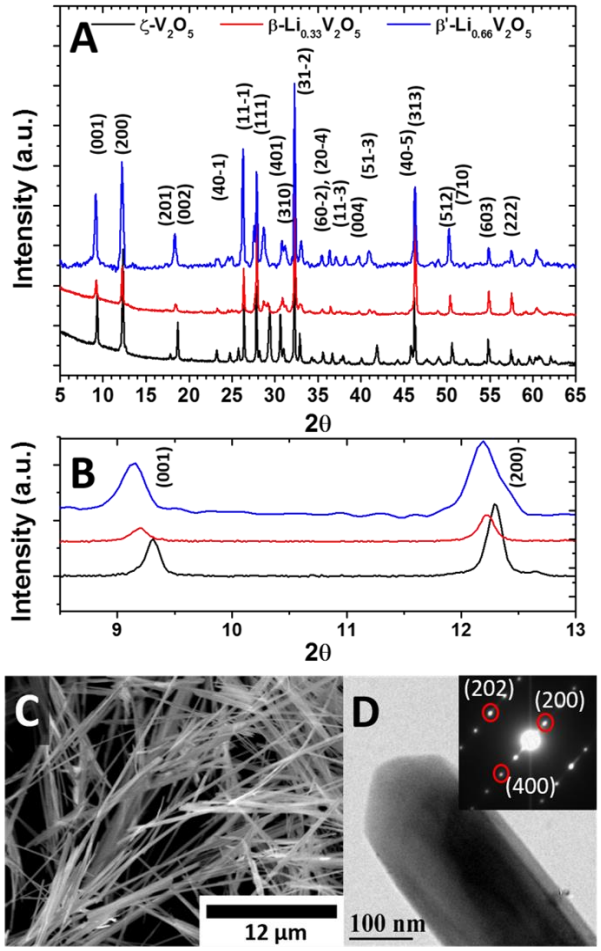

Figure V. 2: A) XRD patterns acquired for ζ-V_2O_5, β-$Li_{0.33}V_2O_5$, and β-$Li_{0.66}V_2O_5$ nanowires. B) Magnified view of 2Θ = 8—13° region. C) SEM image indicating the morphology of β-$Li_{0.66}V_2O_5$ and D) TEM with SAED pattern along the (010) zone axis indicating retention of the single crystalline nature and suggesting fully topochemical Li-ion insertion.

and growth of lithiated phases.[47,48] Some broadening of the reflections is observed, which is attributed to particle-to-particle variations in the extent of lithiation. Figure V.2B provides an enhanced view of the low-angle reflections that are most strongly shifted upon lithiation. The (001) reflection can be seen to shift from 9.45 Å for the as-prepared ζ-phase to 9.59 Å and 9.68 Å for β-$Li_{0.33}V_2O_5$ and β′-$Li_{0.66}V_2O_5$, respectively, as the lattice

expands with increasing Li-ion concentration. This lattice expansion is also observed in the shift of the (200) reflection from 7.17 Å for the pristine phase to 7.21 Å for β-$Li_{0.33}V_2O_5$ and 7.24 Å for β′-$Li_{0.66}V_2O_5$. The diminution in peak intensity for {200} reflections upon lithiation is explicable considering that these planes bifurcate the two β-sites where the inserted cations reside; destructive interference from inserted Li-ions residing at the these sites reduces the intensity of these reflections. Based on refinement of the cell parameters, lithiation brings about lattice expansion with the total unit cell volume expanding from 523.81 $Å^3$ for the pristine phase to 534.52 $Å^3$ for the fully intercalated x = 0.66 phase, which makes for a total volume expansion of 2.04%.[2] This relatively small volume expansion is the origin of the retention of the morphology evidenced in Figures V.2C and D. Both SEM and TEM evaluation of the nanowires provides no indication of crack initiation or pulverization and the indexed SAED pattern

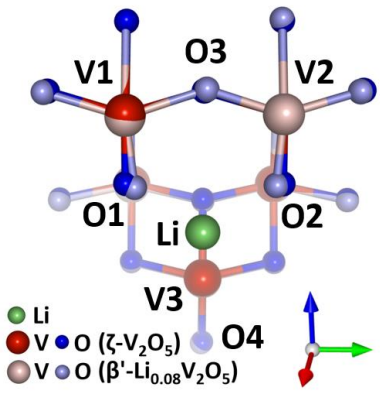

Figure V. 3: Structural rearrangement of ζ-V_2O_5 upon Li-ion intercalation as deduced from DFT+U calculations (see also Video A.1). Darker shade balls and sticks represent atomic positions of the as-prepared ζ-phase, whereas lighter colors denote the atomic positions in the lithiated β'-$Li_{0.083}V_2O_5$ phase.

indicates that the obtained nanowires are single crystalline suggesting that chemical lithiation proceeds in an entirely topochemical manner.

The changes to the unit cell parameters and the global structure observed by powder XRD are consistent with the results from DFT+U calculations. Figure V.3 furthermore illustrates the calculated local structural deformations deduced from DFT+U calculations upon the insertion of Li-ions within the ζ-V_2O_5 lattice. Video A.1 (supplemental files) shows the transformation pathway as deduced from Amplimodes, whereas Table A.1 lists key bond distances and bond angles of the unlithiated and fully lithiated phases. In the fully intercalated structure, the Li-ions are tetrahedrally coordinated to four oxygen atoms derived from vanadyl V=O bonds that protrude into the interstitial space of the 1D tunnels. As illustrated by Figure V.3, lithiation induces a substantial distortion of the O1—V1—O3 and O3—V2—O2 bond angles (from 105.9° in ζ-V_2O_5 to 102.2° and 101.2° in β'-$Li_{0.083}V_2O_5$) as a result of the electrostatic interactions between the Li-ions and oxygen atoms from the vanadyl species (Table A.1, Supporting Information). This interaction reduces the bond order of the vanadyl V=O bonds (V1—O1, V2—O2, and V3—O4 in Table A.1, Supporting Information), which are consistently elongated by 0.03—0.05Å with respect to the distances in pristine ζ-V_2O_5. The interaction of Li-ions with the anion sublattice is thus similar to the characteristic interaction of V=O moieties with Li-ions in layered α- and ε-$Li_xV_2O_5$ phases, as extensively studied *via* Raman and X-ray absorption spectroscopy, and is consistent with localized reduction of V^{5+} to V^{4+} (*vide infra*).[46,47,74]

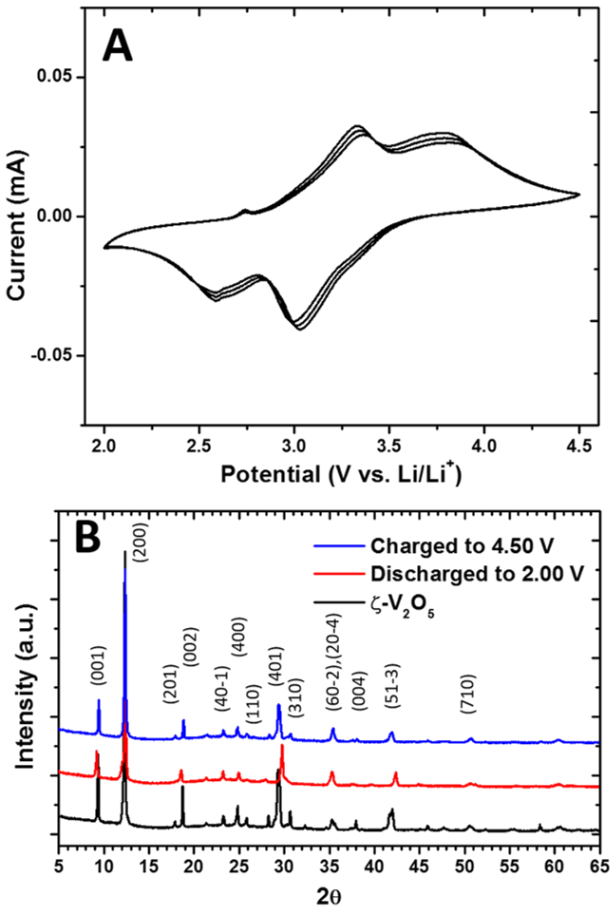

Figure V. 4: A) Cyclic voltammogram of ζ-V_2O_5 acquired in 1.0M LiTFSI in 1:1 DMC:EC at a scan rate of 0.5 mV/s; and B) XRD pattern of ζ-V_2O_5 nanowires after discharge to 2.00 V and charge to 4.50 V contrasted to the XRD pattern of the pristine ζ-V_2O_5 electrode.

To determine the electrochemical behavior of the ζ-phase V_2O_5 nanowires and to stabilize electrochemically lithiated structures, cyclic voltammetry has been performed on a thin film of ζ-V_2O_5 nanowires. Figure V.4a shows the measured cyclic voltammogram of the ζ-V_2O_5 nanowires between 2.00 and 4.50 V measured at a scan rate of 0.5 mV/s. In both the cathodic and anodic voltage sweeps, two distinctive peaks are identified, corresponding to the occupancy of the β and β′ sites, respectively. It is notable that based

on Figure V.2, the site occupancy is altered upon increasing lithiation but the 1D tunnel framework does not undergo a phase transformation such as observed in orthorhombic layered V_2O_5. The peak shapes of the intercalation and deintercalation cycles are similar, indicating good reversibility. The slight diminution of the peak current arises from the loss of connection of a fraction of the nanowires with the current collector since no binder or conductive filler has been used while preparing the electrode. Figure V.4B plots XRD patterns of electrochemically lithiated ζ-V_2O_5 charged to 4.5 V and discharged to 2.0 V. The patterns are similar to those depicted in Figure V.2B and corroborate that electrochemical Li-ion insertion proceeds without a large distortion of the framework as observed for chemical lithiation.

V.3.2. Electronic Structure of Lithiated ζ-V_2O_5

There is increasing realization that the electronic structure plays a paramount role in mediating cation diffusion and intercalation-induced structural distortions of cathode materials.[58,60,61,197,198,218] As noted above, in the layered orthorhombic phase of V_2O_5, Li-ion intercalation brings about localization of electron density in the split-off V $3d_{xy}$-derived conduction band, which results in stabilization of a small polaron.[45,47] The electronic structure implications of lithiation of ζ-V_2O_5 have not thus far been studied. XANES and X-ray photoemission spectroscopy serve as sensitive probes of electronic structure, specifically unoccupied/partially-occupied conduction band states and occupied valence band states, respectively.

V L-edge spectra correspond to transitions from the V 2*p* to unoccupied or partially occupied V 3*d* states, and are broadly separated into two main features split by ca. 7 eV

due to the spin-orbit coupling of the V 2*p* orbitals. The V L_{III}-edge at ca. 517 eV arises from the transition of V $2p_{3/2} \rightarrow 3d$ states, while the L_{II}-edge at ca. 524 eV arises from the V $2p_{1/2} \rightarrow 3d$ transition.[45,60,61,218] The L_{III}-edge exhibits features that arise due to the splitting of V $2p^5 3d^1$ excited states by crystal field and multiplet effects.[60] For the layered orthorhombic phase (figure V.5), there are two distinct features at 513.5 eV and 515 eV that correspond to excitations to the V $3d_{xy}$ and V $3d_{xz/yz}$ orbitals,[45,60,61] with the remainder of the 3*d* orbitals contributing to the main peak resonance at 517 eV. The V L_{II}-edge is rendered largely void of fine structure due to spectral broadening as the result of a Coster-Kronig Auger decay of the $2p_{1/2}$ to fill the $2p_{3/2}$ hole.

O K-edge spectra correspond to excitations from the O 1*s* core levels to O 2*p* states. The hybridization of V 3*d* orbitals with the O 2*p* orbitals splits this resonance into two states due to the crystal field splitting of the V 3*d* set. The first of these corresponds to hybridization of the O $2p_x$, $2p_y$, and $2p_z$ with the V 3*d* t_{2g} ($3d_{xy,}$ $3d_{xz,}$ and $3d_{yz}$) set at 529.5 eV via π interactions. The higher energy portion of the split resonance arises from σ interactions between the O 2*p* orbitals with the V 3*d* e_g set (531 eV), *via* hybridization of the O $2p_x$ and $2p_y$ with the V $3d_{x^2-y^2}$, and the O $2p_z$ orbital with the V $3d_{z^2}$. The modifications of these features as a result of the different structural and bonding motif in

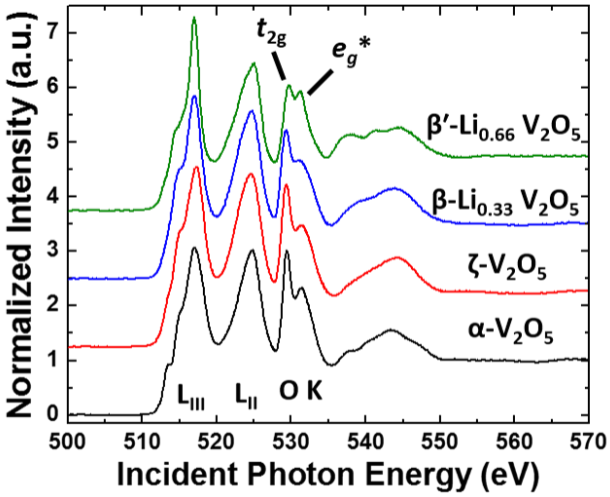

Figure V. 5: XANES spectra of layered α-V_2O_5, pristine ζ-V_2O_5, β-$Li_{0.33}V_2O_5$, and β'-$Li_{0.66}V_2O_5$.

the ζ-phase, and the changes incurred upon lithiation thus yield valuable insight into bonding and electronic structure.

Figure V.5 contrasts the V L-edge and O K-edge XANES spectra for the pristine ζ-phase and the layered orthorhombic phase of V_2O_5 and plots the evolution of the former upon chemical lithiation to nominal $Li_xV_2O_5$ stoichiometries of x = 0.33 and 0.66. The differences in the electronic structure of orthorhombic and ζ-V_2O_5 have been discussed in our previous work;[66] in ζ-V_2O_5, states derived from V $3d_{xy}$ orbitals are still situated at the bottom of the conduction band but since there are three different crystallographically inequivalent vanadium atoms and as a result of the relatively greater octahedral symmetry, these states are overlapped with the rest of the conduction band and the "split-off" character characteristic of orthorhombic V_2O_5 is no longer observed. These electronic structure changes are reflected in the absence of the well-resolved shoulder at ca. 513.5

eV in V L_{III}-edge spectra (corresponding to the transition to the V $3d_{xy}$ split-off conduction band observed in the spectra of orthorhombic V_2O_5) for ζ-V_2O_5 (Fig. V.5). With increasing Li-ion concentration, some distinct changes become apparent. At the V L_{III}-edge, there is a strong attenuation of the shoulder at 515 eV with respect to primary resonance at 517 eV, whereas the O K-edge shows a pronounced decrease in the ratio of t_{2g}:e_g* resonances (Fig. V.5). To fully understand the changes seen upon Li-ion insertion, a detailed investigation of the band structure of the ζ-phase, and its evolution upon lithiation is germane.

Figure V.6 plots the total density of states (DOS) as well as atom- and orbital-projected density of states (PDOS) of ζ-V_2O_5, ζ-V_2O_5 upon initial incorporation of Li-ions (x = 0.08), and the fully intercalated β'-$Li_{0.66}V_2O_5$ phase. In the pristine ζ-V_2O_5 phase, the Fermi level is situated just above the top of the valence band (Figure V.6A). The atom-projected PDOS plotted in Figure V.6B indicates considerably hybridization of V 3d and

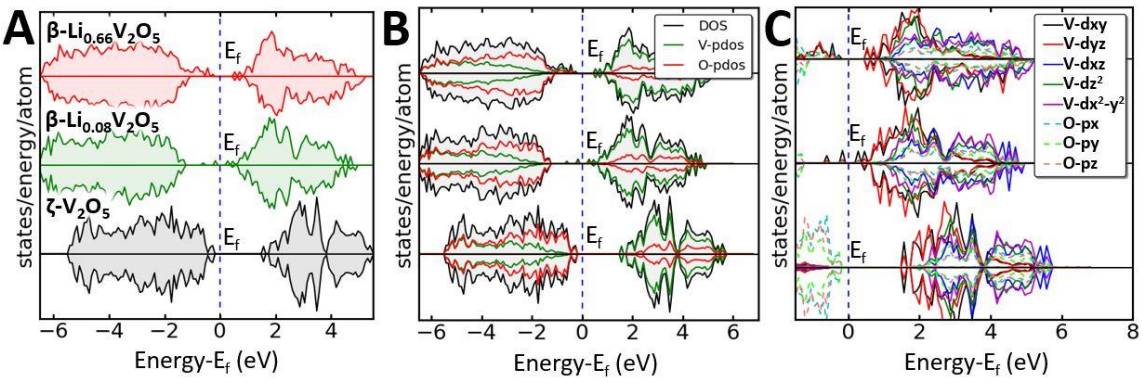

Figure V. 6: A) Total density of states, B) atom-projected density of states, C) vanadium orbital-projected density of states for pristine ζ-V_2O_5, β'-$Li_{0.08}V_2O_5$, and β'-$Li_{0.66}V_2O_5$ as calculated by DFT+U calculations.

O2p states. Figure V.6B indicates that the valence band is predominantly O2p in origin, whereas the conduction band is derived from V3d states. The conduction band can be roughly divided into two sets of states; the lower energy t_{2g} with contributions from V3d_{xy}, 3d_{xz}, and 3d_{yz} orbitals engaged in side-ways π-overlap with O2p orbitals and the higher energy e_g* states with contributions from V3d_{z2} and 3d_{x2-y2} orbitals engaged in end-on σ-overlap with O2p orbitals (Fig. V.6C). As a result of significant distortion of the vanadium coordination environment away from perfectly octahedral, there is a distinct splitting of the t_{2g} orbitals into non-degenerate states. In contrast to the square-pyramidal vanadium coordination of orthorhombic V_2O_5, which yields a distinctive V 3d_{xy} split-off conduction band, the distinct mix of five- and six-coordinated vanadium centers in the ζ-phase leads to a combination of the V3d_{xy} and 3d_{yz} orbitals comprising the lowest energy states at the bottom of the conduction band (Figure V.6C). Upon initial intercalation of Li-ions, corresponding to a stoichiometry of β′-$Li_{0.08}V_2O_5$, a filled mid-gap state appears adjacent to the Fermi level (Figure V.6). As depicted in Figures V.6B and 6C, these filled mid-gap states comprise V 3d_{xy} and 3d_{yz} states hybridized with O 2p_y states. This indicates that as the vanadium centers are reduced upon the insertion of Li-ions, the approximately degenerate V 3d_{xy} and V 3d_{yz} bands that comprise the lowest lying states of the conduction band are filled and shift just below the Fermi level. Increasing the Li-ion concentration to the stoichiometric limit (x = 0.66), leads to the appearance of additional states just below the Fermi level. The increase in Li-ion concentration leads to further distortion of the vanadium symmetry away from octahedral and thereby further increases the splitting of the t_{2g} states (Figure V.6C). In addition, as a greater proportion of vanadium centers are

reduced by the incorporated interstitial Li-ions, these filled V $3d^1$ states are shifted from the conduction band to the mid-gap region.

In the XANES measurements shown in Figure V.5, it is apparent that lithiation of ζ-V_2O_5 brings about a sharp attenuation of the low-energy shoulder at the V L_{III}-edge. These resonances correspond to transitions to final states at the bottom of the conduction band that are predominantly V $3d_{xy}$ and $3d_{yz}$ in origin as discussed above. With increasing Li-ion intercalation, there is a strong suppression of the absorption (Pauli blocking) associated with these states as these states become filled. Indeed, consistent with this assignment, the V $2p_{3/2}$ XPS spectrum shown in Figure A.5 shows the pronounced appearance of a low-energy shoulder corresponding to tetravalent vanadium for β'-$Li_{0.66}V_2O_5$. This filling of the V $3d_{xy}$ and $3d_{yz}$ orbitals is also reflected in the changes at the O K-edge; the intensity of the resonance associated with the hybridization of the O 2p orbitals with the t_{2g} set of the V 3d centered at 529 eV is reduced relative to the resonance associated with the e_g* antibonding orbitals centered at 531 eV (Figure V.5). The structural distortion associated with lithiation, which reduces the degeneracy of the t_{2g} states (Fig. V.6C), as well as the removal of degeneracy majority and minority spin states upon vanadium reduction (in analogy with previous observations for orthorhombic V_2O_5)[45] likely further contribute to the substantial alteration of intensity ratios observed upon lithiation. Consistent with the above picture wherein lowest-lying V $3d_{xy}$ and $3d_{yz}$ states are filled upon intercalation and the filled states appear in the mid-gap region (Fig. V.6), hard X-ray photoelectron spectroscopy (HAXPES) measurements depicted in Figure A.5A indicate the appearance of filled bands ca. 0.1 eV below the Fermi level (inset).

These states are not observed for unlithiated V_2O_5 and their distinct emergence upon lithiation verifies the appearance of new states predicted by the DFT+U calculations.

V.3.3. Polaron Formation and Barriers to Li-ion Diffusion

In layered orthorhombic V_2O_5, the insertion of a Li-ion leads to the formation of a small polaron that significantly impedes diffusivity through the host lattice; such quasiparticles are also stabilized upon lithiation of α-MoO_3.[45,47,244] In order to examine polaron formation upon lithiation of the ζ-phase of V_2O_5, the charge density difference has been computed for the lithiated and unlithiated structures as per:

$$\Delta\rho_{total} = \rho(Li_xV_2O_5) - \rho(V_2O_5) - \rho(x\text{Li}) \qquad \ldots(1)$$

where $\Delta\rho_{total}$ is the total change in charge density, $\rho(Li_xV_2O_5)$ is the charge density of a lithium-ion-intercalated ζ-V_2O_5 supercell, $\rho(V_2O_5)$ is the charge density of ζ-V_2O_5 with the same structural parameters as in the lithiated system, and $\rho(x\text{Li})$ is the charge density of lithium atoms arrayed at the same distances as in the intercalated system. The charge density differential maps allow for visualization of localized electron density. The yellow isosurface plots in Figure V.7A depict the regions wherein the electron density has increased for β'-$Li_{0.08}V_2O_5$ relative to the pristine structure, and corresponds to electron density localized within the t_{2g} states derived from V 3d orbitals. The localized electron density corresponds to reduction of V^{5+} centers to V^{4+}. States derived from V $3d_{xy}$ and V $3d_{yz}$ orbitals are degenerate in this structure (Fig. V.6) and thus electron localization can occur in either state (Figure V.7A), which is in stark contrast to lithiation of α-V_2O_5, where electron localization occurs specifically within the V $3d_{xy}$-derived "split-off" conduction band.[45] A concurrent decrease of charge density is seen along the V–O bonds of the [VO_5]

units, as depicted by the blue isosurface plot in Figure V.7B, which reflects a decrease in bond strength as a result of reduction of the vanadium center. The localization of charge in V $3d_{xy/yz}$ brings about a pronounced distortion of the local geometry that is further amplified by the electrostatic interactions between the intercalated Li-ion and the oxygen atoms pointing inwards and defining its immediate coordination environment. The isosurface plot for the mid-gap state that is formed slightly above the valence band (Fig. V.6) is plotted in Figure V.7C. The contours of charge density depicted in Figure V.7C suggest that this state is derived from V $3d_{xy}$ orbitals hybridized with O $2p_x$ and O $2p_y$ states derived from the vanadyl oxygens. It is noteworthy that the mid-gap states formed upon Li-ion intercalation are not pinned to the O 2p states of the valence band (Fig. A.5B), such pinning would have effectively trapped the polaron, and thus the associated Li-ion.[67]

Figure A.6 (Supporting Information) plots similar charge density difference maps for a ζ-V_2O_5 supercell reduced by a single electron (*sans* the Li-ion). Similar localization of electron density in V t_{2g}-derived states is observed as noted for β'-$Li_{0.08}V_2O_5$; this localization further induces distortion of the local geometry as evidenced by the polarization of V−O bonds and decrease of charge density plotted in Figure A.6B. Figure A.7 indicates the spin polarized density of states calculated for this structure suggesting a lifting of spin degeneracy upon reduction. The splitting of the spin channels stabilizes the system and the energetic gain derived from preferential occupation of a single spin channel is sufficient to counteract the energy expended to distort the lattice around the localized electron. The localization of electron density induces magnetic character as a result of the lifting of spin degeneracy. Figure A.8 indicates that enforcing spin degeneracy within this

system, which results in delocalization of electron density across the vanadium centers, comes at an energetic cost of ca. -360 meV/V_2O_5 formula unit. To put this number in perspective, the corresponding polaron formation energy in the layered orthorhombic-phase of V_2O_5 is -410 meV/V_2O_5 formula unit;[45] the degeneracy of states at the bottom of the conduction band thus destabilizes polaron formation and electron localization by almost 50 meV in the ζ-phase.

From the perspective of Li-ion diffusion, we have further computed the polaron diffusion barrier by examining the energy difference between the configurations shown in Figure V.8 corresponding to diffusion of the polaron from the site labeled from V1 to V2 (the Li-ion remains immobile). As shown in Figure V.8B, the polaron diffusion barrier is computed to be 240 meV, which is substantially lower than the 340 meV polaron migration barrier deduced for orthorhombic V_2O_5; the lower diffusion barrier is expected to yield much more facile Li-ion diffusion in the ζ-phase. Considering the diffusion of just the Li-ion (without the polaron), a relatively small diffusion barrier of 130 eV was predicted for the ζ-phase as a result of small changes in coordination number (5→3→4→3→5 as it diffuses between β sites across a β′ site);[233] the corresponding value for orthorhombic V_2O_5 is 220 meV largely as a result of the large coordination changes (8→3→8) required along the coordinate diffusion path.[45] Supplementary Video A.2 depicts the coupled motion of the polaron as well as the Li-ions through the tunnels of the 1D ζ-V_2O_5 phase.

Figure V.9 plots scanning transmission X-ray microscopy data acquired for several β'-$Li_xV_2O_5$ nanowires with a nominal stoichiometry of x = 0.33. Integrated V L-edge and

O K-edge spectra acquired across different regions are plotted in Figure V.9B. The observed spectral transitions have the same assignments as in Figure V.5; the improved spectral resolution derives from the imaging of individual single-crystalline nanowires as compared to ensemble measurements of powders in Figure V.5. The spectral components measured across different areas of the sample are remarkably homogeneous, suggesting uniform lithiation of the nanowires (as also suggested by the powder XRD measurements in Figure V.2). Notably, the ratio of the shoulder at 15.8 eV to the primary V L_{III} absorption and the ratio of the t_{2g}:/e_g* intensities at the O K-edge remains constant across the three nanowires. The observed homogeneity is in stark contrast to sharp lithiation gradients visualized within nanowires and across networks of nanowires in orthorhombic V_2O_5 as[45,47] well as other cathode materials such as $LiFePO_4$.[46]

V.4 Conclusion

In summary, the 1D tunnels of the metastable ζ-V_2O_5 phase accommodate Li-ions with only modest structural distortion and without a substantial transformation of the framework. As compared to the thermodynamically stable orthorhombic phase of V_2O_5, in ζ-V_2O_5, (i) polaron formation is thermodynamically less favorable by almost 50 meV and (ii) the polaron diffusion barrier is more than 100 meV lower. The increased covalency of the ζ-V_2O_5 structure allows for a more delocalized polaron relative to the orthorhombic structure with greater degeneracy of V 3d states at the bottom of the conduction band in contrast to the "split-off" conduction band observed for orthorhombic V_2O_5. The increased rigidity of the 1D tunnels minimizes the ability of the lattice to deform around the localized electron.

Additionally, the mid-gap states formed upon Li-ion insertion are not pinned to the O 2p orbitals of the valence band. Facile single-phase lithiation is observed and STXM measurements indicate homogeneous lithiation across the nanowires again in sharp contrast to lithiation gradients and domains observed in many cathode materials. The results underscore the interplay between geometric and electronic structure in intercalation hosts and emphasize approaches for mitigating diffusion limitations and phase-transformation-induced energy dissipation through identification of appropriate structural frameworks with appropriate splitting of transition-metal d-orbital-derived states.

CHAPTER VI

CONCLUSION

In this dissertation, the properties of vanadium oxide nanomaterials across phase transitions were explored, with implications for thermochromic glazings, and cation storage. Chapter II discusses the development of a novel synthetic route to free standing nanowires of undoped VO_2. This step-wise hydrothermal reduction is a process that is scalable up to multigram scales, and produces VO_2 nanowires that exhibit MIT properties that are on par with the best performing materials that are synthesized by vapor deposition processes. These nanowires exhibit an almost 4 order of magnitude change in resistivity within 0.1°C across the MIT. DSC indicates that there is relatively low hysteresis, which is corroborated by Raman spectroscopy, which shows that the heating and cooling transitions occur at the same temperature at the time scale of that measurement.

Beginning the exploration of V_2O_5 as a cathode material for Li-ion batteries, Chapter III investigates the effect of size on the kinetics of lithium uptake, and modulation of phase stabilities and formation of phase inhomogeneities as an effect of particle size. Three different sizes of particles were explored, ranging from bulk particles with dimensions on the order of several microns, hydrothermally grown nanowires with lateral dimensions of ca. 180 nm, and CVD grown platelets with dimensions of ca. 80 nm. We find that there is a significant acceleration of Li-ion insertion for the smallest particles, with the CVD grown platelets taking up lithium the most quickly, progressing to ca. x = 1.0 within one hour of lithiation. The hydrothermally grown nanowires, in turn, take up lithium more slowly than the CVD grown platelets, but still significantly faster than the

bulk sized particles, wherein a mixture of the α- and ε-phases in equal proportion are seen after 2 h of lithiation. The bulk particles lag behind, showing only the earliest stages of nucleation of the ε-phase after 2 h. Additionally it is found that at the size regime of the CVD grown platelets, there is no presence of the phase mixtures seen for the larger particles, indicating that there is a critical size below which lithiation proceeds homogeneously.

In Chapter IV, the mecahnisms by which Li-ions insert into V_2O_5 at low overpotentials is investigated by using XANES spectroscopy at the V K-edge to explore the effects of lithiation on the geometric and electronic structures. The presence of isosbestic points in the XANES spectra led to the application of PCA and MCR to statistically deconvolute the spectra to investigate the formation of phase mixtures, and more broadly, the phase progression as a function of Li-ion concentration for these wires. We find that the barrier that arises due to the formation of small polarons upon Li-ion insertion slow the diffusion of Li-ions through the host structure. Due to this roadblock slowing the bulk diffusion of Li-ion to a rate slower than insertion at the nanowire surfaces, there is a supersaturation of Li-ions near particle surfaces that leads to the nucleation of a high lithium ε- or δ-phase. The detailed structural progression is as follows: initial Li-ion insertion homogeneously forms the low-lithium α-phase; beyond $x = 0.1$ Li/V_2O_5 the high lithium ε- or δ-phase nucleates at nanowire surfaces, and upon further lithiation, the high lithium phase grows at the expense of the low lithium phase.

Chapter V builds upon the discovery of the polaronic barrier to Li-ion diffusion in the single layered V_2O_5 structure. In this chapter we identify a novel polymorph of V_2O_5

that serves to minimize this polaronic barrier. Due to the distinctly different vanadium coordination environments in this 1D-tunnel phase the non-degeneracy of the V $3d_{xy}$ orbital in the single layered phases is eliminated, blending at the conduction band bottom with the other orbitals of the t_{2g} set. This degeneracy leads to the formation of a more delocalized, less distorted, and thus weaker polaron. Additionally the modified bonding of the Li-ions in the interstitial tunnel site leads to a significant lowering of coordination frustration along the Li-ion diffusion path.

In the future, we plan to study Li-ion transport at the mesoscale for the single layered phase of V_2O_5 using STXM in order to gain further insight into Li-ion diffusion mechanisms beyond the atomistic and single particle regimes. These measurements will allow for the formulation of design rules for electrode architectures for these materials. With the ζ-phase, we plan to investigate the insertion and diffusion of multivalent cations. A subject of intense research interest due to concerns of lithium criticality and safety, cations such as magnesium offer the promise of very high energy density batteries utilizing metallic electrodes that are impossible for Li-ion batteries due to dendrite formation. However, there are only ca. 5 known materials that are able to reversibly intercalate Mg-ions, none of which are capable of operation at potentials > 3V. DFT calculations of Mg-ion insertion into the ζ-phase indicate that room temperature Mg-ion insertion and cell voltages in excess of 3V should be achieveable. Should facile Mg-ion insertion be realized, it would serve as an illustration of the power of understanding cation insertion and diffusion mechanisms in informing rational cathode design.

REFERENCES

(1) Galy, J. Vanadium Pentoxide and Vanadium Oxide Bronzes-Structral Chemistry of Single (S) and Double (D) Layer $M_xV_2O_5$ Phases. *J. Solid State Chem.* **1992**, *100*, 229–245.

(2) Marley, P. M.; Abtew, T. A.; Farley, K. E.; Horrocks, G. A.; Dennis, R. V.; Zhang, P.; Banerjee, S. Emptying and Filling a Tunnel Bronze. *Chem. Sci.* **2015**, *6*, 1712–1718.

(3) Chernova, N. A.; Roppolo, M.; Dillon, A. C.; Whittingham, M. S. Layered Vanadium and Molybdenum Oxides: Batteries and Electrochromics. *J. Mater. Chem.* **2009**, *19*, 2526–2552.

(4) Whittaker, L.; Patridge, C. J.; Banerjee, S. Microscopic and Nanoscale Perspective of the Metal-Insulator Phase Transitions of VO_2: Some New Twists to an Old Tale. *J. Phys. Chem. Lett.* **2011**, *2*, 745–758.

(5) Marley, P. M.; Horrocks, G. A.; Pelcher, K. E.; Banerjee, S. Transformers : The Changing Phases of Low-Dimensional Vanadium Oxide Bronzes. *Chem. Commun.* **2015**, *51*, 5181–5198.

(6) Whittingham, M. S. Lithium Batteries and Cathode Materials. *Chem. Rev.* **2004**, *104*, 4271–4302.

(7) Zavalij, P. Y.; Whittingham, M. S. Structural Chemistry of Vanadium Oxides with Open Frameworks. *Acta Crystallogr.* **1999**, *B55*, 627–663.

(8) Marley, P. M.; Banerjee, S. Reversible Interconversion of a Divalent Vanadium Bronze between δ and β Quasi-1D Structures. *Inorg. Chem.* **2012**, *51*, 5264–5269.

(9) Ueda, Y.; Isobe, M.; Yamauchi, T. Superconductivity under High Pressure in β(β′)-Vanadium Bronzes. *J. Phys. Chem. Solids* **2002**, *63*, 951–955.

(10) Morin, F. J. Oxides Which Show a Metal-Insulator Transition at the Neel Temperature. *Phys. Rev. Lett.* **1959**, *3*, 2–4.

(11) Qazilbash, M. M.; Brehm, M.; Chae, B.-G.; Ho, P.-C.; Andreev, G. O.; Kim, B.-J.; Yun, S. J.; Balatsky, A. V; Maple, M. B.; Keilmann, F.; et al. Mott Transition in VO_2 Revealsed by Infrared Spectroscopy and Nano-Imaging. *Science* **2007**, *318*, 1750–1753.

(12) Qazilbash, M. M.; Tripathi, A.; Schafgans, A. A.; Kim, B.-J.; Kim, H.-T.; Cai, Z.; Holt, M. V.; Maser, J. M.; Keilmann, F.; Shpyrko, O. G.; et al. Nanoscale Imaging of the Electronic and Structural Transitions in Vanadium Dioxide. *Phys. Rev. B* **2011**, *83*, 165108.

(13) Wei, J.; Wang, Z.; Chen, W.; Cobden, D. H. New Aspects of the Metal – Insulator Transition in Single-Domain Vanadium Dioxide Nanobeams. *Nat. Nanotechnol.* **2009**, *4*, 420–424.

(14) Eyert, V. VO_2: A Novel View from Band Theory. *Phys. Rev. Lett.* **2011**, *107*, 2–5.

(15) Tao, Z.; Han, T.-R. T.; Mahanti, S. D.; Duxbury, P. M.; Yuan, F.; Ruan, C.-Y.; Wang, K.; Wu, J. Decoupling of Structural and Electronic Phase Transitions in VO_2. *Phys. Rev. Lett.* **2012**, *109*, 166406.

(16) van Veenendaal, M. Ultrafast Photoinduced Insulator-to-Metal Transitions in Vanadium Dioxide. *Phys. Rev. B* **2013**, *87*, 235118.

(17) Manning, T. D.; Parkin, I. P.; Clark, R. J. H.; Sheel, D.; Pemble, M. E.; Vernadou,

D. Intelligent Window Coatings: Atmospheric Pressure Chemical Vapour Deposition of Vanadium Oxides. *J. Mater. Chem.* **2002**, *12*, 2936–2939.

(18) Goodenough, J. B. Two Components of the Crystallographic Transition in VO_2. *J. Solid State Chem.* **1971**, *3*, 490–500.

(19) Patridge, C. J.; Whittaker, L.; Ravel, B.; Banerjee, S. Elucidating the Influence of Local Structure Perturbations on the Metal−Insulator Transitions of $V_{1-x}Mo_xO_2$ Nanowires: Mechanistic Insights from an X-Ray Absorption Spectroscopy Study. *J. Phys. Chem. C* **2012**, *116*, 3728–3736.

(20) Whittaker, L.; Wu, T.-L.; Patridge, C. J.; Sambandamurthy, G.; Banerjee, S. Distinctive Finite Size Effects on the Phase Diagram and Metal–insulator Transitions of Tungsten-Doped Vanadium(IV) Oxide. *J. Mater. Chem.* **2011**, *21*, 5580.

(21) Zhang, J.; He, H.; Xie, Y.; Pan, B. Theoretical Study on the Tungsten-Induced Reduction of Transition Temperature and the Degradation of Optical Properties for VO_2. *J. Chem. Phys.* **2013**, *138*, 114705.

(22) Lee, S.; Cheng, C.; Guo, H.; Hippalgaonkar, K.; Wang, K.; Suh, J.; Liu, K.; Wu, J. Axially Engineered Metal-Insulator Phase Transition by Graded Doping VO_2 Nanowires. *J. Am. Chem. Soc.* **2013**, *135*, 4850–4855.

(23) Dai, L.; Chen, S.; Liu, J.; Gao, Y.; Zhou, J.; Chen, Z.; Cao, C.; Luo, H.; Kanehira, M. F-Doped VO_2 Nanoparticles for Thermochromic Energy-Saving Foils with Modified Color and Enhanced Solar-Heat Shielding Ability. *Phys. Chem. Chem. Phys.* **2013**, *15*, 11723–11729.

(24) Burkhardt, W.; Christmann, T.; Meyer, B. K.; Niessner, W.; Schalch, D.; Scharmann, A. W- and F-Doped VO_2 Films Studied by Photoelectron Spectrometry. *Thin Solid Films* **1999**, *345*, 229–235.

(25) Ren, Q.; Wan, J.; Gao, Y. Theoretical Study of Electronic Properties of X-Doped (X = F , Cl , Br , I) VO_2 Nanoparticles for Thermochromic Energy-Saving Foils. *J. Phys. Chem. A* **2014**, *118*, 11114–11118.

(26) Guiton, B. S.; Gu, Q.; Prieto, A. L.; Gudiksen, M. S.; Park, H. Single-Crystalline Vanadium Dioxide Nanowires with Rectangular Cross Sections. *J. Am. Chem. Soc.* **2005**, *127*, 498–499.

(27) Jones, A. C.; Berweger, S.; Wei, J.; Cobden, D.; Raschke, M. B. Nano-Optical Investigations of the Metal-Insulator Phase Behavior of Individual VO_2 Microcrystals. *Nano Lett.* **2010**, *10*, 1574–1581.

(28) Wu, J.; Gu, Q.; Guiton, B. S.; Leon, N. P. De; Ouyang, L.; Park, H. Strain-Induced Self Organization of Metal − Insulator Domains in Single-Crystalline VO_2 Nanobeams. *Nano Lett.* **2006**, *6*, 2313–2317.

(29) Whittaker, L.; Jaye, C.; Fu, Z.; Fischer, D. A.; Banerjee, S. Depressed Phase Transition in Solution-Grown VO_2 Nanostructures. *J. Am. Chem. Soc.* **2009**, *131*, 8884–8894.

(30) Corr, S. A.; Grossman, M.; Furman, J. D.; Melot, B. C.; Cheetham, A. K.; Heier, K. R.; Seshadri, R. Controlled Reduction of Vanadium Oxide Nanoscrolls: Crystal Structure, Morphology, and Electrical Properties. *Chem. Mater.* **2008**, *20*, 6396–6404.

(31) Liu, J.; Li, Q.; Wang, T.; Yu, D.; Li, Y. Metastable Vanadium Dioxide Nanobelts: Hydrothermal Synthesis, Electrical Transport, and Magnetic Properties. *Angew. Chem. Int. Ed. Engl.* **2004**, *43*, 5048–5052.

(32) Whittaker, L.; Zhang, H.; Banerjee, S. VO_2 Nanosheets Exhibiting a Well-Defined Metal–insulator Phase Transition. *J. Mater. Chem.* **2009**, *19*, 2968.

(33) Wu, T.-L.; Whittaker, L.; Banerjee, S.; Sambandamurthy, G. Temperature and Voltage Driven Tunable Metal-Insulator Transition in Individual $W_xV_{1-x}O_2$ Nanowires. *Phys. Rev. B* **2011**, *83*, 73101.

(34) Griffiths, C. H. Influence of Stoichiometry on the Metal-Semiconductor Transition in Vanadium Dioxide. *J. Appl. Phys.* **1974**, *45*, 2201.

(35) Ruzmetov, D.; Zawilski, K. T.; Narayanamurti, V.; Ramanathan, S. Structure-Functional Property Relationships in Rf-Sputtered Vanadium Dioxide Thin Films. *J. Appl. Phys.* **2007**, *102*, 113715.

(36) Narayan, J.; Bhosle, V. M. Phase Transition and Critical Issues in Structure-Property Correlations of Vanadium Oxide. *J. Appl. Phys.* **2006**, *100*, 103524.

(37) Horrocks, G. A.; Singh, S.; Likely, M. F.; Sambandamurthy, G.; Banerjee, S. Scalable Hydrothermal Synthesis of Free-Standing VO_2 Nanowires in the M1 Phase. *ACS Appl. Mater. Interfaces* **2014**, *6*, 15726–15732.

(38) Li, S.-Y.; Niklasson, G. A.; Granqvist, C. G. Nanothermochromics : Calculations for Nanoparticles in Dielectric Hosts Show Much Improved Luminous Transmittance and Solar Energy Transmittance Modulation. *J. Appl. Phys.* **2010**, *108*, 63525.

(39) Goodenough, J. B.; Park, K.-S. The Li-Ion Rechargeable Battery : A Perspective. *J. Am. Chem. Soc.* **2013**, *135*, 1167–1176.

(40) Orvananos, B.; Ferguson, T. R.; Yu, H.-C.; Bazant, M. Z.; Thornton, K. Particle-Level Modeling of the Charge-Discharge Behavior of Nanoparticulate Phase-Separating Li-Ion Battery Electrodes. *J. Electrochem. Soc.* **2014**, *161*, A535–A546.

(41) Chueh, W. C.; Gabaly, F. El; Sugar, J. D.; Bartelt, N. C.; McDaniel, A. H.; Fenton, K. R.; Zavadil, K. R.; Tyliszczak, T.; Lai, W.; McCarty, K. F. Intercalation Pathway in Many-Particle $LiFePO_4$ Electrode Revealed by Nanoscale State-of-Charge Mapping. *Nano Lett.* **2013**, *13*, 866–872.

(42) Guo, Y.; Smith, R. B.; Yu, Z.; Efetov, D. K.; Wang, J.; Kim, P.; Bazant, M. Z.; Brus, L. E. Li Intercalation into Graphite: Direct Optical Imaging and Cahn-Hilliard Reaction Dynamics. *J. Phys. Chem. Lett.* **2016**, *7*, 2151–2156.

(43) Ghassemi, H.; Au, M.; Chen, N.; Heiden, P. A; Yassar, R. S. In Situ Electrochemical Lithiation/Delithiation Observation of Individual Amorphous Si Nanorods. *ACS Nano* **2011**, *10*, 7805–7811.

(44) Yang, F.; Liu, Y.; Martha, S. K.; Wu, Z.; Andrews, J. C.; Ice, G. E.; Pianetta, P.; Nanda, J. Nanoscale Morphological and Chemical Changes of High Voltage Lithium-Manganese Rich NMC Composite Cathodes with Cycling. *Nano Lett.* **2014**, *14*, 4334–4341.

(45) De Jesus, L. R.; Horrocks, G. A.; Liang, Y.; Parija, A.; Jaye, C.; Wangoh, L.; Wang, J.; Fischer, D. A.; Piper, L. F. J.; Prendergast, D.; et al. Mapping Polaronic States and Lithiation Gradients in Individual V_2O_5 Nanowires. *Nat. Commun.* **2016**, *7*,

12022.

(46) Lim, J.; Li, Y.; Alsem, D. H.; So, H.; Lee, S. C.; Bai, P.; Cogswell, D. A.; Liu, X.; Jin, N.; Yu, Y.; et al. Origin and Hysteresis of Lithium Compositional Spatiodynamics within Battery Primary Particles. *Science* **2016**, *353*, 566–571.

(47) Horrocks, G. A.; Braham, E. J.; Liang, Y.; De Jesus, L. R.; Jude, J.; Velázquez, J. M.; Prendergast, D.; Banerjee, S. Vanadium K-Edge X-Ray Absorption Spectroscopy as a Probe of the Heterogeneous Lithiation of V_2O_5: First-Principles Modeling and Principal Component Analysis. *J. Phys. Chem. C* **2016**, *120*, 23922–23932.

(48) Horrocks, G. A.; Likely, M. F.; Velazquez, J. M.; Banerjee, S. Finite Size Effects on the Structural Progression Induced by Lithiation of V_2O_5: A Combined Diffraction and Raman Spectroscopy Study. *J. Mater. Chem. A* **2013**, *1*, 15265–15277.

(49) Stein, P.; Zhao, Y.; Xu, B.-X. Effects of Surface Tension and Electrochemical Reactions in Li-Ion Battery Electrode Nanoparticles. *J. Power Sources* **2016**, *332*, 154–169.

(50) Hitchcock, A. P. Soft X-Ray Spectromicroscopy and Ptychography. *J. Electron Spectros. Relat. Phenomena* **2015**, *200*, 49–63.

(51) Whittingham, M. S. The Role of Ternary Phases in Cathode Reactions. *J. Electrochem. Soc.* **1976**, *123*, 315.

(52) Delmas, C.; Maccario, M.; Croguennec, L.; Le Cras, F.; Weill, F. Lithium Deintercalation in $LiFePO_4$ Nanoparticles via a Domino-Cascade Model. *Nat*

Mater **2008**, *7*, 665–671.

(53) Liu, H.; Strobridge, F. C.; Borkiewicz, O. J.; Wiaderek, K. M.; Chapman, K. W.; Chupas, P. J.; Grey, C. P. Capturing Metastable Structures during High-Rate Cycling of $LiFePO_4$ Nanoparticle Electrodes. *Science* **2014**, *344*, 1451–1452.

(54) Brunetti, G.; Robert, D.; Bayle-Guillemaud, P.; Rouvière, J. L.; Rauch, E. F.; Martin, J. F.; Colin, J. F.; Bertin, F.; Cayron, C. Confirmation of the Domino-Cascade Model by $LiFePO_4/FePO_4$ Precession Electron Diffraction. *Chem. Mater.* **2011**, *23*, 4515–4524.

(55) Schultz, B. J.; Dennis, R. V; Lee, V.; Banerjee, S. An Electronic Structure Perspective of Graphene Interfaces. *Nanoscale* **2014**, *6*, 3444–3466.

(56) Liang, Y.; Vinson, J.; Pemmeraju, S.; Drisdell, W. S.; Shirley, E. L.; Prendergast, D. Accurate X-Ray Absorption Predictions: An Advanced Self-Consistent-Field Approach Inspired by Many-Body Perturbation Theory. *Phys. Rev. Lett.* **2017**, *118*, 96402.

(57) McBreen, J. The Application of Synchrotron Techniques to the Study of Lithium-Ion Batteries. *J. Solid State Electrochem.* **2009**, *13*, 1051–1061.

(58) Patridge, C. J.; Jaye, C.; Abtew, T. A.; Ravel, B.; Fischer, D. A.; Marschilok, A. C.; Zhang, P.; Takeuchi, K. J.; Takeuchi, E. S.; Banerjee, S. An X-Ray Absorption Spectroscopy Study of the Cathodic Discharge of $Ag_2VO_2PO_4$: Geometric and Electronic Structure Characterization of Intermediate Phases and Mechanistic Insights. *J. Phys. Chem. C* **2011**, *115*, 14437–14447.

(59) Chaurand, P.; Rose, J.; Briois, V.; Salome, M.; Proux, O.; Nassif, V.; Olivi, L.;

Susini, J.; Hazemann, J.-L.; Bottero, J.-Y. New Methodological Approach for the Vanadium K-Edge X-Ray Absorption Near-Edge Structure Interpretation: Application to the Speciation of Vanadium in Oxide Phases from Steel Slag. *J. Phys. Chem. B* **2007**, *111*, 5101–5110.

(60) Maganas, D.; Roemelt, M.; Hävecker, M.; Trunschke, A.; Knop-Gericke, A.; Schlögl, R.; Neese, F. First Principles Calculations of the Structure and V L-Edge X-Ray Absorption Spectra of V_2O_5 Using Local Pair Natural Orbital Coupled Cluster Theory and Spin-Orbit Coupled Configuration Interaction Approaches. *Phys. Chem. Chem. Phys.* **2013**, *15*, 7260–7276.

(61) Velazquez, J. M.; Jaye, C.; Fischer, D. A.; Banerjee, S. Near Edge X-Ray Absorption Fine Structure Spectroscopy Studies of Single-Crystalline V_2O_5 Nanowire Arrays. *J. Phys. Chem. C* **2009**, *113*, 7639–7645.

(62) Ikeno, H.; de Groot, F. M. F.; Stavitski, E.; Tanaka, I. Multiplet Calculations of $L_{2,3}$ X-Ray Absorption near-Edge Structures for 3d Transition-Metal Compounds. *J. Phys. Condens. Matter* **2009**, *21*, 104208.

(63) Ade, H.; Hitchcock, A. P. NEXAFS Microscopy and Resonant Scattering: Composition and Orientation Probed in Real and Reciprocal Space. *Polymer* **2008**, *49*, 643–675.

(64) Thibault, P.; Dierolf, M.; Menzel, A.; Bunk, O.; David, C.; Pfeiffer, F. High-Resolution Scanning X-Ray Diffraction Microscopy. *Science* **2008**, *321*, 379–382.

(65) Lerotic, M.; Jacobsen, C.; Schäfer, T.; Vogt, S. Cluster Analysis of Soft X-Ray Spectromicroscopy Data. *Ultramicroscopy* **2004**, *100*, 35–57.

(66) Tolhurst, T. M.; Leedahl, B.; Andrews, J. L.; Marley, P. M.; Banerjee, S.; Moewes, A. Contrasting 1D Tunnel-Structured and 2D Layered Polymorphs of V_2O_5: Relating Crystal Structure and Bonding to Band Gaps and Electronic Structure. *Phys. Chem. Chem. Phys.* **2016**, *18*, 15798–15806.

(67) Lin, Y.-C.; Wen, B.; Wiaderek, K. M.; Sallis, S.; Liu, H.; Lapidus, S. H.; Borkiewicz, O. J.; Quackenbush, N. F.; Chernova, N. A.; Karki, K.; et al. Thermodynamics, Kinetics and Structural Evolution of ε-$LiVOPO_4$ over Multiple Lithium Intercalation. *Chem Mater* **2016**, *28*, 1794–1805.

(68) Wang, D.; Zuin, L. Li K-Edge X-Ray Absorption near Edge Structure Spectra for a Library of Lithium Compounds Applied in Lithium Batteries. *J. Power Sources* **2017**, *337*, 100–109.

(69) Patridge, C. J.; Wu, T.-L.; Jaye, C.; Ravel, B.; Takeuchi, E. S.; Fischer, D. A.; Sambandamurthy, G.; Banerjee, S. Synthesis, Spectroscopic Characterization, and Observation of Massive Metal-Insulator Transitions in Nanowires of a Nonstoichiometric Vanadium Oxide Bronze. *Nano Lett.* **2010**, 2448–2453.

(70) Chan, C. K.; Peng, H.; Liu, G.; McIlwrath, K.; Zhang, X. F.; Huggins, R. A.; Cui, Y. High-Performance Lithium Battery Anodes Using Silicon Nanowires. *Nat. Nanotechnol.* **2008**, *3*, 31–35.

(71) Chan, C. K.; Peng, H.; Twesten, R. D.; Jarausch, K.; Zhang, X. F.; Cui, Y. Fast, Completely Reversible Li Insertion in Vanadium Pentoxide Nanoribbons. *Nano Lett.* **2007**, *7*, 490–495.

(72) Whittingham, M. S. Inorganic Nanomaterials for Batteries. *Dalt. Trans.* **2008**, No.

40, 5424–5431.

(73) Aricò, A. S.; Bruce, P.; Scrosati, B.; Tarascon, J.-M.; van Schalkwijk, W. Nanostructured Materials for Advanced Energy Conversion and Storage Devices. *Nat. Mater.* **2005**, *4*, 366–377.

(74) Kang, K.; Meng, Y. S.; Breger, J.; Grey, C. P.; Ceder, G. Electrodes with High Power and High Capacity for Rechargeable Lithium Batteries. *Science* **2006**, *311*, 977–980.

(75) Baddour-Hadjean, R.; Pereira-Ramos, J.-P. Raman Microspectrometry Applied to the Study of Electrode Materials for Lithium Batteries. *Chem. Rev.* **2010**, *110*, 1278–1319.

(76) Whittingham, M. S. Intercalation Chemistry and Energy Storage. *J. Solid State Chem.* **1979**, *29*, 303–310.

(77) Scanlon, D. O.; Walsh, A.; Morgan, B. J.; Watson, G. W. An Ab Initio Study of Reduction of V_2O_5 through the Formation of Oxygen Vacancies and Li Intercalation. *J. Phys. Chem. C* **2008**, *112*, 9903–9911.

(78) Piper, L. F. J.; Quackenbush, N. F.; Sallis, S.; Scanlon, D. O.; Watson, G. W.; Nam, K.-W.; Yang, X.-Q.; Smith, K. E.; Omenya, F.; Chernova, N. A.; et al. Elucidating the Nature of Pseudo Jahn-Teller Distortions in Li_xMnPO_4: Combining Density Functional Theory with Soft and Hard X-Ray Spectroscopy. *J. Phys. Chem. C* **2013**, *117*, 10383–10396.

(79) Eyert, V.; Höck, K.-H. Electronic Structure of V_2O_5: Role of Octahedral Deformations. *Phys. Rev. B* **1998**, *57*, 12727–12737.

(80) Ignatiev, A.; Chen, X.; Wu, N.; Lu, Z.; Smith, L. Nanostructured Thin Solid Oxide Fuel Cells with High Power Density. *Dalton Trans.* **2008**, 5501–5506.

(81) Huang, J. Y.; Zhong, L.; Wang, C. M.; Sullivan, J. P.; Xu, W.; Zhang, L. Q.; Mao, S. X.; Hudak, N. S.; Liu, X. H.; Subramanian, A.; et al. In Situ Observation of the Electrochemical Lithiation of a Single SnO_2 Nanowire Electrode. *Science* **2010**, *330*, 1515–1520.

(82) McDowell, M. T.; Ryu, I.; Lee, S. W.; Wang, C.; Nix, W. D.; Cui, Y. Studying the Kinetics of Crystalline Silicon Nanoparticle Lithiation with in Situ Transmission Electron Microscopy. *Adv. Mater.* **2012**, *24*, 6034–6041.

(83) Huggins, R. A.; Nix, W. D. Decrepitation Model For Capacity Loss During Cycling of Alloys in Rechargeable Electrochemical Systems. *Ionics* **2000**, *6*, 57–63.

(84) Yang, J.; Winter, M.; Besenhard, J. O. Small Particle Size Multiphase Li-Alloy Anodes for Lithium-Ion- Batteries. *Solid State Ionics* **1996**, *90*, 281–287.

(85) Whittaker, L.; Velazquez, J. M.; Banerjee, S. A VO-Seeded Approach for the Growth of Star-Shaped VO_2 and V_2O_5 Nanocrystals: Facile Synthesis, Structural Characterization, and Elucidation of Electronic Structure. *CrystEngComm* **2011**, *13*, 5328.

(86) Cava, R. J.; Santoro, A.; Murphy, D. W.; Zahurak, S. M.; Fleming, R. M.; Marsh, P.; Roth, R. S. The Structure of the Lithium-Inserted Metal Oxide δ-LiV_20_5. *J. Solid State Chem.* **1986**, *71*, 63–71.

(87) Delmas, C.; Cognac-Auradou, H. Formation of the W-Type Phase by Lithium Intercalation in (Mo, V) Oxides Deriving from V_2O_5. *J. Power Sources* **1995**, *54*,

406–410.

(88) Rozier, P.; Savariault, J.-M.; Galy, J.; Marichal, C.; Hirschinger, J.; Granger, P. ε-$Li_xV_2O_5$ Bronzes ($0.33 \leq X \leq 0.64$) a Joint Study by X-Ray Powder Diffraction and ^6Li, ^7Li MAS NMR. *Eur. J. Solid State Inorg. Chem.* **1996**, *33*, 1–13.

(89) Baddour-Hadjean, R.; Marzouk, a.; Pereira-Ramos, J. P. Structural Modifications of $Li_xV_2O_5$ in a Composite Cathode ($0 \leq x < 2$) Investigated by Raman Microspectrometry. *J. Raman Spectrosc.* **2012**, *43*, 153–160.

(90) Katzke, H.; Kato, K.; Dinnebier, R. E. Calculation of the Intensity Distribution for One-Dimensionally Disordered $Li_xV_2O_5$ I. The Disordered Phase of ε'-$Li_{0.620(3)}V_2O_5$ at 298K. *Zeitschrift fuer Krist.* **1999**, *214*, 392–397.

(91) Katzke, H.; Czank, M.; Depmeier, W.; van Smaalen, S. On the Incommensurately Modulated Structure of ε'-$Li_xV_2O_5$ at Room Temperature. *Philos. Mag. B* **1997**, *75*, 757–767.

(92) Rozier, P.; Savariault, J. M.; Galy, J. A New Interpretation of the $Li_xV_2O_5$ Electrochemical Behaviour for $1 < X < 3$. *Solid State Ionics* **1997**, *98*, 133–144.

(93) Whittaker, L.; Patridge, C. J.; Banerjee, S. Microscopic and Nanoscale Perspective of the Metal-Insulator Phase. *J. Phys. Chem. Lett.* **2011**, *2*, 745–758.

(94) Navrotsky, A. Nanoscale Effects on Thermodynamics and Phase Equilibria in Oxide Systems. *ChemPhysChem* **2011**, *12*, 2207–2215.

(95) Depner, S. W.; Cultrara, N. D.; Farley, K. E.; Qin, Y.; Banerjee, S. Ferroelastic Domain Organization and Precursor Control of Size in Solution-Grown Hafnium Dioxide Nanorods. *ACS Nano* **2014**, *8*, 4678–4688.

(96) Tian, P.; Zhang, Y.; Senevirathne, K.; Brock, S. L.; Dixit, A.; Lawes, G.; Billinge, S. J. L. Diverse Structural and Magnetic Properties of Differently Prepared MnAs Nanoparticles. *ACS Nano* **2011**, *5*, 2970–2978.

(97) Sides, C. R.; Martin, C. R. Nanostructured Electrodes and the Low-Temperature Performance of Li-Ion Batteries. *Adv. Mater.* **2005**, *17*, 125–128.

(98) Sipr, O.; Simunek, A.; Bocharov, S.; Kirchner, T.; Drager, G. Geometric and Electronic Structure Effects in Polarized V K-Edge Absorption near-Edge Structure Spectra of V_2O_5. *Phys. Rev. B* **1999**, *60*, 14115–14127.

(99) De Francesco, R.; Stener, M.; Causà, M.; Toffoli, D.; Fronzoni, G. Time Dependent Density Functional Investigation of the near-Edge Absorption Spectra of V_2O_5. *Phys. Chem. Chem. Phys.* **2006**, *8*, 4300–4310.

(100) Yamamoto, T. Assignment of Pre-Edge Peaks in K-Edge X-Ray Absorption Spectra of 3d Transition Metal Compounds: Electric Dipole or Quadrupole? *X-Ray Spectrom.* **2008**, *37*, 572–584.

(101) Coulston, G. W.; Bare, Simon, R.; Kung, H.; Birkeland, K.; Bethke, G. K.; Harlow, R.; Herron, N.; Lee, P. L. The Kinetic Significance of V^{5+} in N-Butane Oxidation Catalyzed by Vanadium Phosphates. *Science* **1997**, *275*, 191–193.

(102) Conti, P.; Zamponi, S.; Giorgetti, M.; Berrettoni, M.; Smyrl, W. H. Multivariate Curve Resolution Analysis for Interpretation of Dynamic Cu K-Edge X-Ray Absorption Spectroscopy Spectra for a Cu Doped V_2O_5 Lithium Battery. *Anal. Chem.* **2010**, *82*, 3629–3635.

(103) Li, Y.; El Gabaly, F.; Ferguson, T. R.; Smith, R. B.; Bartelt, N. C.; Sugar, J. D.;

Fenton, K. R.; Cogswell, D. A.; Kilcoyne, A. L. D.; Tyliszczak, T.; et al. Current-Induced Transition from Particle-by-Particle to Concurrent Intercalation in Phase-Separating Battery Electrodes. *Nat. Mater.* **2014**, *13*, 1149–1156.

(104) Bai, P.; Cogswell, D. A.; Bazant, M. Z. Suppression of Phase Separation in $LiFePO_4$ Nanoparticles during Battery Discharge. *Nano Lett.* **2011**, *11*, 4890–4896.

(105) Lim, J.; Li, Y.; Alsem, D. H.; So, H.; Lee, S. C.; Bai, P.; Cogswell, D. A.; Liu, X.; Jin, N.; Yu, Y.; et al. Origin and Hysteresis of Lithium Compositional Spatiodynamics within Battery Primary Particles. *Science* **2016**, *353*, 566-571.

(106) Wang, J.; Chen-Wiegart, Y. K.; Wang, J. In Operando Tracking Phase Transformation Evolution of Lithium Iron Phosphate with Hard X-Ray Microscopy. *Nat. Commun.* **2014**, *5*, 1–10.

(107) Orvananos, B.; Ferguson, T. R.; Yu, H.-C.; Bazant, M. Z.; Thornton, K. Particle-Level Modeling of the Charge-Discharge Behavior of Nanoparticulate Phase-Separating Li-Ion Battery Electrodes. *J. Electrochem. Soc.* **2014**, *161*, A535–A546.

(108) Zhang, X.; van Hulzen, M.; Singh, D. P.; Brownrigg, A.; Wright, J. P.; van Dijk, N. H.; Wagemaker, M. Direct View on the Phase Evolution in Individual $LiFePO_4$ Nanoparticles during Li-Ion Battery Cycling. *Nat. Commun.* **2015**, *6*, 8333.

(109) Wang, J.; Chen-Wiegart, Y. K.; Wang, J. In Operando Tracking Phase Transformation Evolution of Lithium Iron Phosphate with Hard X-Ray Microscopy. *Nat. Commun.* **2014**, *5*, 4570.

(110) Laffont, L.; Delacourt, C.; Gibot, P.; Wu, M. Y.; Kooyman, P.; Masquelier, C.; Tarascon, J. M. Study of the $LiFePO_4/FePO_4$ Two-Phase System by High-

Resolution Electron Energy Loss Spectroscopy. *Chem. Mater.* **2006**, *18*, 5520–5529.

(111) Badi, S.-P.; Wagemaker, M.; Ellis, B. L.; Singh, D. P.; Borghols, W. J. H.; Kan, W. H.; Ryan, D. H.; Mulder, F. M.; Nazar, L. F. Direct Synthesis of Nanocrystalline $Li_{0.90}FePO_4$: Observation of Phase Segregation of Anti-Site Defects on Delithiation. *J. Mater. Chem.* **2011**, *21*, 10085–10093.

(112) Takeuchi, E. S.; Thiebolt III, W. C. The Reduction of Silver Vanadium Oxide in Lithium/silver Vanadium Oxide Cells. *J Electrochem Soc* **1988**, *135*, 2691–2694.

(113) Takeuchi, K. J.; Leising, R. A.; Palazzo, M. J.; Marschilok, A. C.; Takeuchi, E. S. Advanced Lithium Batteries for Implantable Medical Devices: Mechanistic Study of SVO Cathode Synthesis. *J. Power Sources* **2003**, *119–121*, 973–978.

(114) Morcrette, M.; Rozier, P.; Dupont, L.; Mugnier, E.; Sannier, L.; Galy, J.; Tarascon, J.-M. A Reversible Copper Extrusion-Insertion Electrode for Rechargeable Li Batteries. *Nat. Mater.* **2003**, *2*, 755–761.

(115) Morcrette, M.; Martin, P.; Rozier, P.; Vezin, H.; Chevallier, F.; Laffont, L.; Poizot, P.; Tarascon, J.-M. $Cu_{1.1}V_4O_{11}$: A New Positive Electrode Material for Rechargeable Li Batteries. *Chem. Mater.* **2005**, *17*, 418–426.

(116) Schaak, R. E.; Mallouk, T. E. Perovskites by Design: A Toolbox of Solid-State Reactions. *Chem. Mater.* **2002**, *14*, 1455–1471.

(117) Yang, Z.; Ko, C.; Ramanathan, S. Oxide Electronics Utilizing Ultrafast Metal-Insulator Transitions. *Annu. Rev. Mater. Res.* **2011**, *41*, 337–367.

(118) Imada, M.; Fujimori, A.; Tokura, Y. Metal-Insulator Transitions. *Rev. Mod. Phys.*

1998, *70*, 1039–1263.

(119) Ruzmetov, D.; Gopalakrishnan, G.; Ko, C.; Narayanamurti, V.; Ramanathan, S. Three-Terminal Field Effect Devices Utilizing Thin Film Vanadium Oxide as the Channel Layer. *J. Appl. Phys.* **2010**, *107*, 114516.

(120) Li, S. Y.; Namura, K.; Suzuki, M.; Niklasson, G. a.; Granqvist, C. G. Thermochromic VO_2 Nanorods Made by Sputter Deposition: Growth Conditions and Optical Modeling. *J. Appl. Phys.* **2013**, *114*, 33516.

(121) Driscoll, T.; Kim, H.-T.; Chae, B.-G.; Kim, B.-J.; Lee, Y.-W.; Jokerst, N. M.; Palit, S.; Smith, D. R.; Di Ventra, M.; Basov, D. N. Memory Metamaterials. *Science* **2009**, *325*, 1518–1521.

(122) Driscoll, T.; Quinn, J.; Di Ventra, M.; Basov, D. N.; Seo, G.; Lee, Y.-W.; Kim, H.-T.; Smith, D. R. Current Oscillations in Vanadium Dioxide: Evidence for Electrically Triggered Percolation Avalanches. *Phys. Rev. B* **2012**, *86*, 094203.

(123) Jo, S. H.; Chang, T.; Ebong, I.; Bhadviya, B. B.; Mazumder, P.; Lu, W. Nanoscale Memristor Device as Synapse in Neuromorphic Systems. *Nano Lett.* **2010**, *10*, 1297–1301.

(124) Strukov, D. B.; Snider, G. S.; Stewart, D. R.; Williams, R. S. The Missing Memristor Found. *Nature* **2008**, *453*, 80–83.

(125) Wu, C.; Feng, F.; Xie, Y. Design of Vanadium Oxide Structures with Controllable Electrical Properties for Energy Applications. *Chem. Soc. Rev.* **2013**, *42*, 5157–5183.

(126) Li, S.; Li, Y.; Jiang, M.; Ji, S.; Luo, H.; Gao, Y.; Jin, P. Preparation and

Characterization of Self-Supporting Thermochromic Films Composed of VO_2(M)@SiO_2 Nanofibers. *ACS Appl. Mater. Interfaces* **2013**, *5*, 6453–6457.

(127) Cao, J.; Ertekin, E.; Srinivasan, V.; Fan, W.; Huang, S.; Zheng, H.; Yim, J. W. L.; Khanal, D. R.; Ogletree, D. F.; Grossman, J. C.; et al. Strain Engineering and One-Dimensional Organization of Metal – Insulator Domains in Single-Crystal Vanadium Dioxide Beams. *Nat. Nanotechnol.* **2009**, *4*, 732–737.

(128) Yamauchi, T.; Ueda, Y. Superconducting B(β′)-Vanadium Bronzes under Pressure. *Phys. Rev. B* **2008**, *77*, 104529-1–18.

(129) Cao, J.; Gu, Y.; Fan, W.; Chen, L. Q.; Ogletree, D. F.; Chen, K.; Tamura, N.; Kunz, M.; Barrett, C.; Seidel, J.; et al. Extended Mapping and Exploration of the Vanadium Dioxide Stress-Temperature Phase Diagram. *Nano Lett.* **2010**, *10*, 2667–2673.

(130) Lopez, R.; Feldman, L.; Haglund, R. Size-Dependent Optical Properties of VO_2 Nanoparticle Arrays. *Phys. Rev. Lett.* **2004**, *93*, 177403.

(131) Lopez, R.; Boatner, L. A.; Haynes, T. E.; Feldman, L. C.; Haglund, R. F. Synthesis and Characterization of Size-Controlled Vanadium Dioxide Nanocrystals in a Fused Silica Matrix. *J. Appl. Phys.* **2002**, *92*, 4031.

(132) Katzke, H.; Tolédano, P.; Depmeier, W. Theory of Morphotropic Transformations in Vanadium Oxides. *Phys. Rev. B* **2003**, *68*, 24109.

(133) Youn, D.-H.; Kim, H.-T.; Chae, B.-G.; Hwang, Y.-J.; Lee, J.-W.; Maeng, S.-L.; Kang, K.-Y. Phase and Structural Characterization of Vanadium Oxide Films Grown on Amorphous SiO_2/Si Substrates. *J. Vac. Sci. Technol. A Vacuum,*

Surfaces, Film. **2004**, *22*, 719.

(134) Tashman, J. W.; Lee, J. H.; Paik, H.; Moyer, J. A.; Misra, R.; Mundy, J. A.; Spila, T.; Merz, T. A.; Schubert, J.; Muller, D. A.; et al. Epitaxial Growth of VO_2 by Periodic Annealing. *Appl. Phys. Lett.* **2014**, *104*, 63104.

(135) Fan, L. L.; Chen, S.; Wu, Y. F.; Chen, F. H.; Chu, W. S.; Chen, X.; Zou, C. W.; Wu, Z. Y. Growth and Phase Transition Characteristics of Pure M-Phase VO_2 Epitaxial Film Prepared by Oxide Molecular Beam Epitaxy. *Appl. Phys. Lett.* **2013**, *103*, 131914.

(136) Leroux, C.; Nihoul, G.; Van Tendeloo, G. From VO_2 (B) to VO_2 (R): Theoretical Structures of VO_2 Polymorphs and in Situ Electron Microscopy. *Phys. Rev. B* **1998**, *57*, 5111–5121.

(137) Oka, Y.; Sato, S.; Yao, T.; Yamamoto, N. Crystal Structures and Transition Mechanism of VO_2 (A). *J. Solid State Chem.* **1998**, 141, 594–598.

(138) Liu, M.; Wagner, M.; Zhang, J.; McLeod, A.; Kittiwatanakul, S.; Fei, Z.; Abreu, E.; Goldflam, M.; Sternbach, A. J.; Dai, S.; et al. Symmetry Breaking and Geometric Confinement in VO_2: Results from a Three-Dimensional Infrared Nano-Imaging. *Appl. Phys. Lett.* **2014**, *104*, 121905.

(139) Mai, L. Q.; Hu, B.; Hu, T.; Chen, W.; Gu, E. D. Electrical Property of Mo-Doped VO_2 Nanowire Array Film by Melting-Quenching Sol-Gel Method. *J. Phys. Chem. B* **2006**, *110*, 19083–19086.

(140) Pan, M.; Zhong, H.; Wang, S.; Liu, J.; Li, Z.; Chen, X.; Lu, W. Properties of VO_2 Thin Film Prepared with Precursor $VO(acac)_2$. *J. Cryst. Growth* **2004**, *265*, 121–

126.

(141) Berglund, C. N.; Guggenheim, H. J. Electronic Properties of VO_2 near the Semiconductor-Metal Transition. *Phys. Rev.* **1969**, *185*, 1022–1033.

(142) Salker, A. V.; Seshan, K.; Keer, H. V. Phase Transition Behaviour of VO_2. *Phys. Stat. Sol. A* **1983**, *75*, K37–K40.

(143) Whittaker, L.; Wu, T.; Stabile, A.; Sambandamurthy, G.; Banerjee, S.; Al, W. E. T. Single-Nanowire Raman Microprobe Studies of Doping-, Temperature-, and Voltage-Induced Metal-Insulator Transitions of $W_xV_{1-x}O_2$ Nanowires. *ACS Nano* **2011**, *5*, 8861–8867.

(144) Zhang, S.; Chou, J. Y.; Lauhon, L. J. Direct Correlation of Structural Domain Formation with the Metal Insulator Transition in a VO_2 Nanobeam. *Nano Lett.* **2009**, *9*, 4527–4532.

(145) Donev, E. U.; Lopez, R.; Feldman, L. C.; Haglund, R. F. Confocal Raman Microscopy across the Metal-Insulator Transition of Single Vanadium Dioxide Nanoparticles. *Nano Lett.* **2009**, *9*, 702–706.

(146) Schilbe, P. Raman Scattering in VO_2. *Phys. B* **2002**, *316–317*, 600–602.

(147) Chou, J. Y.; Lensch-Falk, J. L.; Hemesath, E. R.; Lauhon, L. J. Vanadium Oxide Nanowire Phase and Orientation Analyzed by Raman Spectroscopy. *J. Appl. Phys.* **2009**, *105*, 34310.

(148) Waitz, T.; Tsuchiya, K.; Antretter, T.; Fischer, F. D. Phase Transformations of Nanocrystalline Martensitic Materials. *MRS Bulletiin* **2009**, *34*, 814–821.

(149) Maeng, J.; Kim, T.-W.; Jo, G.; Lee, T. Fabrication, Structural and Electrical

Characterization of VO_2 Nanowires. *Mater. Res. Bull.* **2008**, *43*, 1649–1656.

(150) Taguchi, Y.; Matsumoto, T.; Tokura, Y.; Sr, T. Dielectric Breakdown of One-Dimensional Mott Insulators Sr_2CuO_3 and $SrCuO_2$. *Phys. Rev. B* **2000**, *62*, 7015–7018.

(151) Maki, K. Thermal Fluctuations of the Order Parameter in Charge-Density Waves. *Phys. Rev. B* **1986**, *33*, 2852–2854.

(152) Sharoni, A.; Ramírez, J.; Schuller, I. Multiple Avalanches across the Metal-Insulator Transition of Vanadium Oxide Nanoscaled Junctions. *Phys. Rev. Lett.* **2008**, *101*, 26404.

(153) Stabile, A. A.; Singh, S. K.; Wu, T.; Banerjee, S.; Sambandamurthy, G. Separating Electric Field and Thermal Effects across the Metal-Insulator Transition in Vanadium Oxide Nanobeams. 1404.4129, arXiv.org e-Print archive. http://arxiv.org/abs/1310.5021 (accessed Apr 14, 2014). **2014**, 1–13.

(154) Tarascon, J.-M. Key Challenges in Future Li-Battery Research. *Philos. Trans. R. Soc. A* **2010**, *368*, 3227–3241.

(155) Winter, M.; Besenhard, J. O.; Spahr, M. E.; Novak, P. Insertion Electrode Materials for Rechargeable Lithium Batteries. *Adv. Mater.* **1998**, 10, 725–763.

(156) Sides, C. R.; Li, N.; Patrissi, C. J.; Scrosati, B.; Martin, C. R. Nanoscale Materials for Lithium-Ion Batteries. *MRS Bulletiin* **2002**, *27*, 604–607.

(157) Nazar, L. F.; Goward, G.; Leroux, F.; Duncan, M.; Huang, H.; Kerr, T.; Gaubicher, J. Nanostructured Materials for Energy Storage. *Int. J. Inorg. Mater.* **2001**, *3*, 191–200.

(158) Wang, Y.; Cao, G. Synthesis and Enhanced Intercalation Properties of Nanostructured Vanadium Oxides. *Chem. Mater.* **2006**, *18*, 2787–2804.

(159) Delmas, C.; Cognac-Auradou, H.; Cocciantelli, J. M.; Menetrier, M.; Doumerc, J. P. The $Li_xV_2O_5$ System: An Overview of the Structure Modifications Induced by the Lithium Intercalation. *Solid State Ionics* **1994**, *69*, 257–264.

(160) Rocquefelte, X.; Boucher, F.; Gressier, P.; Ouvrard, G. First-Principle Study of the Intercalation Process in the $Li_xV_2O_5$ System. *Chem. Mater.* **2003**, *6*, 1812–1819.

(161) Leger, C.; Bach, S.; Soudan, P.; Pereira-Ramos, J.-P. Structural and Electrochemical Properties of ω-$Li_xV_2O_5$ ($0.4 \leq x \leq 3$) as Rechargeable Cathodic Material for Lithium Batteries. *J. Electrochem. Soc.* **2005**, *152*, A236.

(162) Satto, C.; Sciau, P.; Dooryhee, E.; Galy, J.; Millet, P. The δ-ε-γ LiV_2O_5 "High Temperature" Phase Transitions Evidenced by Synchrotron X-Ray Powder Diffraction Analysis. *J. Solid State Chem.* **1999**, *109*, 103–109.

(163) Galy, J.; Satto, C.; Sciau, P.; Millet, P. Atomic Modeling of the δ→ε LiV_2O_5 Phase Transition and Simulation of the XRD Powder Pattern Evolution. *J. Solid State Chem.* **1999**, *146*, 129–136.

(164) Whittingham, M. S.; Dines, M. B. n-Butyllithium—An Effective, General Cathode Screening Agent. *J. Electrochem. Soc.* **1977**, *124*, 1387–1388.

(165) Dickens, P. G.; French, S. J.; Hight, A. T.; Pye, M. F. Phase Relationships in the Ambient Temperature $Li_xV_2O_5$ System ($0.1 < X < 1.0$). *Mater. Res. Bull.* **1979**, *14*, 1295–1299.

(166) Garcia, B.; Millet, M.; Pereira-Ramos, J. P.; Baffier, N.; Bloch, D. Electrochemical

Behaviour of Chemically Lithiated $Li_xV_2O_5$ Phases ($0.9 < X < 1.6$). *J. Power Sources* **1999**, *81*, 670–674.

(167) Katzke, H.; Czank, M.; Depmeier, W.; van Smaalen, S. The Stoichiometric Dependence of the Modulation Wave Vector in the Incommensurately Modulated Structures of The Stoichiometric Dependence of the Modulation Wave Vector in the Incommensurately Modulated Structures of ε-$Li_xV_2O_5$ and ε′-$Li_xV_2O_5$. *J. Phys. Condens. Matter* **1997**, *9*, 6231–6239.

(168) Patrissi, C. J.; Martin, C. R. Sol-Gel-Based Template Synthesis and Li-Insertion Rate Performance of Nanostructured Vanadium Pentoxide. *J. Electrochem. Soc.* **1999**, *146*, 3176–3180.

(169) Baddour-Hadjean, R.; Raekelboom, E.; Pereira-Ramos, J.-P. New Structural Characterization of the $Li_xV_2O_5$ System Provided by Raman Spectroscopy. *Chem. Mater.* **2006**, *18*, 3548–3556.

(170) Cocciantelli, J. M.; Doumerc, J. P.; Pouchard, M.; Broussely, M.; Labat, J. Crystal Chemistry of Electrochemically Inserted $Li_xV_2O_5$. *J. Power Sources* **1991**, *34*, 103–111.

(171) Baddour-Hadjean, R.; Golabkan, V.; Pereira-Ramos, J. P.; Mantoux, a.; Lincot, D. A Raman Study of the Lithium Insertion Process in Vanadium Pentoxide Thin Films Deposited by Atomic Layer Deposition. *J. Raman Spectrosc.* **2002**, *33*, 631–638.

(172) Baddour-Hadjean, R.; Pereira-Ramos, J. P.; Navone, C.; Smirnov, M. Raman Microspectrometry Study of Electrochemical Lithium Intercalation into Sputtered

Crystalline V_2O_5 Thin Films. *Chem. Mater.* **2008**, *20*, 1916–1923.

(173) Rey, I.; Bruneel, J.-L.; Grondn, J.; Servant, L.; Lassègues, J.-C. Raman Spectroelectrochemistry of a Lithium/Polymer Electrolyte Symmetric Cell. *J. Electrochem. Soc.* **1998**, *145*, 3043–3042.

(174) Rey, I.; Lassegues, J. C.; Baudry, P.; Majastre, H. Study of a Lithium Battery by Confocal Raman Microspectrometry. *Electrochim. Acta* **1998**, *43*, 1539–1544.

(175) Zhang, X.; Frech, R. In Situ Roman Specfroscopy of $Li_xV_2O_5$ in a Lithium Rechargeable Battery. *J. Electrochem. Soc.* **1998**, *145*, 847–851.

(176) Zhang, X.; Frech, R. Vibrational Spectroscopic Study of Lithium Vanadium Pentoxides. *Electrochim. Acta* **1997**, *42*, 475–482.

(177) Abello, L.; Husson, E.; Repelin, Y.; Lucazeau, G. Vibrational Spectra and Valence Force Field of Crystalling V2O5. *Spectrochim. Acta* **1983**, *39A*, 641–651.

(178) Baddour-Hadjean, R.; Navone, C.; Pereira-Ramos, J. P. In Situ Raman Microspectrometry Investigation of Electrochemical Lithium Intercalation into Sputtered Crystalline V2O5 Thin Films. *Electrochim. Acta* **2009**, *54*, 6674–6679.

(179) McGraw, J. M.; Perkins, J. D.; Zhang, J.-G.; Liu, P.; Parilla, P. A.; Turner, J.; Schulz, D. L.; Curtis, C. J.; Ginley, D. S. Next Generation V_2O_5 Cathode Materials for Li Rechargeable Batteries. *Solid State Ionics* **1998**, *115*, 407–413.

(180) Cazzanelli, E.; Mariotto, G.; Passerini, S.; Decker, F. Spectroscopic Investigations of Li-Intercalated V_2O_5 Polycrystalline Films. *Solid State Ionics* **1994**, No. 70, 412–416.

(181) Julien, C.; Ivanov, I.; Gorenstein, A. Vibrational Modifications on Lithium

Intercalation in V_20_5 Films. *Mater. Sci. Eng. B* **1995**, *B33*, 168–172.

(182) Velazquez, J. M.; Banerjee, S. Catalytic Growth of Single-Crystalline V_2O_5 Nanowire Arrays. *Small* **2009**, *5*, 1025–1029.

(183) Patridge, C. J.; Wu, T.-L.; Sambandamurthy, G.; Banerjee, S. Colossal above-Room-Temperature Metal-Insulator Switching of a Wadsley-Type Tunnel Bronze. *Chem. Commun.* **2011**, *47*, 4484–4486.

(184) Patridge, C. J.; Jaye, C.; Zhang, H.; Marschilok, A. C.; Fischer, D. A.; Takeuchi, E. S.; Banerjee, S. Synthesis, Structural Characterization, and Electronic Structure of Single-Crystalline $Cu_xV_2O_5$ Nanowires. *Inorg. Chem* **2009**, *48*, 3145–3152.

(185) Malik, R.; Zhou, F.; Ceder, G. Kinetics of Non-Equilibrium Lithium Incorporation in $LiFePO_4$. *Nat. Mater.* **2011**, *10*, 587–590.

(186) Rozier, P.; Tarascon, J. M. Review—Li-Rich Layered Oxide Cathodes for Next-Generation Li-Ion Batteries: Chances and Challenges. *J. Electrochem. Soc.* **2015**, *162*, A2490–A2499.

(187) Armand, M.; Tarascon, J.-M. Building Better Batteries. *Nature* **2008**, *451*, 652–657.

(188) Whittingham, M. S. Ultimate Limits to Intercalaton Reactions Fo Lithium Batteries. *Chem. Rev.* **2014**, *114*, 11414–11443.

(189) Tarascon, J. M.; Armand, M. Issues and Challenges Facing Rechargeable Lithium Batteries. *Nature* **2001**, *414*, 359–367.

(190) Sai Gautam, G.; Canepa, P.; Abdellahi, A.; Urban, A.; Malik, R.; Ceder, G. The Intercalation Phase Diagram of Mg in V_2O_5 from First-Principles. *Chem. Mater.*

2015, *27*, 3733–3742.

(191) Li, L.; Chen-Wiegart, Y. K.; Wang, J.; Gao, P.; Ding, Q.; Yu, Y.-S.; Wang, F.; Cabana, J.; Wang, J.; Jin, S. Visualization of Electrochemically Driven Solid-State Phase Transformations Using Operando Hard X-Ray Spectro-Imaging. *Nat. Commun.* **2015**, *6*, 6883.

(192) Van der Ven, A.; Bhattacharya, J.; Belak, A. A. Understanding Li Diffusion in Li-Intercalation. *Accounts Chem. Reserach* **2011**, *46*, 1216–1225.

(193) Wiaderek, K. M.; Borkiewicz, O. J.; Castillo-Martínez, E.; Robert, R.; Pereira, N.; Amatucci, G. G.; Grey, C. P.; Chupas, P. J.; Chapman, K. W. Comprehensive Insights into the Structural and Chemical Changes in Mixed-Anion FeOF Electrodes by Using Operando Pdf and NMR Spectroscopy. *J. Am. Chem. Soc.* **2013**, *135*, 4070–4078.

(194) Wang, F.; Yu, H.-C.; Chen, M.-H.; Wu, L.; Pereira, N.; Thornton, K.; Van der Ven, A.; Zhu, Y.; Amatucci, G. G.; Graetz, J. Tracking Lithium Transport and Electrochemical Reactions in Nanoparticles. *Nat. Commun.* **2012**, *3*, 1201.

(195) Gao, Q.; Meng, G.; Nie, A.; Mashayek, F.; Wang, C.; Odegard, G. M.; Shahbazian-Yassar, R. Direct Evidence of Lithium-Induced Atomic Ordering in Amorphous TiO_2 Nanotubes. *Chem. Mater.* **2014**, *26*, 1660–1669.

(196) Ohmer, N.; Fenk, B.; Samuelis, D.; Chen, C.-C.; Maier, J.; Weigand, M.; Goering, E.; Schütz, G. Phase Evolution in Single-Crystalline $LiFePO_4$ Followed by in Situ Scanning X-Ray Microscopy of a Micrometre-Sized Battery. *Nat. Commun.* **2015**, *6*, 6045.

(197) Stallworth, P. E.; Kostov, S.; DenBoer, M. L.; Greenbaum, S. G.; Lampe-Onnerud, C. X-Ray Absorption and Magnetic Resonance Spectroscopic Studies of $Li_xV_6O_{13}$. *J. Appl. Phys.* **1998**, *83*, 1247.

(198) Leifer, N. D.; Colon, A.; Martocci, K.; Greenbaum, S. G.; Alamgir, F. M.; Reddy, T. B.; Gleason, N. R.; Leising, R. A.; Takeuchi, E. S. Nuclear Magnetic Resonance and X-Ray Absorption Spectroscopic Studies of Lithium Insertion in Silver Vanadium Oxide Cathodes. *J. Electrochem. Soc.* **2007**, *154*, A500–A506.

(199) Love, C. T.; Korovina, A.; Patridge, C. J.; Swider-Lyons, K. E.; Twigg, M. E.; Ramaker, D. E. Review of $LiFePO_4$ Phase Transition Mechanisms and New Observations from X-Ray Absorption Spectroscopy. *J. Electrochem. Soc.* **2013**, *160*, A3153–A3161.

(200) Wong, J.; Lytle, F. W.; Messmer, R. P.; Maylotte, D. H. K-Edge Absoption Spectra of Selected Vanadium Compounds. *Phys. Rev. B* **1984**, *30*, 5596–5610.

(201) Poumellec, B.; Cortes, R.; Sanchez, C.; Berthon, J.; Fretigny, C. Polarized XANES and EXAFS at the V K-Edge of $VOPO_4$*H_2O Gel, Comparison with the V K-Edge in V_2O_5 Xerogel. *J. Phys. Chem. Solids* **1993**, *54*, 751–763.

(202) Stizza, S.; Benfatto, M.; Bianconi, A.; Garcia, J.; Mancini, G.; Natoli, C. Vanadium Site Structure in V_2O_5 Gel by Polarized EXAFS and XANES. *J. Phys. Colloq.* **1986**, *47*, C8-691-C8-696.

(203) Giorgetti, M.; Berrettoni, M.; Passerini, S.; Smyrl, W. H. Absorption of Polarized X-Rays by V_2O_5-Based Cathodes for Lithium Batteries: An Application. *Electrochim. Acta* **2002**, *47*, 3163–3169.

(204) Giorgetti, M.; Passerini, S.; Smyrl, W. H.; Mukerjee, S.; Yang, X. Q.; McBreen, J. In Situ X-Ray Absorption Spectroscopy Characterization of V_2O_5 Xerogel Cathodes upon Lithium Intercalation. *J. Electrochem. Soc.* **1999**, *146*, 2387–2392.

(205) Stizza, S.; Benfatto, M.; Davoli, I.; Mancini, G.; Marcelli, A.; Bianconi, A.; Tomelini, M.; Garcia, J. On the Basic Structural Unit of Amorphous V_2O_5 From XANES and EXAFS. *J. Phys. Colloq.* **1985**, *46*, C8-255-C8-259.

(206) Farges, F.; Brown, G.; Rehr, J. Ti K-Edge XANES Studies of Ti Coordination and Disorder in Oxide Compounds: Comparison between Theory and Experiment. *Phys. Rev. B* **1997**, *56*, 1809–1819.

(207) Coulston, G. W.; Bare, Simon, R.; Kung, H.; Birkeland, K.; Bethke, G. K.; Harlow, R.; Herron, N.; Lee, P. L. The Kinetic Significance of V^{5+} in N-Butane Oxidation Catalyzed by Vanadium Phosphates. *Science* **1997**, *275*, 191–193.

(208) Ravel, B.; Newville, M. ATHENA, ARTEMIS, HEPHAESTUS: Data Analysis for X-Ray Absorption Spectroscopy Using IFEFFIT. *J. Synchrotron Radiat.* **2005**, *12*, 537–541.

(209) Ravel, B.; Newville, M. ATHENA and ARTEMIS Interactive Graphical Data Analysisusing IFEFFIT. *Phys. Scr.* **2005**, *T115*, 1007.

(210) Kohn, W.; Sham, L. J. Self-Consistent Equations Including Exchange and Correlation Effects. *Phys. Rev.* **1965**, *140*, A1133–A1138.

(211) Hohenberg, P.; Kohn, W. Inhomogeneous Electron Gas. *Phys. Rev.* **1964**, *136*, B864–B871.

(212) Kresse, G.; Furthmüller, J. Efficiency of Ab-Initio Total Energy Calculations for

Metals and Semiconductors Using a Plane-Wave Basis Set. *Comput. Mater. Sci.* **1996**, *6*, 15–50.

(213) Perdew, J. P.; Burke, K.; Ernzerhof, M. Generalized Gradient Approximation Made Simple. *Phys. Rev. Lett.* **1996**, *77*, 3865–3868.

(214) Perdew, J. P.; Burke, K.; Ernzerhof, M. Generalized Gradient Approximation Made Simple- ERRATA. *Phys. Rev. Lett.* **1997**, *78*, 1396.

(215) Wang, L.; Maxisch, T.; Ceder, G. Oxidation Energies of Transition Metal Oxides within the GGA+U Framework. *Phys. Rev. B* **2006**, *73*, 195107-1-195107–6.

(216) Blöchl, P. E. Projector Augmented-Wave Method. *Phys. Rev. B* **1994**, *50*, 17953–17979.

(217) Kresse, G.; Joubert, D. From Ultrasoft Pseudopotentials to the Projector Augmented-Wave Method. *Phys. Rev. B* **1999**, *59*, 1758–1775.

(218) Goering, E.; Müller, O.; Klemm, M.; DenBoer, M. L.; Horn, S. Angle Dependent Soft-X-Ray Absorption Spectroscopy of V_2O_5. *Philos. Mag. Part B* **1997**, *75*, 229–236.

(219) Joseph, B.; Iadecola, A.; Maugeri, L.; Bendele, M.; Okubo, M.; Li, H.; Zhou, H.; Mizokawa, T.; Saini, N. L. Distinct Local Structure of Nanoparticles and Nanowires of V_2O_5 Probed by X-Ray Absorption Spectroscopy. *Appl. Phys. Lett.* **2013**, *103*, 251910.

(220) Ramaker, D. E.; Koningsberger, D. C. Parameter-Free Calculations of X-Ray Spectra with FEFF9. *Phys. Chem. Chem. Phys.* **2010**, *12*, 5514–5534.

(221) Giuli, G.; Paris, E.; Mungall, J.; Romano, C.; Dingwell, D. V Oxidation State and

Coordination Number in Silicate Glasses by XAS. *Am. Mineral.* **2004**, *89*, 1640–1646.

(222) Goodenough, J. B.; Park, K. The Li-Ion Rechargeable Battery : A Perspective. *J. Am. Chem. Soc.* **2013**, *135*, 1167–1176.

(223) Tarascon, J. M.; Delacourt, C.; Prakash, A. S.; Morcrette, M.; Hegde, M. S.; Wurm, C.; Masquelier, C. Various Strategies to Tune the Ionic/Electronic Properties of Electrode Materials. *Dalt. Trans.* **2004**, *19*, 2988–2994.

(224) Malik, R.; Abdellahi, A.; Ceder, G. A Critical Review of the Li Insertion Mechanisms in $LiFePO_4$ Electrodes. *J. Electrochem. Soc.* **2013**, *160*, A3179–A3197.

(225) Ferguson, T. R.; Bazant, M. Z. Nonequilibrium Thermodynamics of Porous Electrodes. *J. Electrochem. Soc.* **2012**, *159*, A1967–A1985.

(226) Barim, G.; Cottingham, P.; Zhou, S.; Melot, B. C.; Brutchey, R. L. Investigating the Mechanism of Reversible Lithium Insertion into Anti-NASICON $Fe_2(WO_4)_3$. *ACS Appl. Mater. Interfaces* **2017**, *2*, 10813–10819.

(227) Zhou, S.; Barim, G.; Morgan, B. J.; Melot, B. C.; Brutchey, R. L. Influence of Rotational Distortions on Li^+- and Na^+-Intercalation in Anti-NASICON $Fe_2(MoO_4)_3$. *Chem. Mater.* **2016**, *28*, 4492–4500.

(228) Quackenbush, N. F.; Wangoh, L.; Scanlon, D. O.; Zhang, R.; Chung, Y.; Chen, Z.; Wen, B.; Lin, Y.; Woicik, J. C.; Chernova, N. A.; et al. Interfacial Effects in ε-Li_xVOPO_4 and Evolution of the Electronic Structure. *Chem. Mater.* **2015**, *27*, 8211–8219.

(229) Abraham, A.; Housel, L. M.; Lininger, C. N.; Bock, D. C.; Jou, J.; Wang, F.; West, A. C.; Marschilok, A. C.; Takeuchi, K. J.; Takeuchi, E. S. Investigating the Complex Chemistry of Functional Energy Storage Systems: The Need for an Integrative, Multiscale (Molecular to Mesoscale) Perspective. *ACS Cent. Sci.* **2016**, *2*, 380–387.

(230) Whittingham, M. S. Electrical Energy Storage and Intercalation Chemistry. *Science* **1976**, *192*, 1126–1127.

(231) Murphy, D. W.; Christian, P. A.; DiSalvo, F. J.; Waszczak, J. V. Lithium Incorporation by Vanadium Pentoxide. *Inorg. Chem.* **1979**, *18*, 2800–2803.

(232) Withers, R. L.; Millet, P.; Tabira, Y. The Inherent Displacive Structural Flexibility of $M_xV_2O_5$ Framework Structures. *Zeitschrift fuer Krist.* **2000**, *215*, 357–363.

(233) Parija, A.; Liang, Y.; Andrews, J. L.; De Jesus, L. R.; Prendergast, D.; Banerjee, S. Topochemically De-Intercalated Phases of V_2O_5 as Cathode Materials for Multivalent Intercalation Batteries: A First-Principles Evaluation. *Chem. Mater.* **2016**, *28*, 5611–5620.

(234) Clites, M.; Byles, B.; Pomerantseva, E. Effect of Aging and Hydrothermal Treatment on Electrochemical Performance of Chemically Pre-Intercalated Na-V-O Nanowires for Na-Ion Batteries. *J. Mater. Chem. A* **2016**, *4*, 7754–7761.

(235) Wang, W.; Wang, H.; Liu, S.; Huang, J. Synthesis of γ-LiV_2O_5 Nanorods as a High-Performance Cathode for Li-Ion Battery. *J. Solid State Electrochem* **2012**, *16*, 2555–2561.

(236) Li, W.-D.; Xu, C.-Y.; Du, Y.; Fang, H.-T.; Feng, Y.-J.; Zhen, L. Electrochemical

Lithium Insertion Behavior of β-$Li_xV_2O_5$ ($0 \leq X \leq 3$) as the Cathode Material for Secondary Lithium Batteries. *J. Electrochem. Soc.* **2013**, *161*, A75–A83.

(237) Kresse, G.; Hafner, J. Ab Initio Molecular Dynamics for Liquid Metals. *Phys. Rev. B* **1993**, *47*, 558–561.

(238) Dudarev, S. L.; Botton, G. A.; Savrasov, S. Y.; Humphreys, C. J.; Sutton, A. P. Electron-Energy-Loss Spectra and the Structural Stability of Nickel Oxide: An LSDA+U Study. *Phys. Rev. B* **1998**, *57*, 1505–1509.

(239) Zhou, B.; Shi, H.; Cao, R.; Zhang, X.; Jiang, Z. Theoretical Study on the Initial Stage of a Magnesium Battery Based on a V_2O_5 Cathode. *Phys. Chem. Chem. Phys.* **2014**, *16*, 18578–18585.

(240) Klime, J.; Bowler, D. R.; Michaelides, A. Van Der Waals Density Functionals Applied to Solids. *Phys. Rev. B* **2011**, *83*, 195131.

(241) Román-Pérez, G.; Soler, J. M. Efficient Implementation of a van Der Waals Density Functional: Application to Double-Wall Carbon Nanotubes. *Phys. Rev. Lett.* **2009**, *103*, 96102-1–4.

(242) Dion, M.; Rydberg, H.; Schröder, E.; Langreth, D. C.; Lundqvist, B. I. Van Der Waals Density Functional for General Geometries. *Phys. Rev. Lett.* **2004**, *92*, 246401-1–4.

(243) Lee, K.; Murray, É. D.; Kong, L.; Lundqvist, B. I.; Langreth, D. C. Higher-Accuracy van Der Waals Density Functional. *Phys. Rev. B* **2010**, *82*, 81101-3–6.

(244) Ding, H.; Lin, H.; Sadigh, B.; Zhou, F.; Ozoliņš, V.; Asta, M. Computational Investigation of Electron Small Polarons in α-MoO_3. *J. Phys. Chem. C* **2014**, *118*,

15565–15572.

APPENDIX A

SUPPLEMENTARY FIGURES AND TABLES

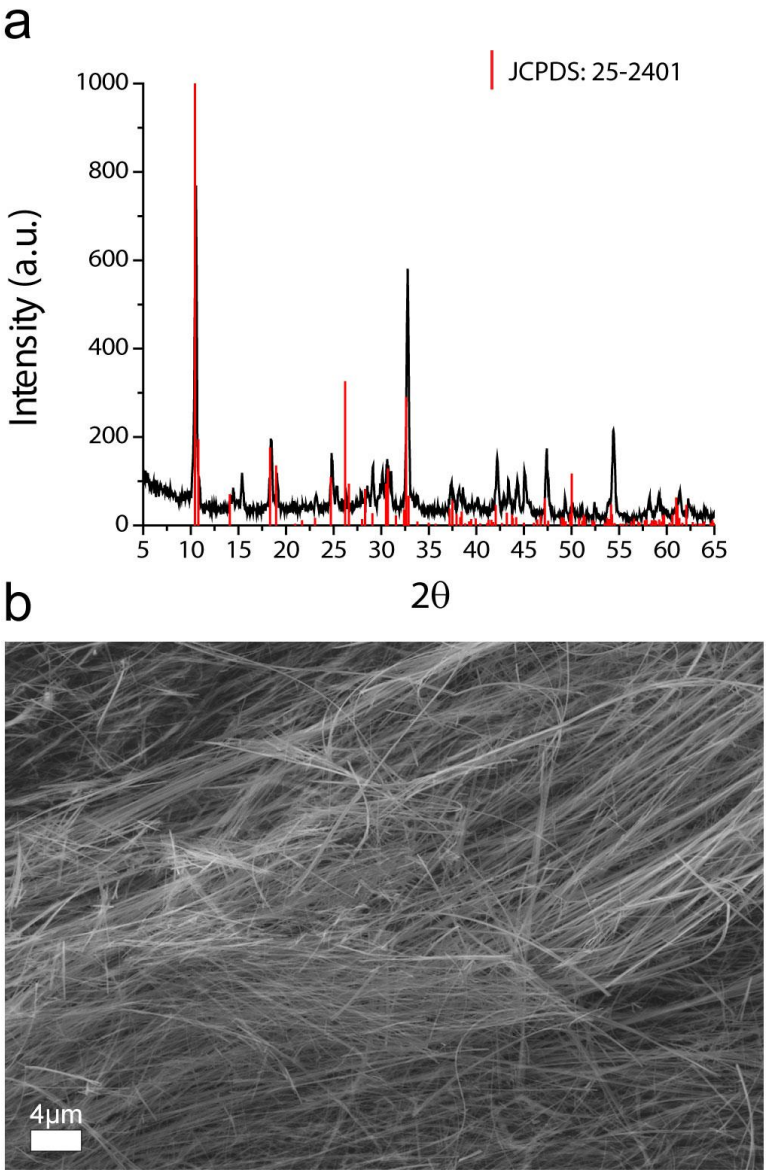

Figure A. 1: X-Ray Diffraction (a), and SEM micrograph (b) of as synthesized V_3O_7 prior to oxidation to V_2O_5. Reprinted from 48.

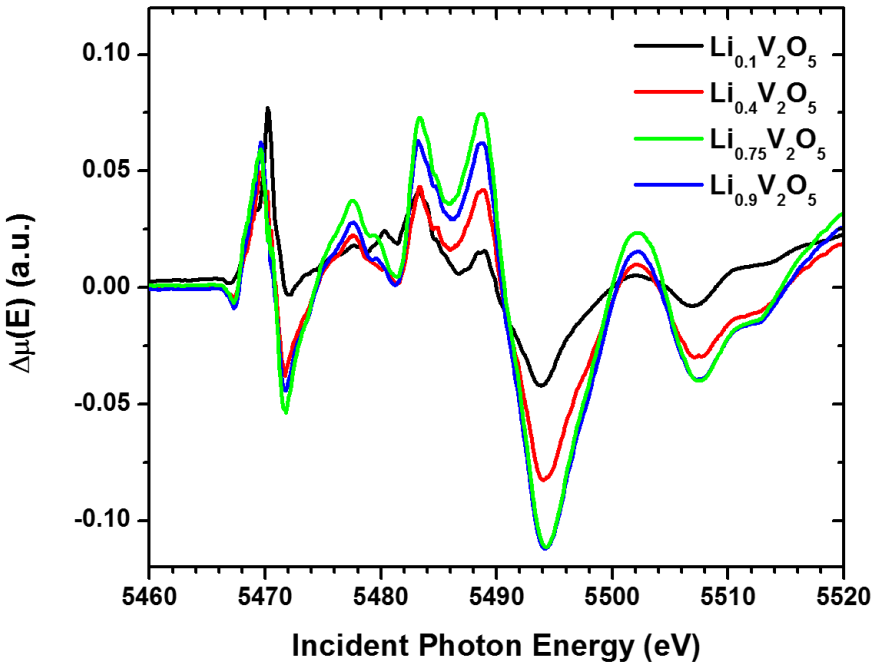

Figure A. 2: Δμ-XANES spectra deduced for varying extents of lithiation of V_2O_5. Reprinted from 47.

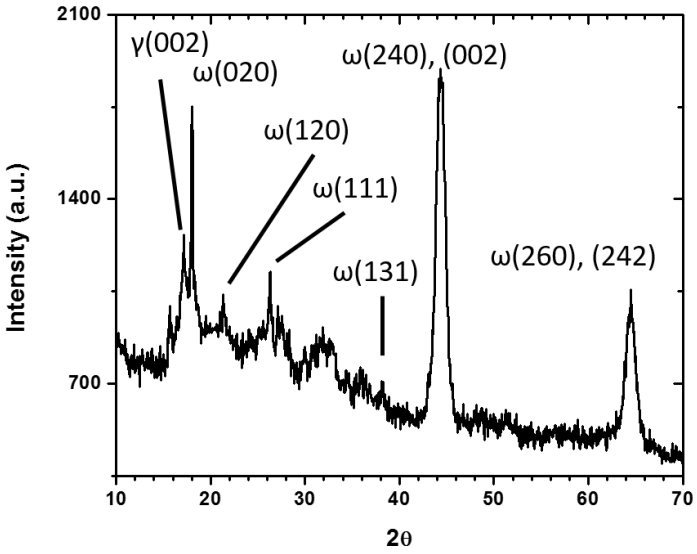

Figure A. 3: Powder X-ray diffraction pattern acquired for a nominal stoichiometry of $Li_{2.5}V_2O_5$ indicating stabilization of the ω-phase of $Li_xV_2O_5$. Reprinted from 47.

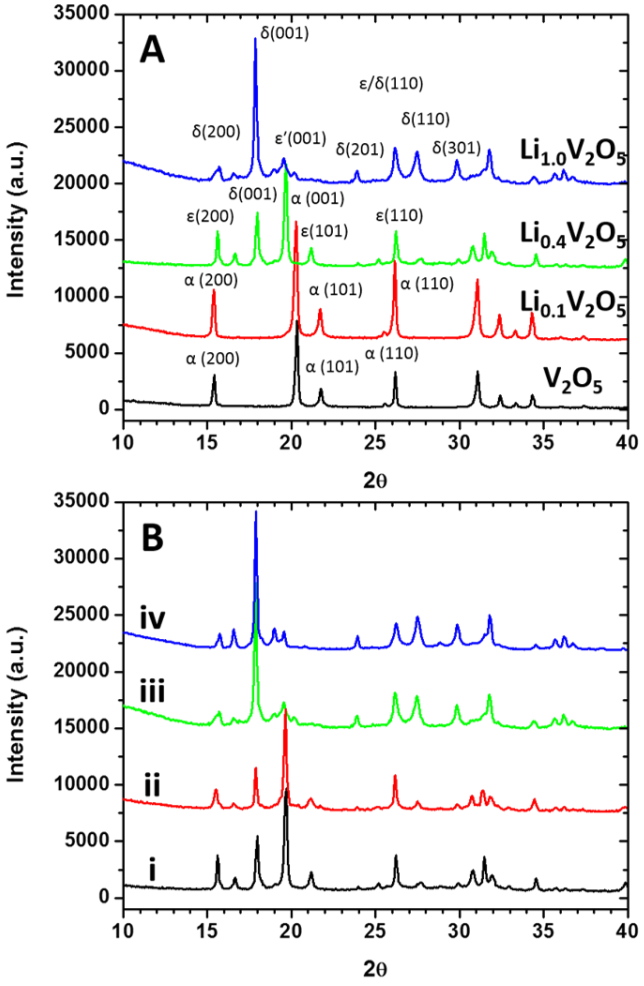

Figure A. 4: Powder X-ray diffraction patterns acquired for (A) chemically lithiated V_2O_5 with varying nominal Li-ion concentrations. Powder X-ray diffraction patterns of $Li_{0.4}V_2O_5$ immediately after synthesis (B, i) and two weeks after synthesis (B, ii), and $Li_{1.0}V_2O_5$ immediately after synthesis (B, iii), and two weeks after synthesis (B, iv). Reprinted from 47.

Table A. 1: Select bond angles and bond distances for the ζ-V_2O_5 and β'-$Li_{0.083}V_2O_5$ phases.

	ζ-V_2O_5	β′-$Li_{0.083}V_2O_5$
O1 – V1 – O3	**105.9°**	**102.2°**
O3 – V2 – O2	**105.9°**	**101.2°**
O1 – V1	**1.62 Å**	**1.65 Å**
O2 – V2	**1.62 Å**	**1.67 Å**
V1 – O3	**1.92 Å**	**1.87 Å**
V2 – O3	**1.92 Å**	**1.99 Å**
V2 – O4	**1.59 Å**	**1.62 Å**

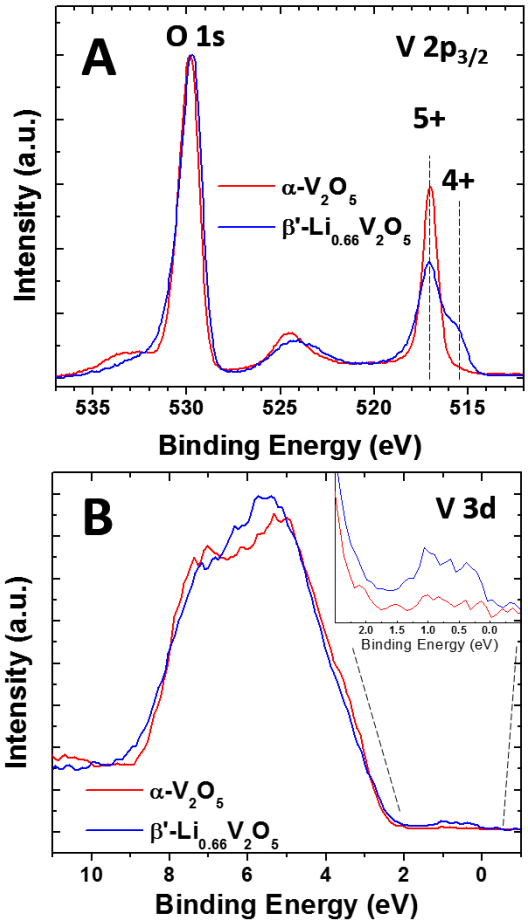

Figure A. 5: A) O1s and V $2p_{3/2}$ XPS spectra and B) valence band HAXPES data acquired for α-V_2O_5 and β'-$Li_{0.66}V_2O_5$. The inset to (B) highlights mid-gap states that appear upon Li-ion intercalation.

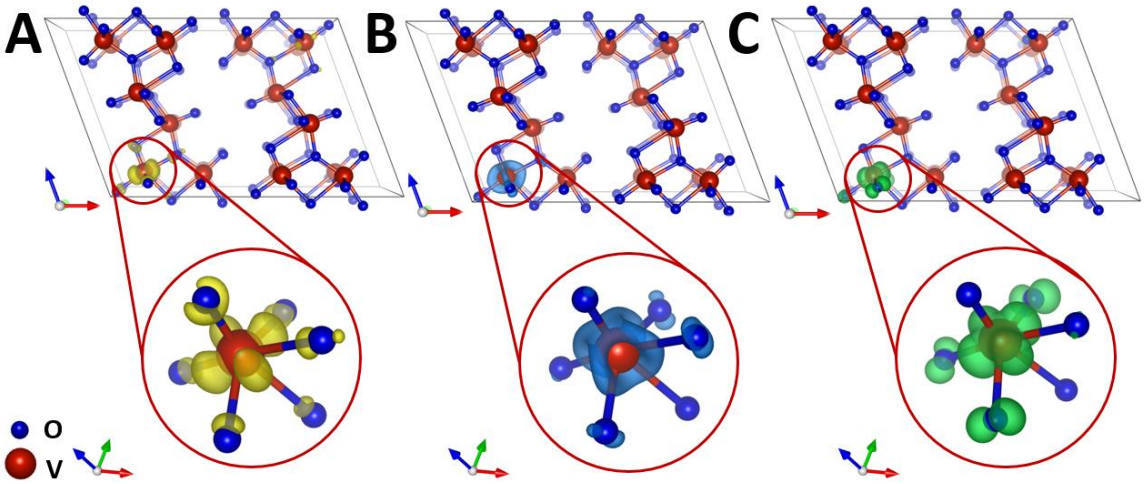

Figure A. 6: A) Charge density increase, B) decrease, and C) the orbitals associated with the mid-gap states for a ζ-V_2O_5 supercell reduced by a single electron (*sans* the Li-ion). The magnified view of the respective features are provided in the lower panel.

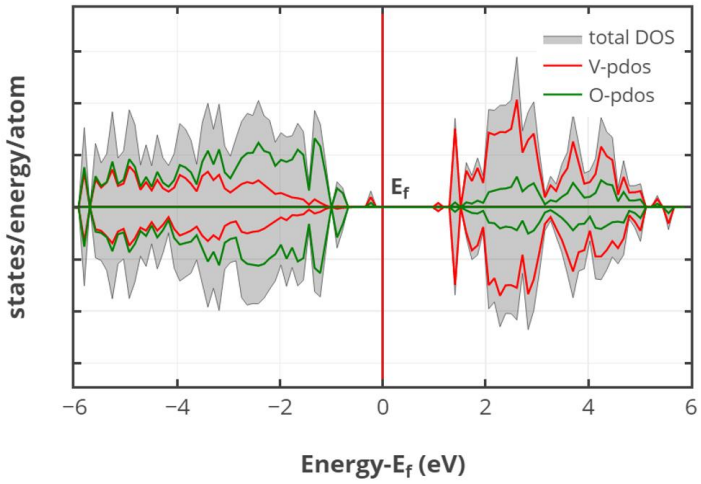

Figure A. 7: Total density of state (DOS) and atomic projected density of states (PDOS) for ζ-$V_2O_5^-$. The appearance of filled mid-gap state can be seen right near the Fermi level. The total DOS shows the non-degeneracy of ζ-$V_2O_5^-$ along one spin direction. The DFT+U calculations lowers the overall total energy by favoring the localization of electron along one spin direction.

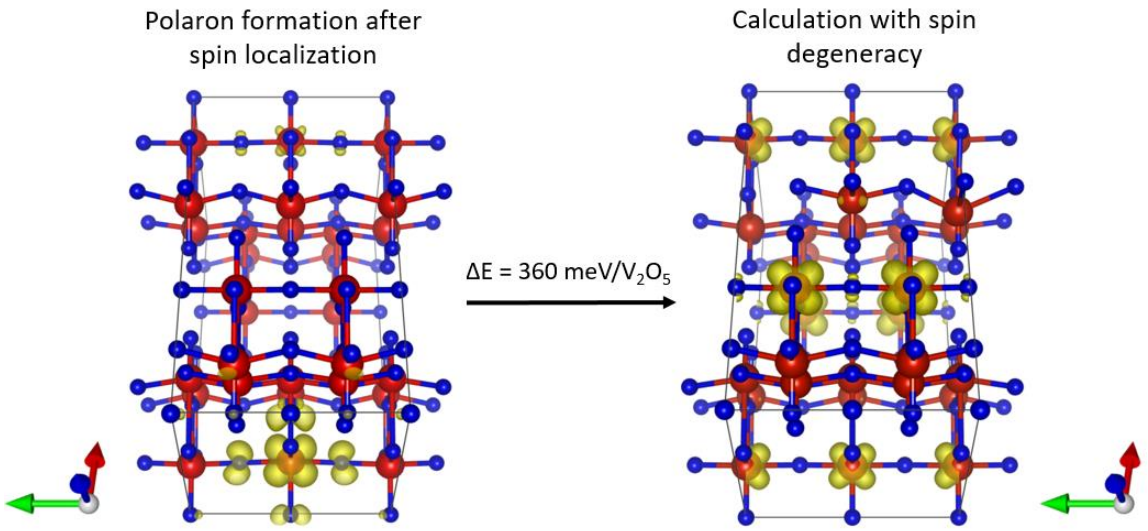

Figure A. 8: Enforcing spin degeneracy results in delocalization of electron density across the supercell. However, the configuration on the right is 360 meV per formula unit V_2O_5 higher in energy.

Supplemental Video A1: Video depicting distortion of the ζ-phase lattice that accompanies small polaron formation upon Li-ion insertion.

Supplemental Video A2: Video depicting coordination changes of Li-ion along diffusion bath between β and β′ sites in ζ-V_2O_5.